6-2020

Experimental Study of Collecting Running Water from Moderately Heated Water Vapors Using Turbulence-Induced Particles Collision (TIPC) Device

Hassan Ali Ghazwani
Western Michigan University, eng-alghazwani.hassan@hotmail.com

EXPERIMENTAL STUDY OF COLLECTING RUNNING WATER FROM MODERATELY HEATED WATER VAPORS USING TURBULENCE-INDUCED PARTICLES COLLISION (TIPC) DEVICE

Hassan Ali Ghazwani, Ph.D.

Western Michigan University, 2020

This dissertation describes the development of an alternative technique to collect water vapors or changing any vapor state to liquid state using a device called the turbulence-induced particles collision generator (TIPC). The experiment of collecting water vapors using the TIPC device is conducted at different values of temperature. The spatial patterns of droplets deposited on a wall due to the TIPC are measured at different values of pressure using luminescent oil technique, and the integrated intensity of deposited droplets is calculated. Also, the luminescent oil technique has been used to visualize the deposited particles on a pipe wall. ANSYS FLUENT Workbench 19.1 has been used to calculate the velocity field for the flow through the TIPC device.

EXPERIMENTAL STUDY OF COLLECTING RUNNING WATER FROM MODERATELY HEATED WATER VAPORS USING TURBULENCE-INDUCED PARTICLES COLLISION (TIPC) DEVICE

by

Hassan Ali Ghazwani

A dissertation submitted to the Graduate College
in partial fulfillment of the requirements
for the degree of Doctor of Philosophy
Mechanical and Aerospace Engineering
Western Michigan University
June 2020

Doctoral Committee:

Tianshu Liu, Ph.D., Chair
Parviz Merati, Ph.D.
Christopher Cho, Ph.D.
Dewei Qi, Ph.D.

ACKNOWLEDGMENTS

First and foremost, I would like to express how thankful I am to my advisor Dr. Tianshu Liu, for his inspiration, tolerance, excellent guidance, unweaving confidence and support throughout this project. He has provided countless helpful suggestions and has pushed me to be my best. I am grateful to my committee members especially Dr. Dewei Qi for his assistance, confidence, and support on this project. Also, I express my gratitude to Dr. Koorosh Naghshineh for permitting me to use the vibration lab instruments for my experiment.

I wish to thank the government of Saudi Arabia and JAZAN University who believed in me and provided me with a generous scholarship. I would like to thank my wife, Sahar and my children Abdulmaieed, Abdulaziz and Abdullatif, for their loving support and have provided me with strength and conviction to conclude this project. I am also very much obliged to my friends David Mosa, Hassan Fagehi who helped me by their suggestion and set up through my project. Thanks for my friend, Mofareh Ghazwani, for his unconditional support. Finally, I would like to thank my wonderful parents Ali and Kharifa for supporting me all throughout my educational studies. Their belief in my capacity to follow my dreams has guided me to achieve my goals education and it has made me who I am today. They are dearly missed.

Hassan Ali Ghazwani

TABLE OF CONTENTS

Table Of Contents–Continued

CHAPTER

LIST OF TABLES

LIST OF FIGURES

List of Figures–Continued

List of Figures–Continued

LIST OF ABBREVIATIONS

TICP	Turbulence Induced Particles Collision
C	Molar Concentration $(mole/Liter)$
R	Gas Constant $(L.atm/mol.K)$
P	Pressure (atm)
T	Temperature (K)
D_{AB}	Diffusion Coefficient (cm^2/s)
M_A, M_B	Molecular Weight
v_A, v_B	Atomic Diffusion Coefficient (cm^2/s)
L	Length (cm)
$N_A^{"}$	Evaporation Rate $(mol/cm^2.s)$
$n_A^{"}$	Mass Transfer Rate (mol/s)
M_w	Molecular weight of water (g/mol)
A_s	Cross section Area (cm^2)
h_m^-	The average of Local Convection Mass Transfer
h_m	The Convection Mass Transfer

Chapter 1

Introduction

1.1 Background

Water is considered the most important requirement for sustained life on Earth, and although about 71 percent of the Earth's surface is covered with water, only 2.5 percentage is fresh water while the remaining 97.5 percentage is salt water [1].

Due to an increasing population, fresh water is no longer enough to supply the entire world's population, therefore, additional methods to obtain fresh water are starting to become more and more popular. One of these methods is the desalinization of salt water from oceans, rivers and lakes. Nowadays, desalination plants are already in the operation in more than 120 countries, however, they are expensive and energy intensive. Desalination systems dependent on the adoption of reversible thermodynamic process due to the energy efficient which is independent of the mechanisms and the system used [1].

Sea water can be desalinated using three different methods: electrical, reverse osmosis and thermal. The electrical method uses electric current to separate the water and the salt. Typically, ions are driven across a selectively permeable membrane, which is carrying the dissociated salt ions with it. A key characteristic of this method is that the requirement of energy depends on the salt concentration in the water [2].

In another hand, the reverse osmosis technology is the most popular technique for water desalination. It uses the pressure to drive the water through a selectively permeable membrane where the salt is left behind. However, just like with the previous technology, the amount of energy required is based on the concentration of salt in the water [2]. Consequently, both are considered suitable for water with low salt concentration but they are too energy intensive for sea water.

It is important to mention, that the environment is affected by the emission of harmful and toxic gases that are coming from the traditional thermal desalination process. As a result, the globe temperature rises causing global warming. Even a small rise in temperature leads to melting of polar ice cap and elevation of the sea levels, which may dip small islands, coastal areas and riverbanks.

Another high efficiency alternative is the use of solar energy. The sun is the biggest source of clean renewable energy. Regions located between the tropic of cancer and the tropic of Capricorn regions obtain the highest solar energy isolation as shown in Figure 1.1.

The extraction of energy from the sun does not only represents a sustainable option, but it also provides a theoretical thermal efficiency of up to 100 percent since there is no limit in converting heat to heat.

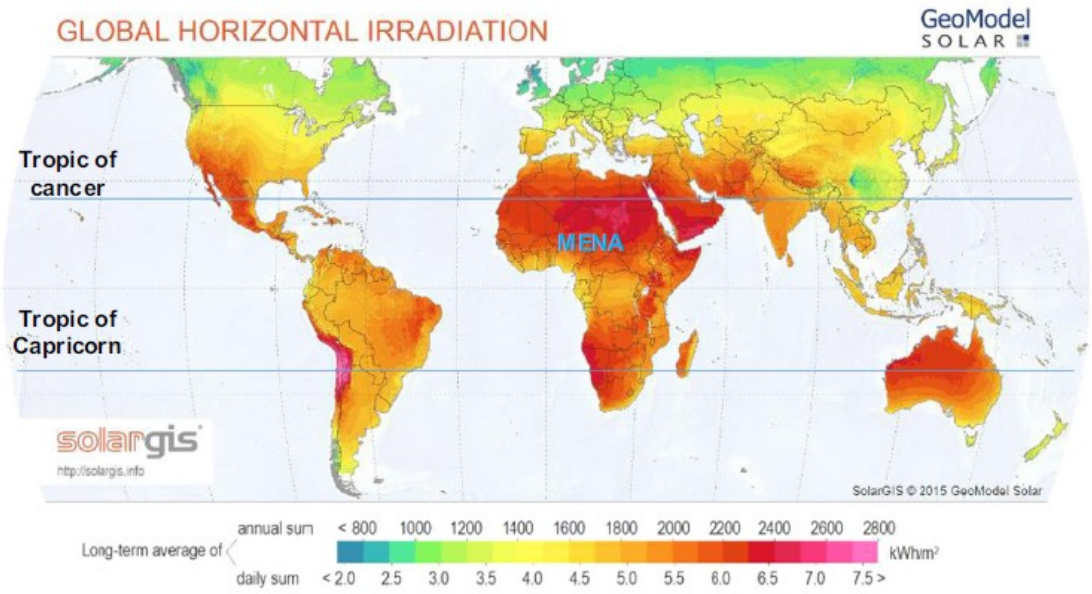

Figure 1.1: Global annual average of solar heat.

The shortfall of water is 2400 billion m3 and the global water demand would be 16,900 billion m3 by the year 2030 as shown in Figure 1.2.. Various desalination process are compensated the shortfall of water.

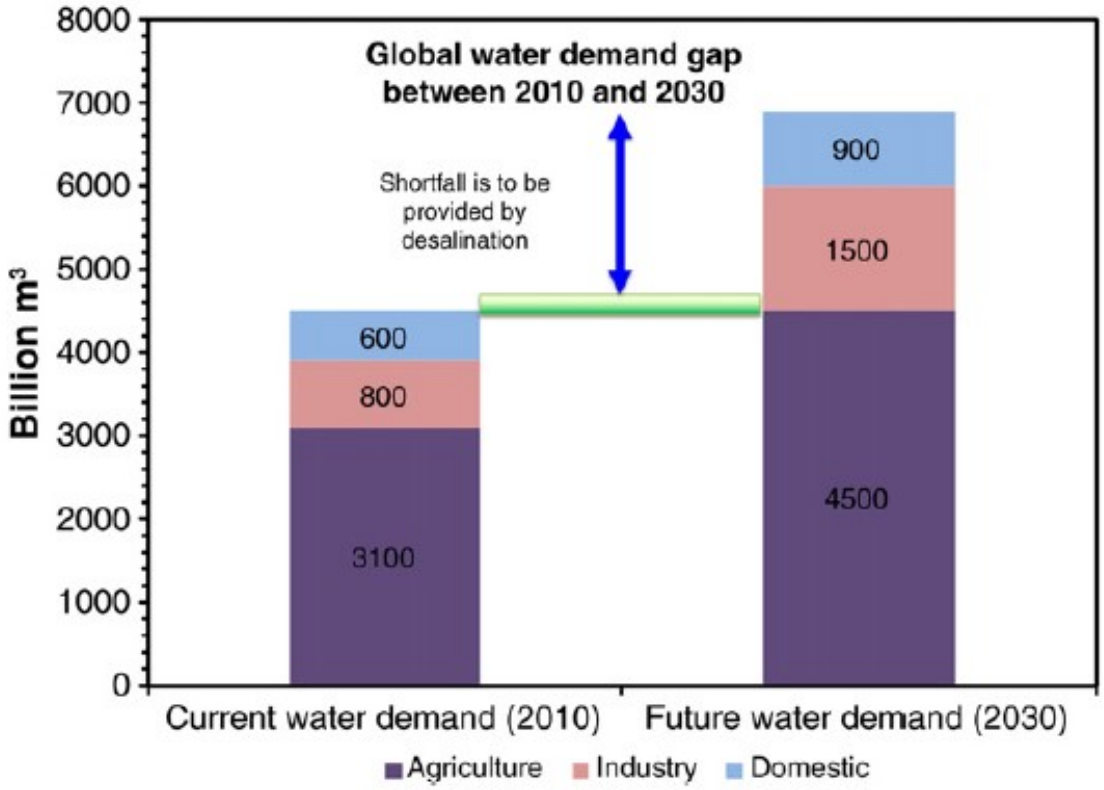

Figure 1.2: The demand for fresh water [3].

1.2 Motivation

The demand for freshwater is increasing annually, therefore, the desalination of seawater is playing crucial role to compensate for that. Current desalination systems required large amounts of energy, hence, the development of a more efficient and an affordable alternative is of the outmost importance. The sun sends a large amount of thermal energy to the seawater surface, which led to evaporate water. Thus, the present study was motivated to collect water vapors in order to produce fresh water using a device called turbulence induced particles collision generator (TIPC).

1.3 Objectives

The main objective of this study is to build and investigate the efficiency of the TIPC model. In addition, the improvement of the experimental model is investigated by studying three different TIPC models while describing their performance at various pressures and temperatures. Finally,

the last objective of this paper is to study the behavior of water particles deposition inside pipes using luminescent oil visualization technique.

Chapter 2

Literature Review

2.1 Desalination by Condensation

This chapter discusses different types of the desalination system by evaporation based on solar energy. The two types of solar thermal desalinations are direct and indirect systems as explained in Figure 2.1.

The indirect system relies on a series of subsystems (i.e., solar collector and the desalination unit) while the direct system is based entirely on the solar system. For the purpose of this work, we will focus on the direct process.

2.1.1 Direct System

As the name suggests, on a direct system, the evaporation and condensation are in the same device. Therefore, this type of system is more suited for domestic communities. Examples of this include single and double slope, water cone, water pyramid and triangle.

2.1.1.1 Sollar Still

The main characteristics of solar stills are: easy to build, inexpensive and uses the solar energy. It can be more economical comparing with other desalination technologies. Figure 2.2 presents some systems for solar stills. It is composed of a dark tank filled with brackish or salt water at certain level and used an inclined glass to cover it in order to facilitate transmission of solar radiation and condensation. The solar radiation entering the tank heats up the dark liner, which in turn heats up the water leading to evaporation. Due to the partial pressure difference and

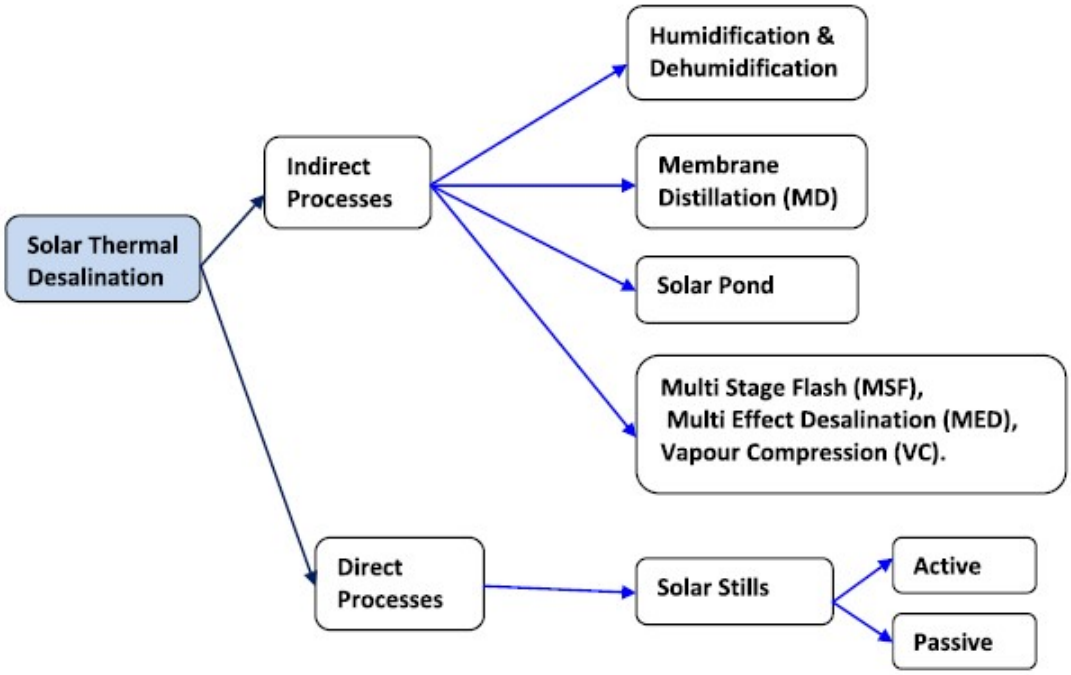

Figure 2.1: Possible configurations of solar energy resources with water desalination technologies [4].

temperature difference, the water vapor condensate over the inclined glass cover which is collected in a container at the bottom [5].

Many effect were study experimentally to investigate the performance of single solar still. The effect such as water color, reflector, addition of black dye, red dye, charcoal pieces and floating surface of different thickness with different density[6]. In addition, the effect of the depth of the water was tested. Based on the results, the dark-colored water heat up faster due to insensitive solar radiation absorption.

Abdallah et al. [7] studied the passive and active solar distillation and advice by experimental work. They advise to use the double passive solar stills to get fresh water for rural community. The water production increased to 22 percent by applying a computerized single axis sun tracking system for the solar still.

Nassar et al.[8] developed design to reflect and concentrate the sun rays on a solar still located at the focus by using concave mirrors as shown in Figure 2.3 and tested experimentally . The normal boiling of the income water was reduced by created vacuum of 562.5 torr in the solar

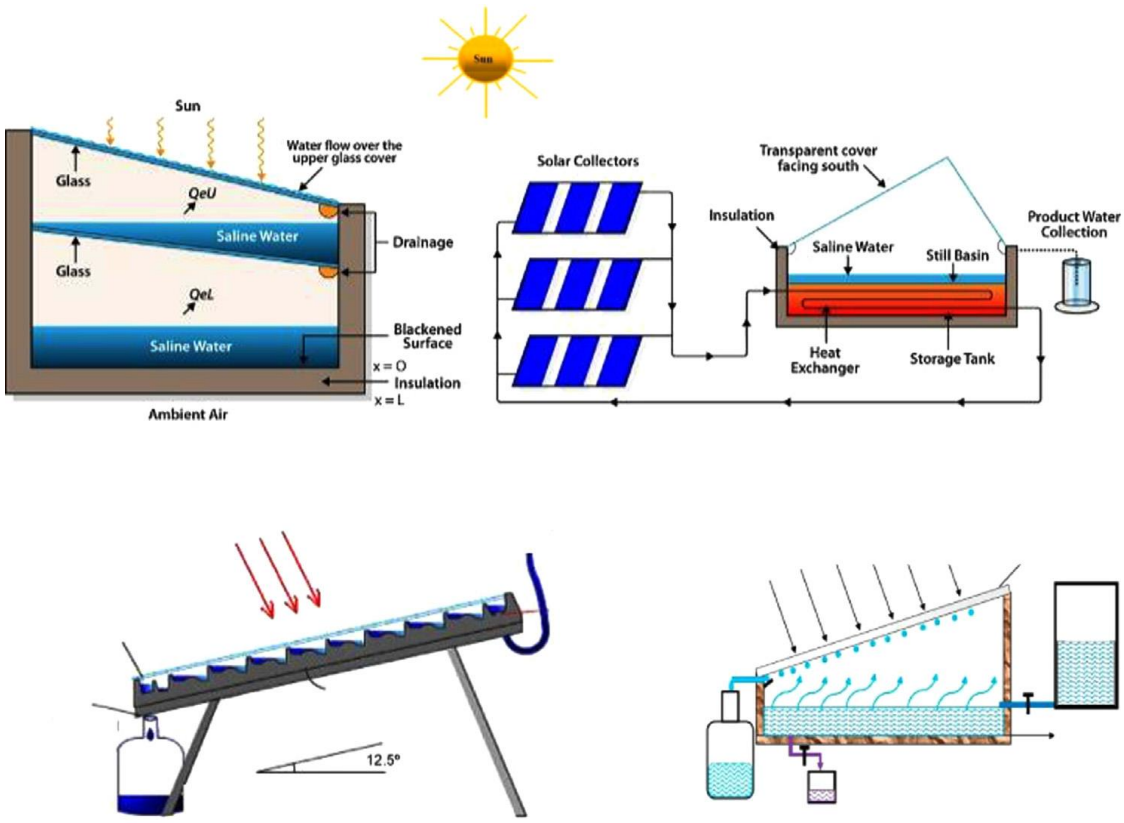

Figure 2.2: Some designs for solar stills [5].

still. The outlet vapor is condensed in the condenser and works as a water trap before entering the vacuum pump.

Al-Kharabsheh et al.[9] investigated a new design by using the natural forces to create the vacuum in the desalination system. The vacuum led to reduce the evaporation temperature of water with less energy. The schematic of the system is shown in Figure 2.4. The performance is low for simulated conventional still comparing with the experimental innovative still. The production work would increase by applying the latent heat of condensation in a multi effect system.

The working principle of the water pyramid is shown in Figure 2.5. This system is based on the temperature difference inside it in order to evaporate and condensate salt water. The sun provides the heat energy needed for evaporation. The design of the water pyramid was patented and rewarded for the small-scale innovation design from the World Bank. The water pyramid system has the ability to produce 1000 to 1250 liters of distilled water with area of 650 m2. This would be more beneficial for the daily need for many people. The large scale solar desalination

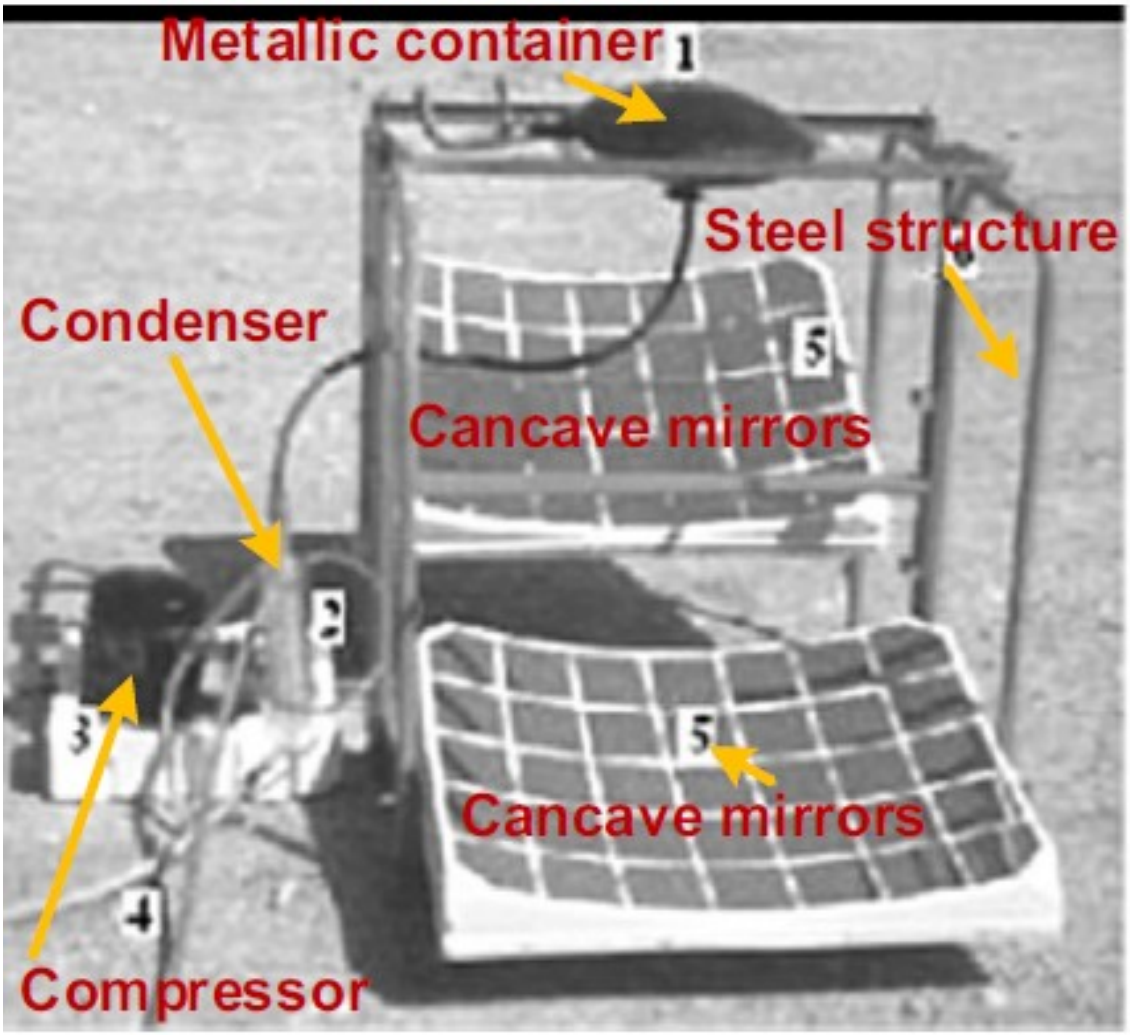

Figure 2.3: Point focus elliptical shape solar still[8].

water can be applied for the water pyramid system .

A. Ahsan et al.[10] have studied parameters affecting the performance of a low cost solar still. The design of triangular solar still is considered cheap and durable. The water productivity is proportional to the solar radiation and has an inverse relationship with the initial water depth. The water quality parameters are within the accepted ranges of drinking water. The design of triangular solar still is shown in Figure 2.6. This system can be easily build and improved by using the available materials such as polythene for the cover, PVC pipe for the frame, Perspex for the tough, nylon rope and transparent scotch tape.

Kumar et al.[11] investigated the thermal performance of V type solar still with combina-

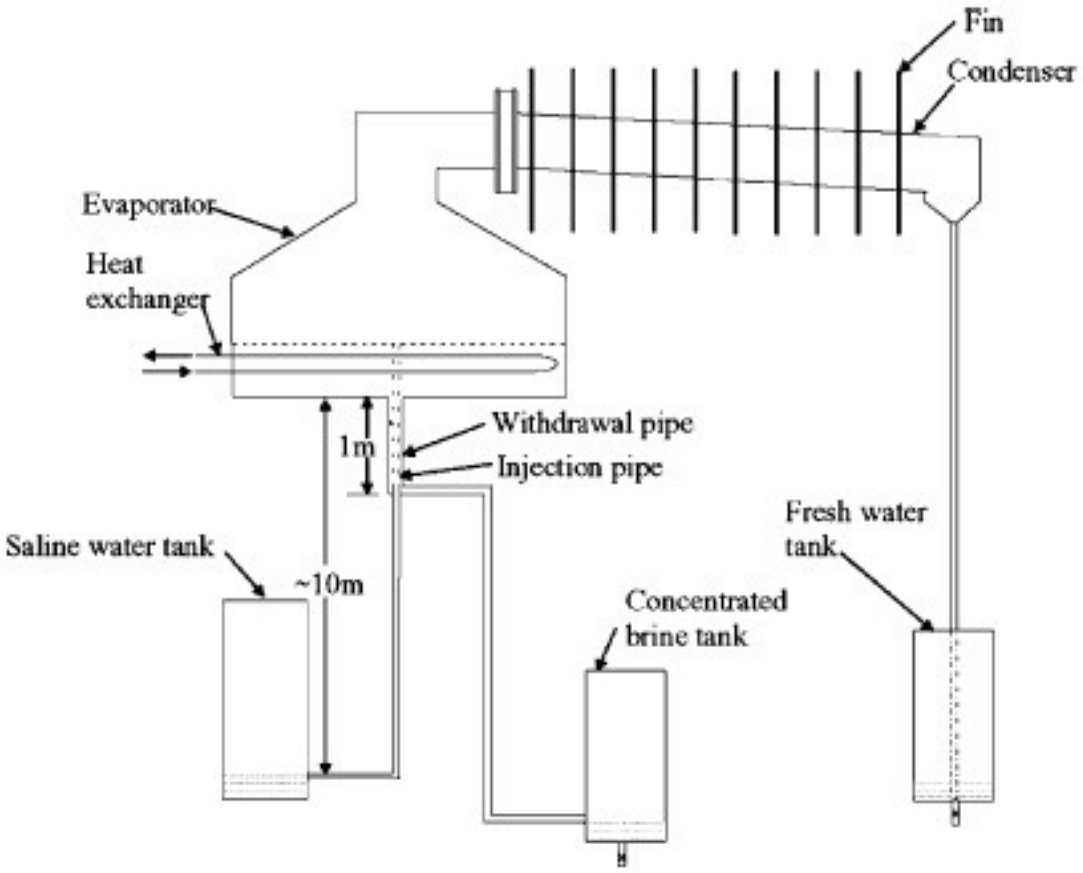

Figure 2.4: The schematic design for the system[9].

tion of a charcoal and distilled water collection. The internal and external heat transfer characteristics of the model were investigated. Based on experimental results, the efficiency of the system was: 24 % without charcoal, 30.05 % with charcoal, 11.92 % with boosting mirror and 14.11 % with boosting mirror and charcoal. The V type solar still has main advantage which is to easy control the direction of all condensation into the outlet collection.

Abu-Hijleh et al.[12] studied different types of sponge cubes with stills to yield a better production by capillary action. The production of stills was very high and the improvement reached up to 273 % resulting of using the sponge cubes in the basin water as presented in fig 10. The sponge cubes led to increase the surface area which the evaporation water occurs on.

Based on Janarthanan et al. [13] had theoretical and experimental study presented to determine the optimum uniform flow rate of water on glass water that is found to be 1.5 m/s. Using a

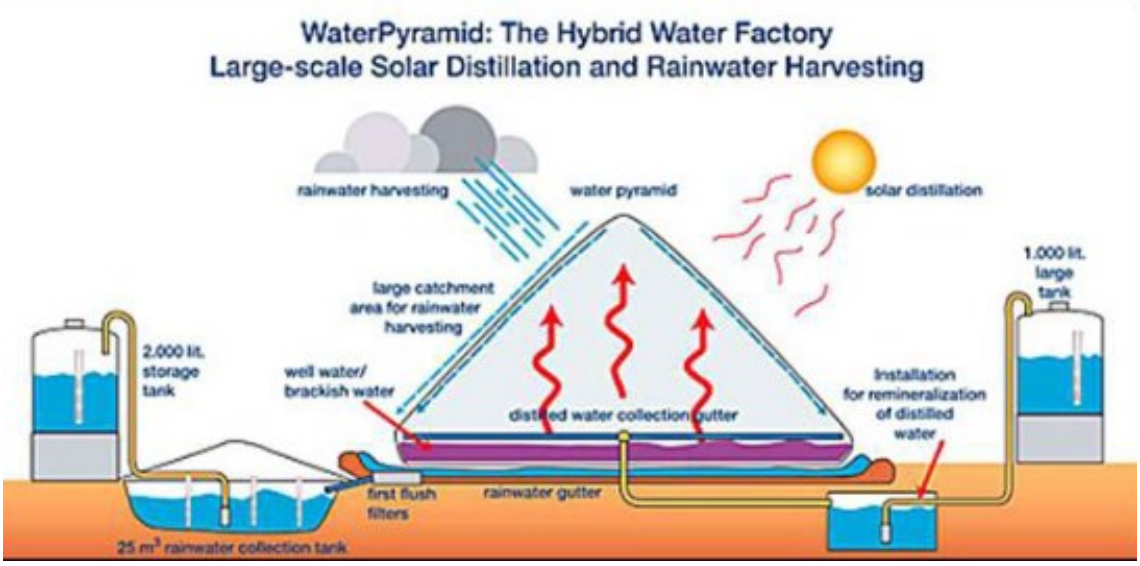

Figure 2.5: The design system for water pyramid.

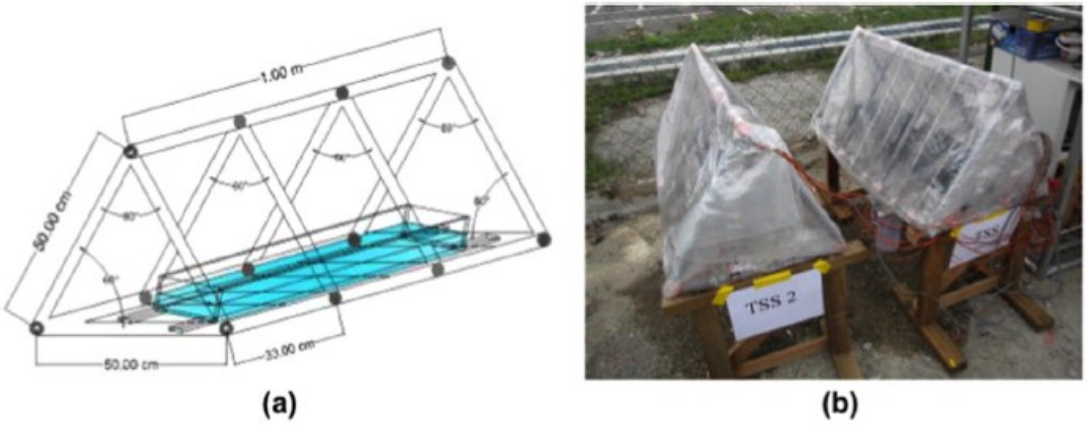

Figure 2.6: Triangular solar still, (a) Schematic diagram and (b) Picture of experimental set-up [10].

pressure regulator, this optimum flow rate can be achieved.

Bhardwaj et al.[14] presented an experimental the way to maximize the production of water by increasing the area of condensation surface for solar distillation. The system is easy to manufacture, inexpensive and operation for a household and community to meet the demand of drinking water. Figure 2.9 is presented the schematic design and the graphical results.

After experimentation, some techniques proposed an increment of the area of condensation in order to increase water vapor production. In addition, the cooling on the surface of the conden-

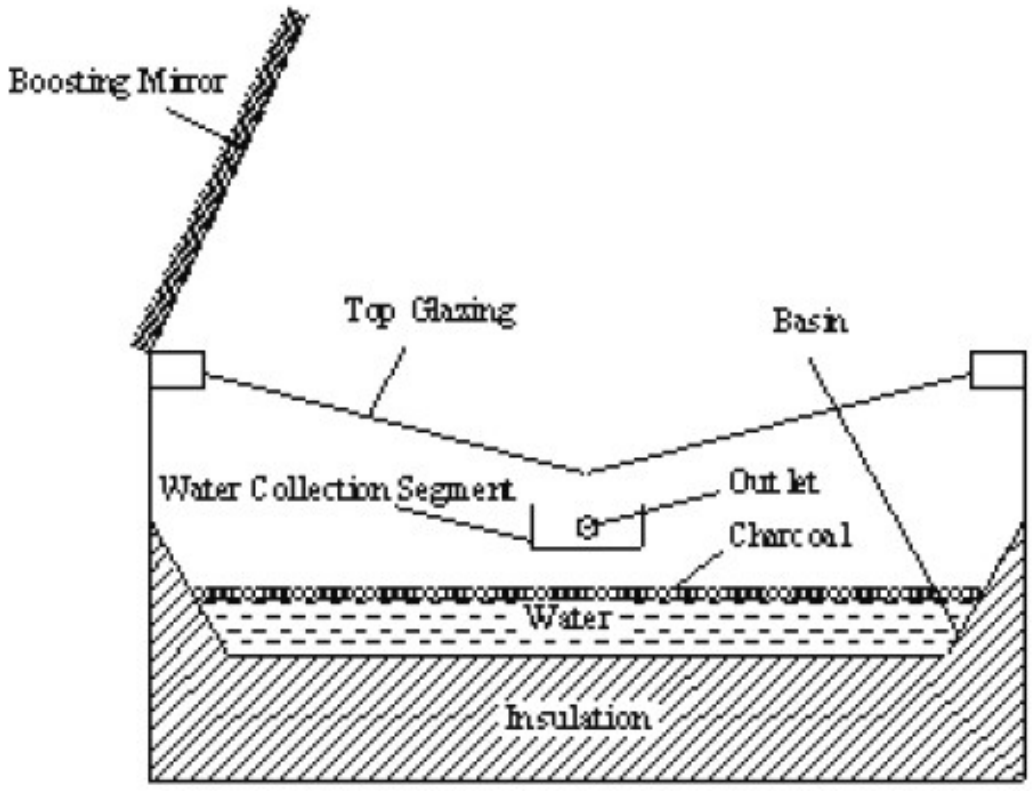

Figure 2.7: The schematic design of the V type solar still[11].

sation should be high. Another way to increase the rate of evaporation is by preheating the water and using internal fan cooling with an increased area of condensation increases the production of water.

This system consists of two units: one to evaporate the water, and another one to separate the condensed vapor in order to maximize the rate of condensation.

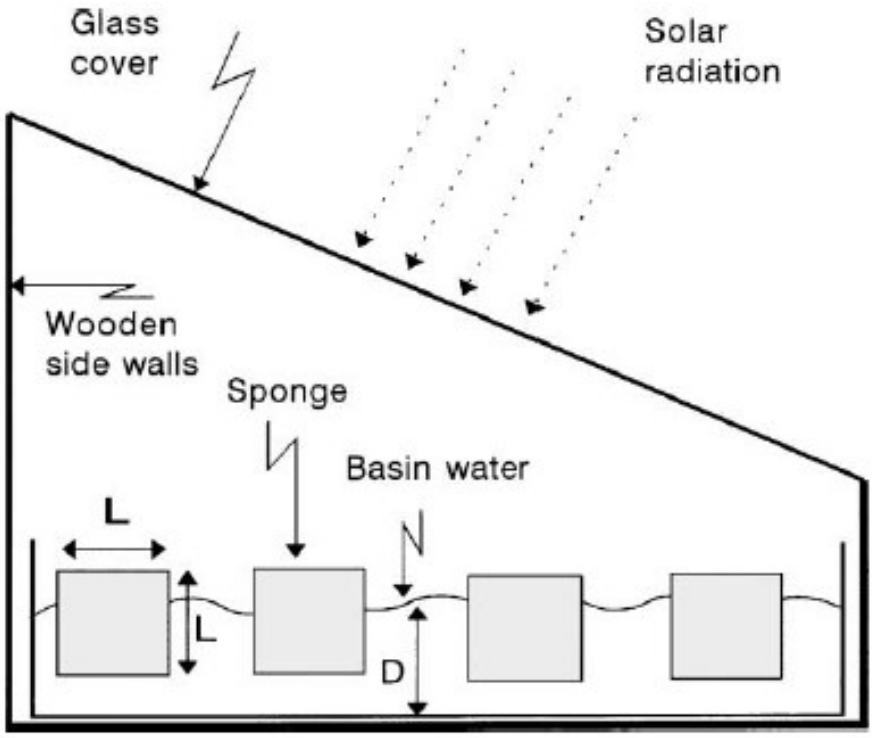

Figure 2.8: The design of the solar still include sponge cubes [12].

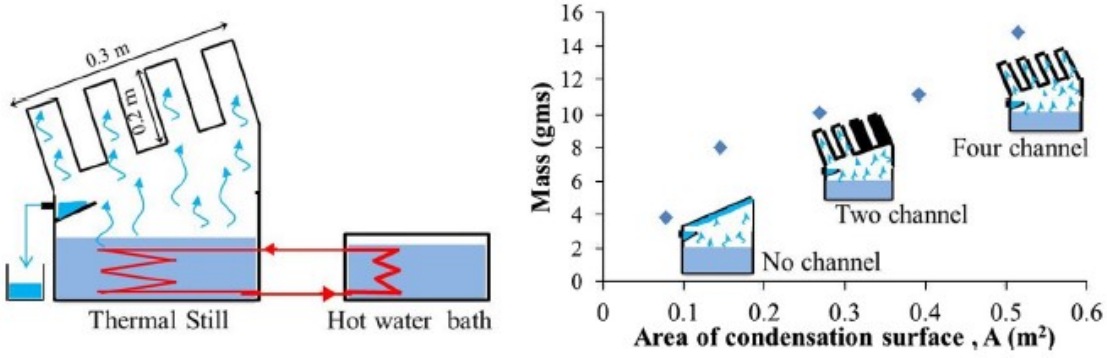

Figure 2.9: Schematic diagram, (a) Experimental setup and (b) Results with increasing condensation area[14].

2.2 Break Up and Collision of Droplets

Movement of droplets through a fluid has been investigated experimentally and numerically in terms of various aspects. Droplets have a strong impact due to their relevance in numerous

industrial applications such as inkjet printing, crop spraying and fuel injection. This section will cover most studies on droplets in different areas in terms of collision and break up.

Mundo et al. [15] have done experimental studies of liquid spray droplets impinging on a flat surface with an aim of formulating an empirical model describing the deposition and the splashing process. Droplet wall collision studies of deformation and breakup events were conducted where monodisperse droplets whose viscosity and surface tension was known were produced by a vibrating orifice generator. The droplets were directed towards a rotating disc and the impingement was visualized by employing an illumination that was synchronized with the droplet frequency. Previous depositions resulted in films that were eradicated using a rubber lip. Ethanol, water and a mixture of water-sucrose-ethanol are the liquids used in the study to establish the different viscosities and surface tensions.

After analysis of the results, one distinct result from the visualization is a correlation of the deposition splashing boundary in terms of Reynolds number and Ohnesorge number. Noteworthy is that a distinct correlation between the Re and Oh number, K = Oh. Re1.25, is only achieved if the normal velocity component of the impinging droplets is used in these dimensionless numbers. For the case of a splashing droplet, a two-component phase Doppler anemometer was utilized in obtaining characteristics of the size and velocity of the secondary droplets. The diameter distribution of the secondary droplets are hinged on the fluid properties such as viscosity and surface tension and kinematic parameters like velocity and size of the primary droplets in the case of an impingement on a smooth surface .

Wang et al.[16] illustrated the effect of air turbulence on collision efficiency. It was introduced and developed a general, kinematic formulation that can describe the collision kernel of hydrodynamically interacting droplets in turbulent air. Such a formulation has been developed and validated for geometrical collision rates of non-settling particles in turbulent flow without hydrodynamic interactions. Direct numerical simulations combining pseudospectral simulations of air turbulence and approximate analytical representation of local disturbance flows were used to validate the new kinematic formulation capable of describing the collision rate and collision efficiency of cloud droplets in turbulent air.

The theoretical formulation was similar to the formulation recently developed for geometrical collision rate of finite-inertia, non-settling particles. Its application to hydro-dynamically

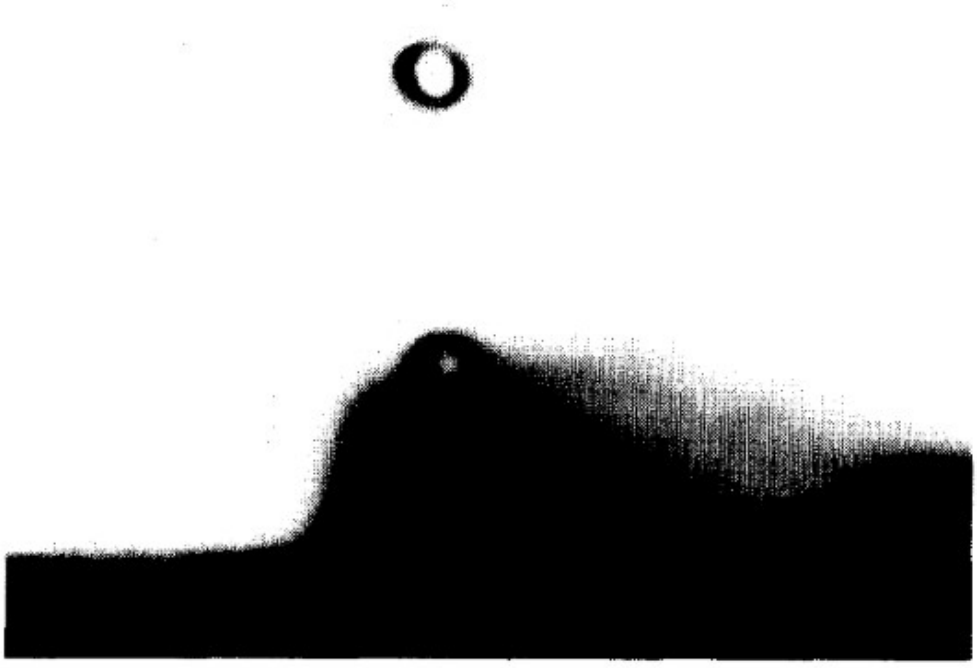

Figure 2.10: Splashing of a liquid droplet with Re = 598.8, Oh - 0.0518, K = 153.5 and St = 0.86 on a rough surface, effective angle of impingement x = 36 [15].

interacting droplets requires corrections because of a non-overlap requirement. An approximate method for correcting the kinematic properties was developed and validated against DNS data. The formulation presented here is more general and accurate than previously published formulations that, in most cases, are some extension to the description of hydrodynamic–gravitational collision.

Air turbulence improved the geometric collision rate and was found to enhance the collision efficiency because, in a turbulent flow, hydrodynamic interactions become less effective in reducing the average relative radial velocity. The level of increase in the collision efficiency depends on the flow dissipation rate. The experiment showed that hydrodynamic interactions lead to higher droplet concentration fluctuations. The formulation presented separates the effect of turbulence on collision efficiency from the previously observed effect of turbulence on the geometric collision rate.

Sikalo et al.[17] investigated experimentally the impact of droplets on horizontal surfaces. Results of the experiment are presented in Weber numbers from 50 to 1080, for water, glycerin,

and isopropanol. The movement of kinematics as well as the influence of wettability on walls was studied. Through results The Weber numbers showed that each diameter for the water, glycerin, and isopropanol varied. The water droplet diameter was about 2.7mm under the Reynolds number. In the wax surfaces, the water or glycerin droplets begin to recoil after the maximum diameter has been reached. There was, however, no recoil on the surface of the glass. The surface also did not affect the apex of the droplet, whether on the glass or wax surface. There was also the effect of velocity on the impact of the apex height of the liquid droplets. They were all showing the same or almost similar Weber numbers (92nm) and Reynolds 4200. The Figure 2.11 is presented the effect of surface on the apex height of a water droplet.

The maximum of the spread from a splash increases with every increasing Reynolds and Weber numbers, and hence it is important to choose the contact point as it determines the effect on the contact angle. Water droplets do not splash on smooth glass surfaces at values of below Weber 1080. It was also found that a rough surface reduces the Weber numbers and hence impact of water droplets. Liquids with higher viscosities such as glycerin produce a minimum spread and splash. The higher the viscosity, the lesser time it takes for a liquid to spread.

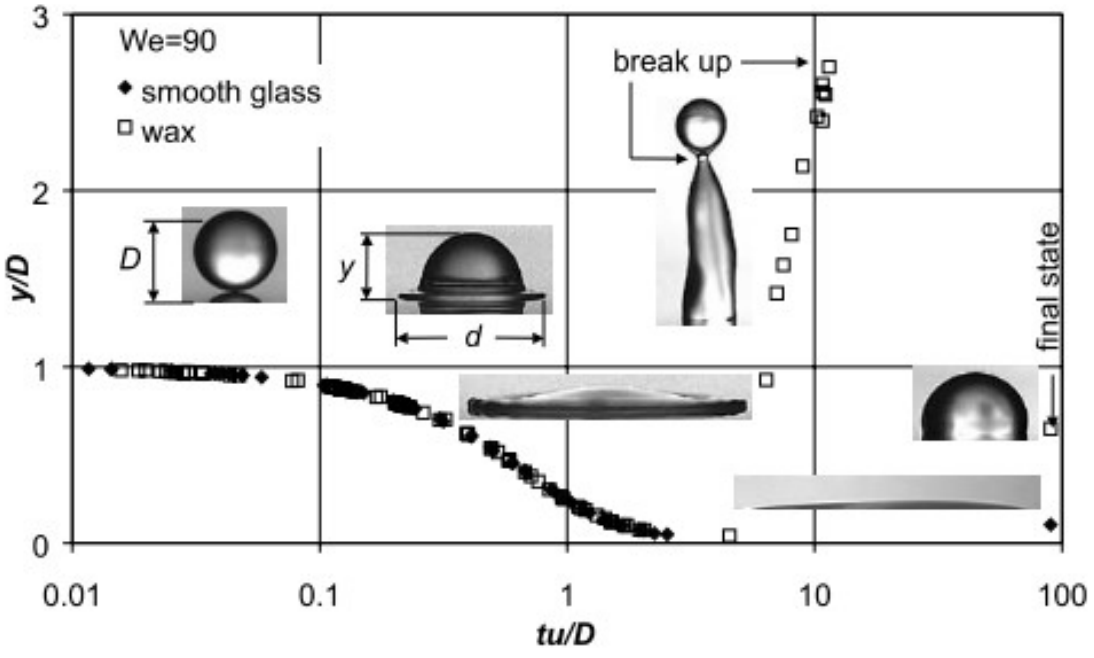

Figure 2.11: : Effect of surface on the apex height of a water droplet, D = 2.7 mm, u = 1.54 m/s, We = 90 [17].

Reade et al. [18] employed direct numerical simulation (DNS) and statistical analysis to investigate the dependence of the radial distribution function on the turbulence and particle parameters. Results were taken over a wide range of the relevant dimensionless parameters enabled estimation of collision rate. The effect of system Reynolds number over the limited range accessible by DNS is also presented. In general, the study showed that the degree of preferential concentration increases as the Reynolds number is increase.

Direct numerical simulations were performed in three parts. The first was the fluid phase where a pseudo-spectral algorithm was utilized to update the fluid velocity. The second part was particle motion the where a third-order Hermitian interpolation scheme used in this study. The last one was particle collision where particles of finite size approach to within their collision diameter, a hard-sphere collision becomes enacted. The simulations were organized in a way that majority were conducted on 643 fluid grid and each DNS began with fluid velocities that had reached statistically stationary states. Dependence on Reynolds number was considered and as Kolmogorov suggested, small scales dominated the particle enrichment.

In the study, a systematic analysis of the radial distribution faction (rdf) was performed to understand its dependence on other system parameters. According to previous studies, under dilute conditions, its dependence on the system loading can be neglected at no effect. The dependence of the rdf on the Reynolds number was separated from its dependence on the other parameters, allowing us to define a single factor G(Rel) that accounts for the Reynolds number. More dense particles (at a given Stokes number) are able to concentrate more strongly and thus achieve higher enhancement factors. Generally, the study confirmed that the degree of preferential concentration is proportional to the Reynolds number, hence increases with increasing Reynolds number.

Collins and Keswani[19] studied the impact of particle clustering on the inter-particle collisions. Since collision is a binary process that occurs at a rate proportional to the square of local number density, fluctuations in the particle concentration field caused by clustering increases the overall collision rate. Sundaram and Collins studied this effect and introduced the radial distribution function (RDF) in the collision kernel to account for particle clustering. The result was a monodisperse population of particle of diameter λ which is expressed in the formula below in the absence of Brownian diffusion or other molecular effects.Through the study, the correction to the collision kernel for particle clustering was completely captured by the factor $g(\sigma)$, which is nor-

malized to be unity for a uniform distribution of particles and increases with increasing clustering, reaching value s as large as 10–100 for $St \approx 1.0$. An impact such magnitude can greatly change an aerosol's distribution size under coalescence (liquids) and agglomeration (solids) as noted in the DNS study by Reade and Collins that showed that particle clustering increased cluster population growth rate and substantially widened particle distribution in comparison to other theories that ignored clustering.

Numerous numerical simulations have been conducted and given mixed results because of the small range of Reynolds number that can be examined. Hence in this paper, direct numerical simulation (DNS) was used over Reynolds number range 57-152 and to its effect, a forcing scheme maintained the average dissipation rate almost constant thus minimizing fluctuations in the Stokes number. Also, confidence analysis was employed to sample Reynolds number trends. Isotropic simulations were conducted in a periodic cube length of 2π on either side. Navier-Stokes and continuity equations below regulate incompressible fluids. A deterministic forcing was applied over the wavenumber range $1 < k < \sqrt{2}$ to minimize the amount of the fluctuations in the average dissipation rate and maintain it at preset values. The particles were then simulated by following to each particle's trajectory in reference to a Lagrangian frame.

Wang et al.[20] investigated two contributions separately via direct numerical simulations. The first one considered the geometric collision rates of finite-inertia particles only with an aim of determining the mean geometric collision rate of finite-inertia, monodisperse, heavy particles as a function of turbulence characteristics and particle inertial response time τp. The second was to separate out numerically the relative contributions of the turbulent transport effect and the accumulation effect.

Present studies have shown that large scale energetic eddies are the dominant factor contributing to the relative velocity between two colliding particles (the turbulent transport effect), whereas small-scale dissipative eddies can enhance the collision rate significantly by inducing local non-uniform particle distribution (the accumulation effect). The turbulent transport effect is most noticeable when the particle inertial response time τp is of the order of the flow integral timescale and the accumulation effect is most pronounced when τp is comparable to the flow Kolmogorov time.In the study, the effects of the two contributions are quantified with a numerical procedure that is independent of the computation of the average collision rate. This facilitated

the study of both the statistical description of the collision kernel and the relative contributions and modeling of the two physical effects. Simulations at several flow Reynolds numbers were performed to suggest a model for the accumulation effect. The data obtained revealed that the accumulation effect scales linearly with flow Taylor microscale Reynolds number $R\lambda$, while the theory for fully developed turbulence indicates that the maximum level of the turbulent transport effect scales with $R\lambda 1 = 2$.

Rioboo et al.[21] explored the influence of the drop size and the impact velocity on the process. Investigations on impacts of water drop impacts have been conducted on porous-like superhydrophobic polymer surfaces. In this study, superhydrophobicity in hydrophobic surfaces is defined by Wenzel's roughness index which is the ratio of real and projected planar surfaces. In the experiment, superhydrophonic surfaces were prepared using a polymer solution made by dissolving iPP at reflux in xylene. Drop impact was then conducted using Milli-Q water where drops of millimetric size were formed using syringes as well as needles of various diameters for precision. Due to pressure, the results yielded a Cassie-Baxter/Wenzel transition and wettability of the system are functions of the drop size and the outcomes of the impact or deposition process such as deposition, rebound sticking, and/or fragmentation. This further revealed that the smaller the drop, the higher the deposition. In addition, analysis demonstrates that the minimum velocity to observe a drop rebound follows a law in the inverse square root of the drop diameter given as $Vc = \sqrt{(2\sigma/(\rho d))}$. Moreover, wettability hysteresis of the surface controls the limit between deposition and rebound events. This limit corresponds to a rather constant Weber number Wec.

Rioboo et al.[22] probed crown formation during liquid drop impact on wetted surfaces. Impact drop features like crowns and splashes have been identified by use of high speed imaging systems. During the investigation, various liquids and numerous impact conditions were investigated to determine crown-splash (C-S) and deposition-crown (D-C) limits. The procedure included a high-speed CMOS camera and synchronised LED flashes (Weinberger) are used (typically 923 images per second to visualize impacting drops in full detailed motion. Generation of drops was done by using hypodermic needles of different diameters while the impact speed was controlled by changing the fall height of the drops. Solid substrates were silicon wafers with a roughness of molecular order, cleaned by being exposed to an argon plasma in order to get the highest possible wettability with respect to all of the liquids used.The results of the experiment yielded three

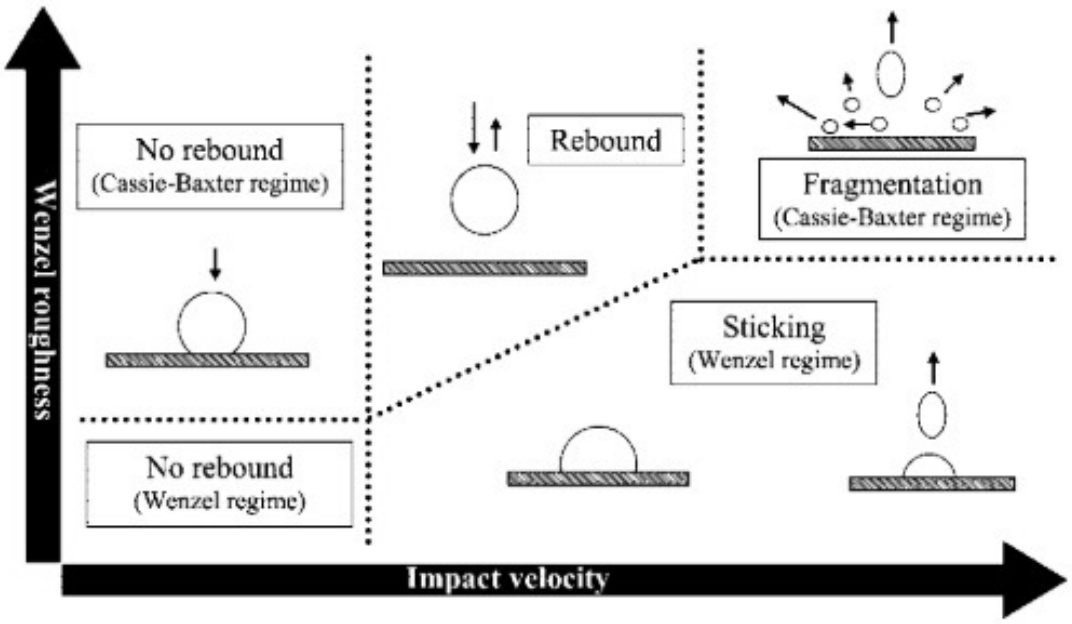

Figure 2.12: Scheme of the outcomes of a drop impacting a superhydro- phobic surface [21].

outcomes of impacts; deposition with neither formation of any crown nor break up, formation of crown without any break up, and splashes. Deposition outcome showed similar features to those of the impact on a dry surface with complete wetting. For high inertia impact, a decrease in the dimensionless thickness of the deposited film yielded a decrease of the duration of the crown leading to sooner ejection of droplets. Also, a decrease in the dimensionless film thickness (below 0.02), resulted to the formation of crown without splashing and the drop splashes without formation of a crown or depositing. The limit between the formation of crowns and deposition without formation of a crown increased in terms of Weber number. Similarly, the limit between the formation of crowns with and without splash decreased in terms of Weber number. These particular results were also found with the other liquids used in this study. It was determined that the splash-crown and crown deposition limits for liquid droplets impacting wetted solid substrates. For the thicker films $(0.06 < H* < 0.14)$, the limits were characterized by constant values of the K parameter while they converged in thinner films. In such cases, one passes from deposition to crown formation and then splashing by increasing the K value. But for $H* < 0.02$, crowns without splashing are almost no longer observed.

Fukai et al.[23] illustrated both an experimental and theoretical study of the deformation

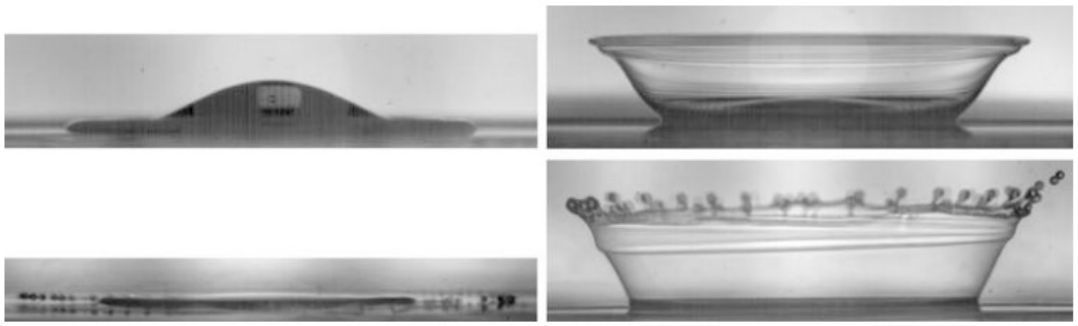

Figure 2.13: Outcomes of a drop impact on a wetted solid surface [22].

of a spherical liquid droplet colliding with a flat surface was conducted where experiments with impingement surfaces of different wettability were performed. It started with mathematical formulation where a mathematical model was based on the complete Navier-Stokes equations applied to the axisymmetric system. This system represents the centerline cross section of a droplet spreading after impact on a flat surface. Water droplets were formed by applying slight pressure, through syringe, to the inlet of a partially tilled water reservoir connected to a nozzle. The plunger of the syringe was advanced slowly, to allow for a droplet to form at the needle tip and detach under its own weight. After detachment, the droplet fell onto the surface of a glass plate. The vertical position of the needle was changed to vary the pre impact droplet velocity. A reflection-type photo sensor was set up below the nozzle tip. Droplet was detected by high-speed camera connected to a photo-sensor.

The results revealed that the initial rate of change of the splat height was in direct proportionate to the droplet impact velocity. Also, the maximum splat radius decreased with the value of the dynamic contact angle for the spreading stage. The effect of impact velocity on droplet spreading was more pronounced when the wetting was limited. On comparing experimental results to the numerical predictions in terms of droplet deformation, splat radius, and splat height, it can be concluded that the theoretical model accurately predicts the deformation of the impacting droplet in both the spreading phase and during recoiling and oscillation. Moreover, the wettability of the substrate upon which the droplet impinges significantly affected all phases of the spreading process.

Liquid droplets behave differently when ejected from nozzles and dropped or deposited on various solid surfaces. Rioboo et al.[24] conducted several experiments concerning deposition of a droplet on a solid surface together with the associated impulsive spreading and a subsequent ejection of a second droplet. An investigation to explain the formation of such droplets and their ejection in terms of a non-stationarity, wetting capillarity, inertia, viscous effects, and the shape of the drop for various liquids.

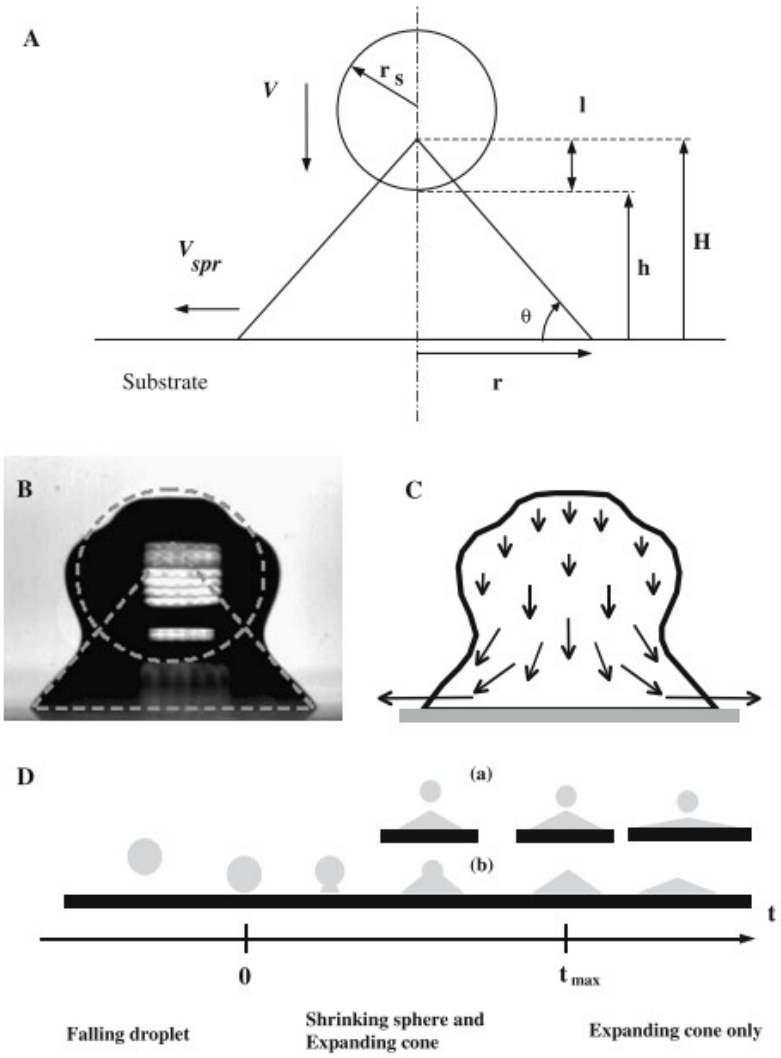

Figure 2.14: Drop during its first spreading stages (a) Schematic diagram presenting the two parts of the geometrical model (b) Example of drop shape (water droplet, diameter: 2.45 mm, impact speed: 0.093 m/s). Dashed lines: basic elements of the model (c) Possible scheme of the flow field. In the region of the contact line the velocity is high while in the reservoir region the velocity is uniform and low. (d) Time sequence for the falling droplet [24].

Liu et al[25]. investigated experimentally the deposition of micron liquid droplets on a glass wall in an impinging turbulent air jet. Visualization method (Luminescent oil) is used to measure the spatial patterns of droplets deposited on wall. The microscopic imagery is employed to acquire the statistical data of deposited droplets. Droplets deposition created two different rings on a wall where global diagnostics of velocity and skin friction are applied to explore the formation of the inner and outer rings.

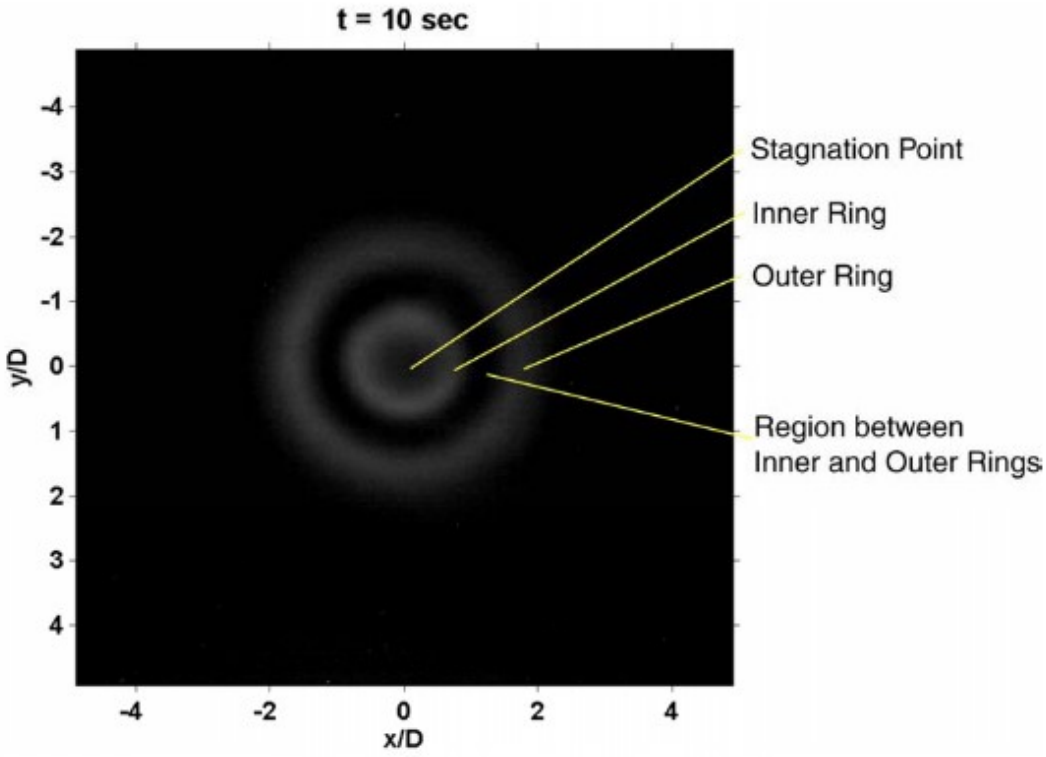

Figure 2.15: Characteristic regions in a luminescent image of deposited droplets at t = 10 s [25].

Chapter 3

Turbulence Induced Particles Collision (TIPC)

3.1 Theoretical Foundation

This section summarizes the theoretical foundation of turbulence induced particles collision (TIPC). This foundation is established by Liu [26] who presented a derivation of the power-law probability density function of a small separation between two inertial particles in homogenous isotropic turbulence by solving a random differential equation when the Stokes number is small. The effects of the Stokes number and Reynolds number on the power-law exponent are also described.

Clustering of inertial particles in turbulence which is known as preferential concentration of particles occurs in many natural phenomena and engineering processes. Direct numerical simulations (DNS) of statistics of inertial particles in isotropic turbulence have been conducted to understand the physical mechanisms of preferential concentration [27, 28, 20, 29, 16, 30, 31]. In the statistical mechanical modeling and simulation, the radial distribution function (rdf), which is proportional to the two-particle probability density function (pdf), is usually used to describe clustering in a system of particles in a volume [27, 29]. One of the most significant results found by DNS is that the rdf. for inertial particles exhibits an inverse power law of a separation [28, 30, 31]. The singular or near-singular behavior of the rdf near zero separation means that inertial particles tend to cluster in turbulence. Further, evidences for the power-law behavior of the rdf were also provided based on theoretical models [32, 33, 34, 35, 36, 37].

Liu [26] gave an alternative, more direct derivation of the power-law form of the p.d.f. of a small separation between two inertial particles in homogenous isotropic turbulence for small Stokes number under relatively weak conditions. A random differential equation for a separation

between two inertial particles was obtained from the kinematical equation. A generic random differential equation is

$$dr/dt = S(t)r + n(t) \tag{3.1}$$

where $S(t)$ and $n(t)$ are considered as a random particle strain rate and a random background noise, respectively. The random processes $S(t)$ and $n(t)$ are considered to statistically independent. Furthermore, it is assumed that $S(t)$ and $n(t)$ are the stationary random processes.

Eq. (3.1) is valid for homogeneous isotropic turbulence in which the random functions $S(t)$ and $n(t)$ can be considered to be independent from the spatial position of a particle and orientation of $\boldsymbol{r}$. Physically, since a fluid velocity field is differentiable in space, a conservative assumption is that the corresponding particle velocity field is differentiable when two inertial particles can closely follow the fluid motion of the smallest eddies in turbulence. It is required that the Stokes number is sufficiently small, i.e., $St = \tau_p/\tau_\eta << 1$, where τ_p is the particle response time and τ_η is the Kolmogorov timescale. A more relaxed requirement could be that a separation between two inertial particles is smaller than a small correlation length scale, and accordingly the particle response time τ_p is smaller than a small correlation timescale.

Using the Stratonvich perturbation method [38], Liu obtained a Fokker-Planck equation for the probability density function (pdf) of a separation from Eq. (3.2), and then gave a formal solution of the pdf. An asymptotic stationary pdf for a sufficiently small r is given by

$$p(r) = \frac{C}{(a_1 r^2 + a_2 r + a_3)^{1/2}} \exp\left(\int_{r_0}^{r} \frac{\langle S \rangle r + \langle n \rangle}{a_1 r^2 + a_2 r + a_3} dr \right) \tag{3.2}$$

The parameters a_1, a_2 and a_3 in Eq. (2) are the correlation coefficients and their physical meanings are discussed by Liu [26]. The means of the random processes $S(t)$ and $n(t)$ are denoted by $\langle S \rangle$ and $\langle n \rangle$. In fact, the exponential part in Eq. (3.2) is a solution of the Pearson system [39, 40, 41]. The Pearson system generates a family of distributions including the Gaussian, beta and gamma distributions, depending on the five parameters a_1, a_2, a_3, $\langle S \rangle$ and $\langle n \rangle$ in Eq. (3.2). However, in this specific application, most distributions derived from the Pearson system are not physically feasible. Under a condition $4a_1a_3 > a_2^2$, a physically feasible distribution of Eq. (3.2) is the Pearson type-IV distribution [39, 40, 41]. Carrying out the integration in Eq. (3.2) and then using a separation $\hat{r} = r/\eta$ normalized by the Kolmogorov length scale η , Liu obtained a

distribution

$$p(\hat{r}) = \frac{C}{(\hat{r}^2 + c_3\hat{r} + c_0)^{1-c_1/2}} \exp\left(\frac{2c_2 - c_3}{\sqrt{4c_0 - c_3^2}} a\tan\frac{2\hat{r} + c_3}{\sqrt{4c_0 - c_3^2}}\right) \tag{3.3}$$

where $c_0 = a_3/(a_1\eta^2)$, $c_1 = \langle S\rangle/a_1$, $c_2 = \langle n\rangle/(a_1\eta)$, $c_3 = a_2/(a_1\eta)$, and C is a constant. Here, a condition $4a_1a_3 > a_2^2$ is equivalent to $4c_0 > c_3^2$. Physically, it is plausible to assume that the correlation between $S(t)$ and $n(t)$ vanishes ($c_3 = 0$) and the mean noise $\langle n\rangle$ is zero ($c_2 = 0$). Thus, Eq. (3.3) gives a simple power-law form of the pdf

$$p(\hat{r}) = C\left(\hat{r}^2 + c_0\right)^{-(1-c_1)/2} \tag{3.4}$$

At this stage, the formal derivation of the power-law form of the pdf is purely based on the kinematical equation under considerably weak conditions. The dynamical information of particles is implicitly contained in the power-law exponent $c_1 = \langle S\rangle/a_1$ in Eq.(3.4).

To evaluate the power-law exponent $c_1 = \langle S\rangle/a_1$, the statistical properties of $S(t)$ such as $\langle S\rangle$ and $K[S(t), S(t+\tau)]$ should be determined based on the dynamics of a pair of particles. Liu [26] derived a generalized Langevin equation for $S(t)$

$$\tau_p\frac{dS}{dt} + S(t) = S_w(t) \tag{3.5}$$

where $S_w = S_f - w\tau_p$ acts as a formal random force and $w = 2S^2 + 2Snr^{-1} - |\Delta \boldsymbol{V}_{(2,1)}|^2 r^{-2}$ is formally treated as a known term. Based on an analysis of Eq. (5), Liu [26] gave a non-dimensional quotient of polynomials of the Stokes number $St = \tau_p/\tau_\eta$

$$c_1 = \frac{1 - (\hat{q}_1\hat{q}_2 St + \hat{q}_3 St^2)St}{\hat{k}_1 - \hat{k}_2 St + \hat{k}_3 St^2} \tag{3.6}$$

where $\hat{q}_1$, $\hat{q}_2$, $\hat{q}_3$, $\hat{k}_1$, $\hat{k}_2$ and $\hat{k}_3$ are non-dimensional parameters. for $St << 1$, the Taylor's expansion of Eq. (3.6) yields

$$\begin{aligned} 1 - c_1 = (\hat{k}_1\hat{q}_1 - \hat{k}_2)St + (\hat{k}_3 - \hat{k}_1\hat{q}_2 + \hat{k}_2\hat{q}_1)St^2 + \\ (\hat{k}_1\hat{q}_3 - \hat{k}_2\hat{q}_2 - \hat{k}_3\hat{q}_1)St^3 + (\hat{k}_2\hat{q}_3 + \hat{k}_3\hat{q}_2)St^4 - \hat{k}_3\hat{q}_3 St^5 \end{aligned} \tag{3.7}$$

It is found that the order estimates are $\hat{q}_1 \sim 1$, $\hat{q}_2 \sim 1$, $\hat{q}_3 \sim 1$, $\hat{k}_2 \sim 1$ and $\hat{k}_3 \sim 1$. Compared with the quadratic term in the right-hand side of Eq. (3.7), the last three terms (the higher-order terms) can be neglected for $St << 1$, since the coefficients in all these terms are $O(1)$. Therefore, the power-law exponent contains the linear and quadratic terms, i.e., $1 - c_1 = (\hat{k}_1\hat{q}_1 - \hat{k}_2)St + (\hat{k}_3 - \hat{k}_1\hat{q}_2 + \hat{k}_2\hat{q}_1)St^2$. The order estimates for the coefficients of the linear and quadratic terms are $\hat{k}_1\hat{q}_1 - \hat{k}_2 = o(1)$ and $\hat{k}_3 - \hat{k}_1\hat{q}_2 + \hat{k}_2\hat{q}_1 = O(1)$, respectively.Furthermore, it is found that these parameters in Eq. (3.6) do not contain the Reynolds number in the first-order estimates. Therefore, the power-law exponent $1 - c_1$ in Eq. (3.4) is, to a great extent, independent of the Reynolds number. The DNS results in a limited range of the Reynolds numbers have also showed the very weak dependence of the power-law exponent on the Reynolds number [29, 31, 19].

In summary, the asymptotic pdf of a small separation between two inertial particles in homogenous isotropic turbulence has a power-law form when the projected strain rate and the background noise are uncorrelated and the mean of the noise is zero. The power-law exponent determines the behavior of the pdf for a small separation. The power-law exponent is expressed as a quotient of polynomials of the Stokes number, which is further approximated by a quadratic polynomial of the Stokes number. The insensitivity of the power-law exponent to the Reynolds number is found. More importantly, the singular or near-singular behavior of the power-law pdf near zero separation of two small particles indicates that inertial particles will cluster in turbulence.

3.2 Experimental Evidence

The above theoretical results on turbulence-induced particle collisions and clustering are difficult to be directly validated in experiments since collisions of micron-size particles in turbulence cannot be directly observed. Therefore, turbulence-induced particle collisions were studied by Liu et al. [25] in experiments on deposition of micron liquid (olive oil) droplets on a glass wall in an impinging turbulent air jet. The spatial patterns of droplets deposited on a wall were measured by using luminescent oil visualization technique were two distinct rings of droplets deposited on a wall: inner and outer rings. In particular, the outer ring of deposited droplets was generated by the intriguing effects of turbulence in the wall-jet refion, including large-scale coherent vortices and small-scale random turbulence. The experimental evidences obtained in the

natural and wire-tripped impinging turbulent jets indicate that small-scale turbulence enhances the probability of collisions between small droplets to coalesce into large droplets. The collision rate of inertial particles is proportional to the turbulent intensity, which sheds light on the enhanced droplet collisions by turbulence for more effective deposition of droplets on a wall in an impinging turbulent jet.

To gain insight into the effect of turbulence on deposition of droplets, an impinging jet was tripped by a thin wire (a small circular cylinder) spanned across the jet exit through the center. Three wires with the diameters of 0.13, 0.35 and 0.65 mm were used for tripping the flow. For the jet exit velocity of 30 m/s, the corresponding Reynolds numbers based on the wire diameter were $Re_{d_w} = 263,\ 709$ and 1317, respectively, where d_w denotes the wire diameter. The nozzle-to-plate distance was 1.05.

Figures 3.1(a) and 3.1(b) are the luminescent oil images at t = 5 s in the impinging jet tripped by a 0.35 mm wire and a 0.65 mm wire, respectively. Clearly, the pattern of deposited droplets is drastically changed by a tripping wire, and particularly droplets are much more rapidly and heavily deposited behind a tripping wire due to wire-generated turbulence. There are two peaks in deposition of droplets on a wall around the location directly behind a tripping wire. A larger wire, such as a 0.65 mm wire, generates more effective deposition. The inner ring observed in the natural impinging jet does not appear clearly. The outer ring is still visible, but considerably thinner compared to the pattern of deposited droplets behind a wire.

The statistical data obtained from microscopic images provide more evidences on the favorable effect of wire-generated turbulence on deposition of droplets. Figure 3.2 shows the relative oil coverage distributions across the y-axis at t = 1 s for the natural jet and jets tripped by wires. The relative oil coverage is defined as a ratio between the oil-covered area in a microscopic image and the total area in the image. It is indicated that deposition of droplets is considerably enhanced by wire-generated turbulence near the center. The relative oil coverage reaches to about 40% at t = 1 s in the impinging jet tripped by a 0.65 mm wire, and then droplets will soon form a continuous film covering the region. The deposition of droplets increases with the wire diameter.

Global velocity diagnostics was conducted for the wire-tripped impinging jets. Figure3.3 shows the mean fields of the velocity, vorticity and turbulent kinetic energy in the wire-tripped impinging jet. The turbulent kinetic energy is high near the stagnation point. In contrast to large-

scale vortices entraining droplets toward a wall, small-scale turbulence is responsible to particle collisions and coalescences. To quantify the effect of wire-generated turbulence, the relative area-averaged turbulent intensity $\langle k \rangle_A^{1/2}/V_{ref}$ is estimated for the wire-tripped impinging jet, where $\langle k \rangle_A$ and A is a rectangle area in $-0.2 \leq r/D \leq 0.2$ and $0 \leq z/D \leq 0.5$. Figure 4 shows an integral of the distribution *N(d)* of particle numbers over a range of 4-9 μm as a function of the relative area-averaged turbulent intensity for the wire-tripped impinging jet. This clearly indicates the dependency of deposition of droplets with the diameters of 4-9 μm on the turbulent intensity.

In summary, the region of more deposited droplets is generated by the combined effects of large-scale vortices and small-scale turbulence on the motion of droplets in the wall jet. Strong small-scale turbulence induces collisions and coalescences of small droplets into large ones for more effective deposition. This mechanism is supported by the experimental results obtained in the wire-tripped impinging jet. Therefore, turbulence-induced droplet collisions could be utilized to effectively generate running liquid water from micro-size water droplets or water vapor. The above theoretical analysis and experimental results promote ideas of designing practical devices to obtain fresh water from moderately heated sea water by the solar energy. This is the main topic of the present work.

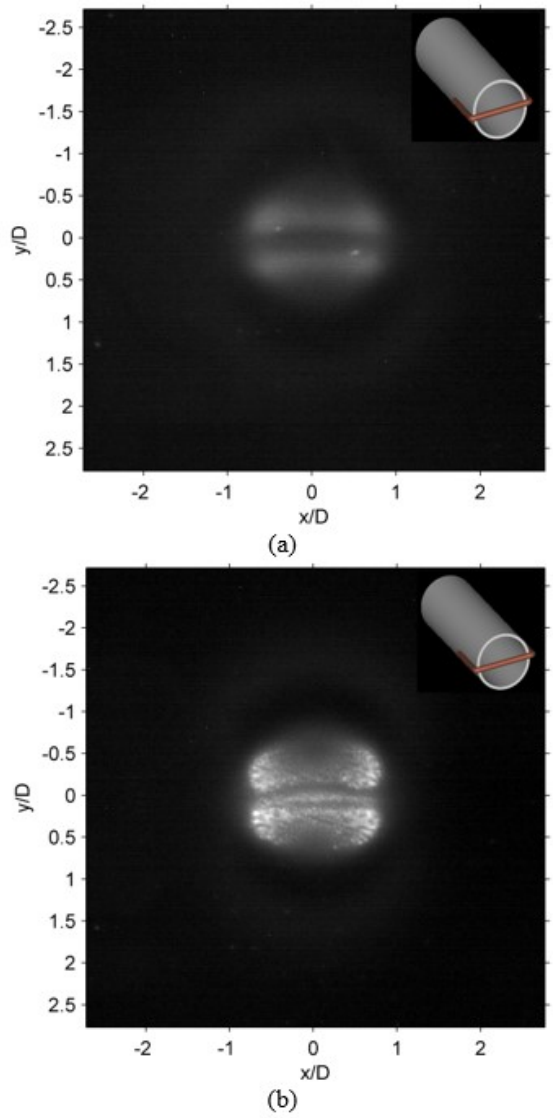

Figure 3.1: Luminescent intensity distributions at t = 5 s in the impinging jets tripped by (a) a 0.35 mm wire, and (b) a 0.65 mm wire [25].

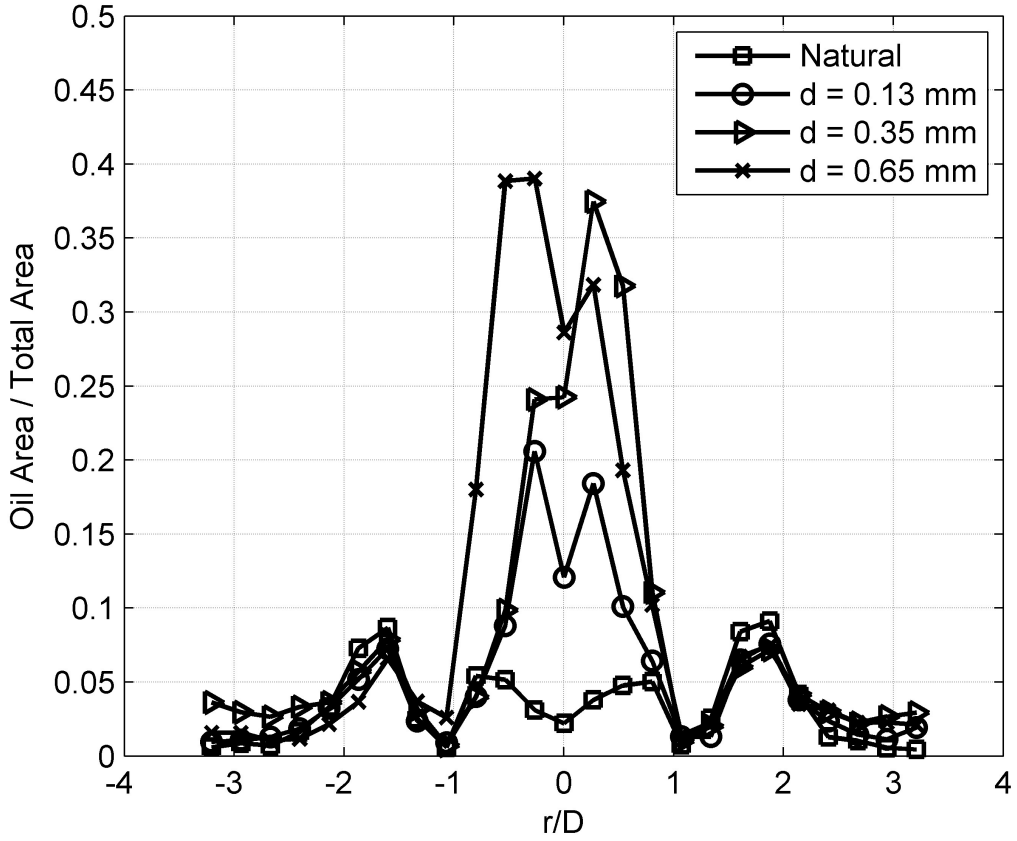

Figure 3.2: Relative oil coverage area distributions and across the y-axis at t = 1 s for the natural impinging jet and jets tripped by different wires[25].

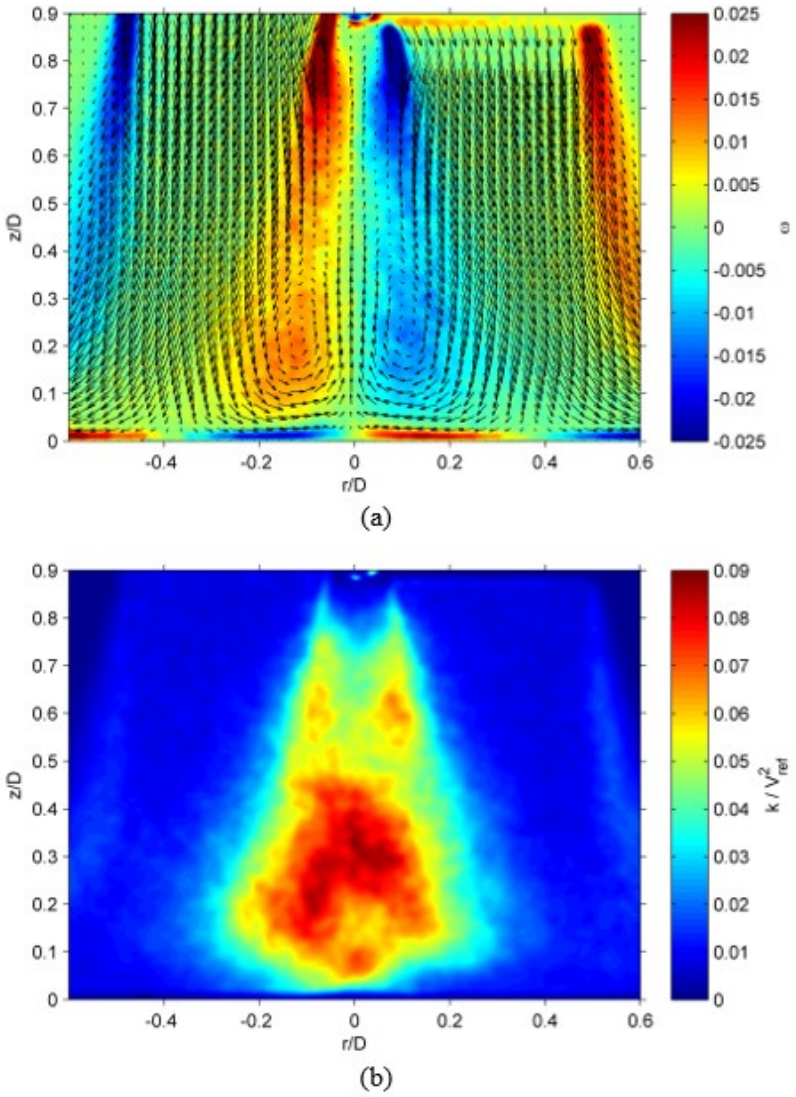

Figure 3.3: PIV measurements, (a) mean velocity and vorticity fields, and (b) turbulent kinetic energy field for the impinging jet tripped by a 0.65 mm wire[25].

3.3 Manufacturing and Design of TIPC Device

The manufacturing of most TIPC models is done by a 3D printer except one model manufactured from copper and aluminum. The material of the 3D printer is a Polylactic Acid (PLA). The shapes are designed using Autodesk Inventor Professional program. There are different configurations of the TIPC device. The first configuration is a cylinder shape placed vertically in the pipe and including three differents designs (A, B and C) based on its diameter. The model A has diameter of 10.16 mm and model B has 12.7 mm,their length are the same inner diameter of the pipe that they placed in which is equal to 15.875 mm. The model C has diameter of 9.5 mm and built from aluminum, it is placed in pipe from copper with a diameter of 13.97 mm. Figures 3.4 and 3.5 show different views of configuration 1 (A) and (B). The raw design of configuration 1(c) is shown in figure 3.6. The second configuration of the TIPC device is a diamond shape. It is designed by two lengths of 10.16 mm and 12.7 mm at the same widths of 5.08 mm. The diamond model is placed vertically in the acrylic pipe where the flow is perpendicular to its length. The glue is used to fix the piece of the model in the pipe and prevent leaking through the system. Figure3.7 shows different views of the diamond model of 10.16 mm length, while the diamond length of 12.7 mm is presented in figure3.8.

The next two configurations 3 and 4 of the TIPC device are designed based on increasing the surface area of the model.The third configuration has consisted of a cylinder of length 31.75 mm and a diameter of 12.7 mm with a hemispherical dome on its top. The cylinder is placed horizontally in the pipe where the flow direction is perpendicular to the hemispherical dome of the cylinder. Figure 3.9 shows different views of configuration 3 of the TIPC device. The fourth configuration of the TIPC device is an oval body of height 15.875 mm, length 25.4 mm and width 12.7 mm. It is placed in the pipe vertically based on its length. Figure 3.10 shows different design views of configuration 4 of the TIPC device.

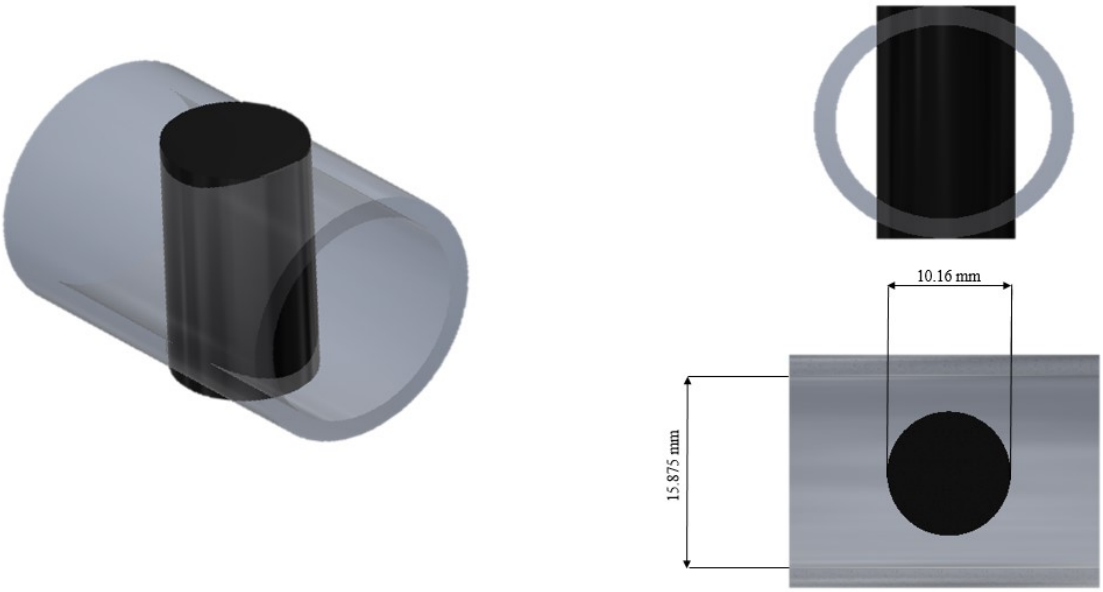

Figure 3.4: Configuration 1(A) of the TIPC device at 10.16 mm for cylinder diameter.

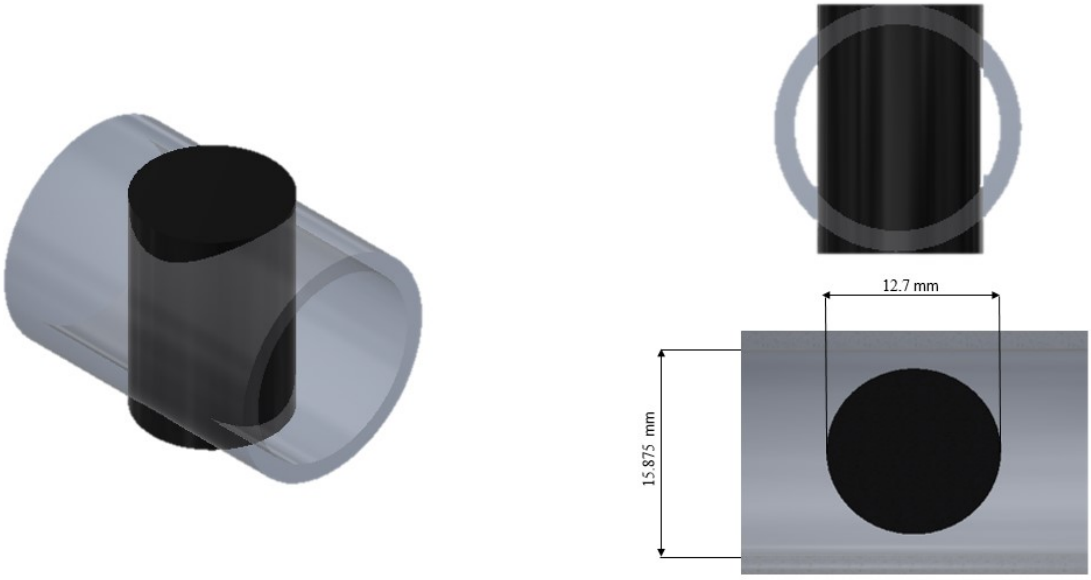

Figure 3.5: Configuration 1(B) of the TIPC device at 12.7 mm for cylinder diameter.

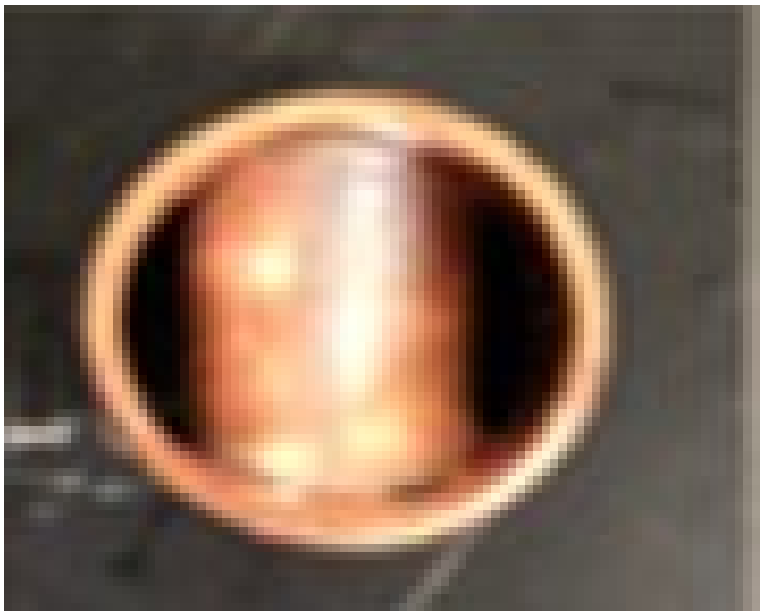

Figure 3.6: Configuration 1(C) of the TIPC device at 9.5 mm for cylinder diameter.

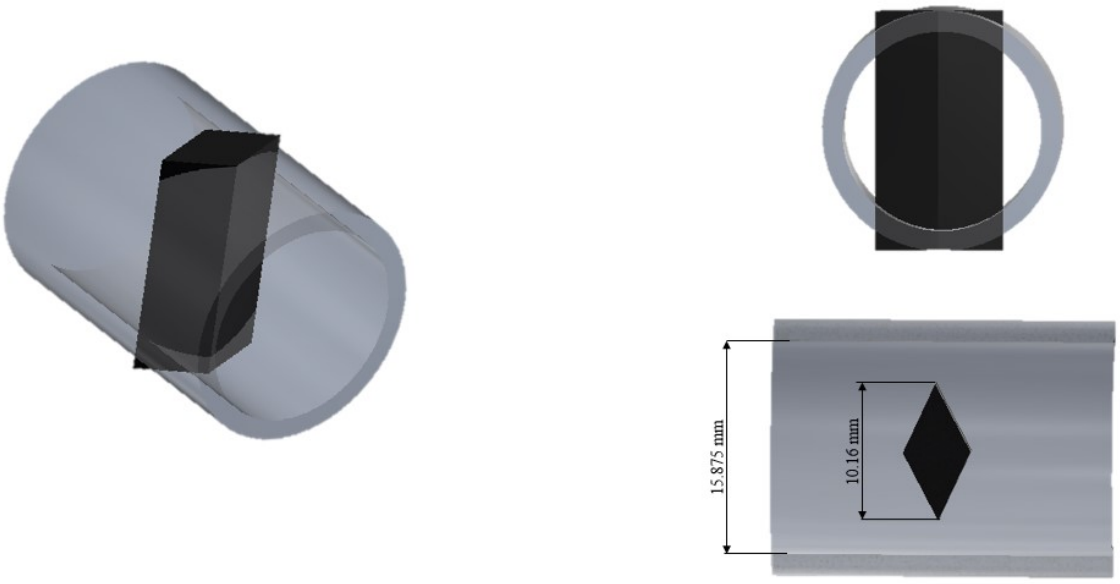

Figure 3.7: Configuration2(A) of the TIPC device at 10.16 mm for cylinder diameter.

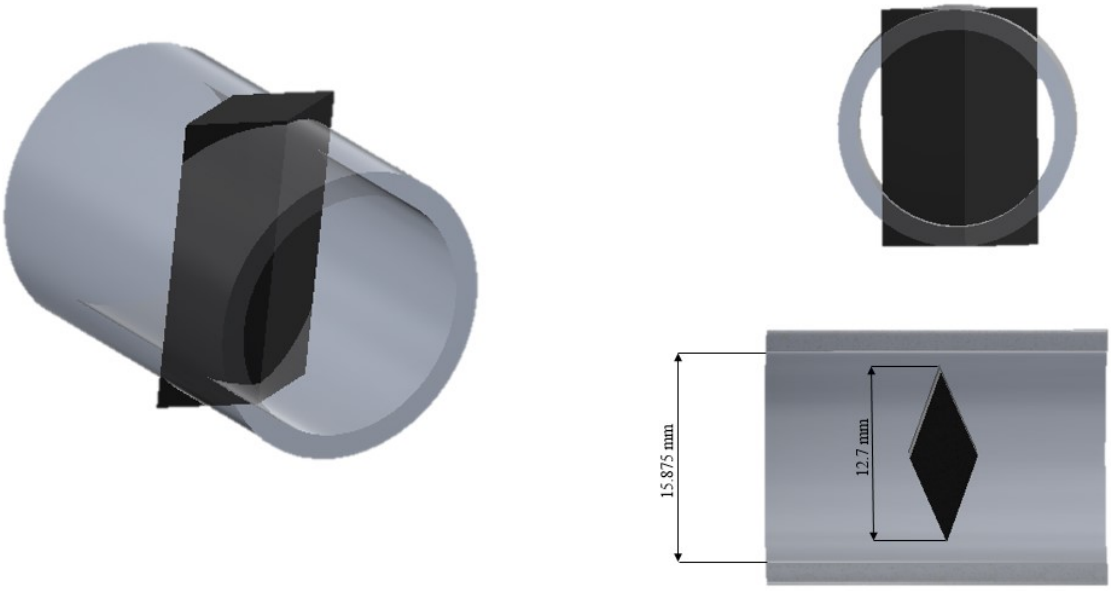

Figure 3.8: Configuration 2(B) of the TIPC device at 12.7 mm for cylinder diameter.

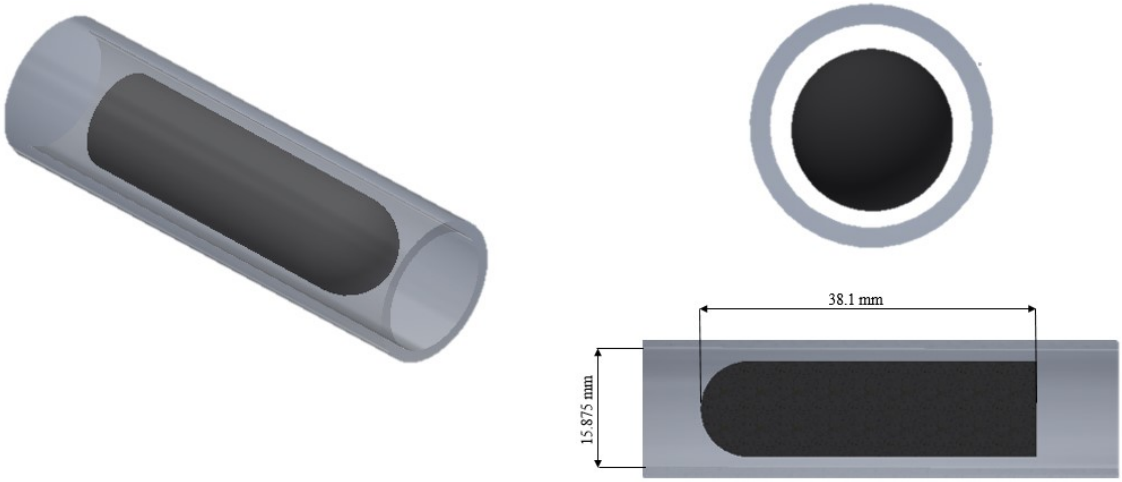

Figure 3.9: Configuration 3 of the TIPC device.

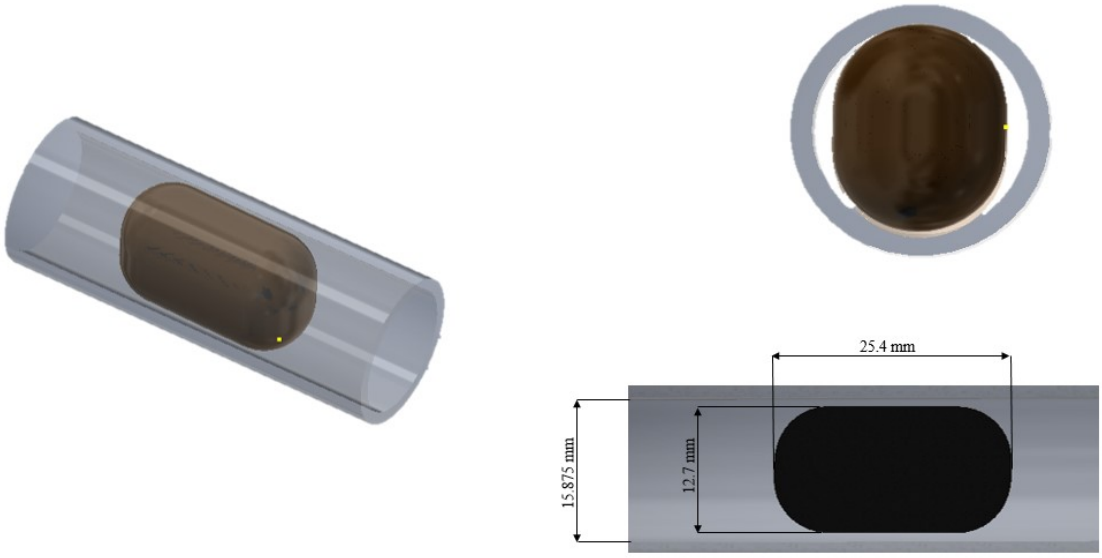

Figure 3.10: Configuration 4 of the TIPC device.

Chapter 4

System Modeling

4.1 Modeling of System

The proposed system is developed to improve the water vapor condensation on solar still systems, which is done using generated turbulence to increase droplets collision. The diagram of the proposed model is shown in Figure 4.1. This system is based on the diffusion of mass transfer for the water droplets of evaporation. The mixture, water vapor and gas, is consider diffusion in the binary gas mixture.

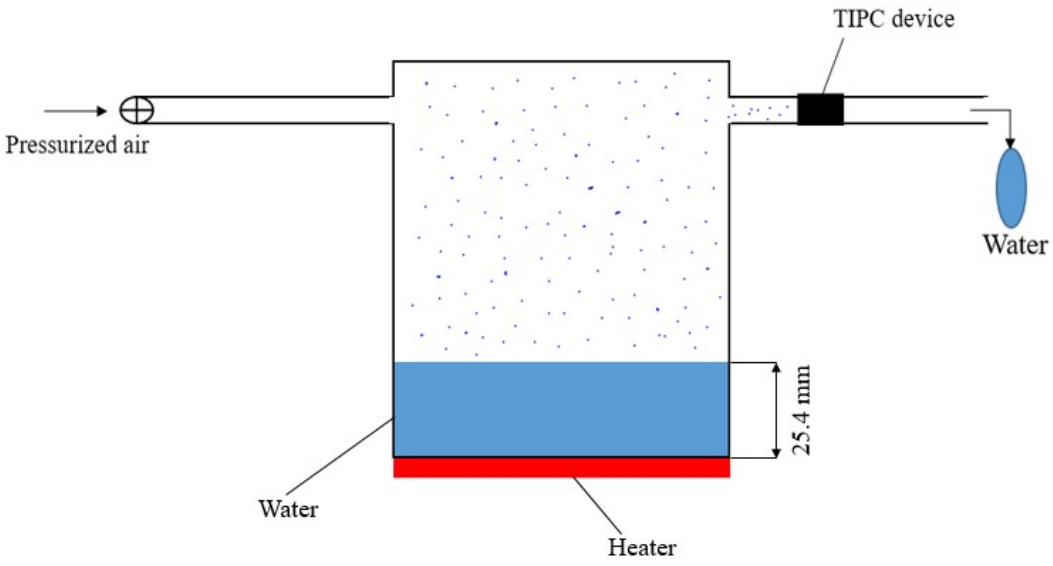

Figure 4.1: The design of system model.

4.1.1 Evaporation Rate in a Container

The system is running at constant pressure and temperature. Also, it has fixed species concentrations of water and air that are maintained at the top of the container. The concentration of vapor corresponds to saturated conditions in view of equilibrium exists between the vapor and liquid phases at the liquid interface. As a result of water concentration at the surface is higher than at the top, the water evaporates from the liquid interface and is transferred upward by diffusion. The evaporation process is shown in Figure 4.2. The molar concentration is determined based on the ideal gas which is explained in equation 1.

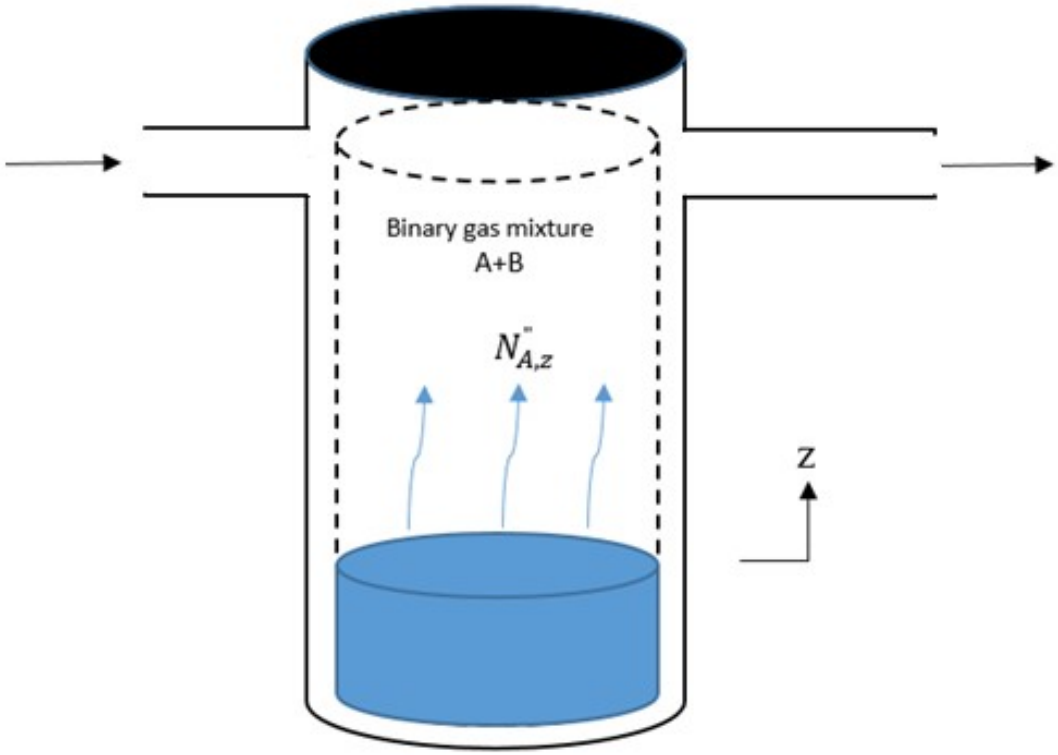

Figure 4.2: Evaporation of water into a binary gas mixture.

$$C = \frac{P}{RT} \tag{4.1}$$

The rate of transport water vapor from interface to binary gas mixture is based on pressure, temperature and binary diffusion coefficient. For constant pressure, temperature and also the bi-

Table 4.1: Atomic diffusion volumes reproduced from Fuller eat all [42]

Atomic diffusion volumes			
Atomic and structural diffusion volume increments			
C	15.90	F	14.70
H	2.13	Cl	21.00
O	6.11	Br	21.90
N	4.54	I	29.80
Atomic or heterocyclic ring	-18.30	S	22.90
Diffusion volumes of simple molecules			
He	2.67	CO	18.00
Ne	5.98	CO2	26.70
Ar	16.20	N2O	35.90
Kr	24.50	NH3	20.70
Xe	32.70	H2O	13.10
D2	6.84	Cl2	38.40
N2	18.5	Br2	69.00
O2	16.30	SO2	41.80
Air	19.70		

nary diffusion coefficient is also constant. The procedure to calculate the diffusion coefficient of evaporated water was developed by Fuller et al.[42]. Parameters are known as 'atomic diffusion volumes' were used. A list of the atomic diffusion volumes is given in Table 4.1. The following equation is used to calculate the diffusion coefficient:

$$D_{AB} = \frac{0.0052T^{1.75}(\frac{1}{M_A} + \frac{1}{M_B})^{0.5}}{P[\upsilon_A^{\frac{1}{3}} + \upsilon_B^{\frac{1}{3}}]^2} \tag{4.2}$$

The mole friction distributions based on interface and at the top are explain in the following equation:

$$\frac{1 - Z_A}{1 - Z_{A,0}} = (\frac{1 - Z_{A,L}}{1 - Z_{A,0}})^{\frac{Z}{L}} \tag{4.3}$$

since $1 - Z_A = Z_B$, we also obtain

$$\frac{Z_B}{Z_{B,0}} = (\frac{Z_{B,L}}{Z_{B,0}})^{\frac{Z}{L}} \tag{4.4}$$

To calculate the evaporation rate of water, the mole friction gradient has to be evaluated. After substituting the result, the evaporation rate equation in mole per centimeter square second is as

following:

$$N_A^{"} = \frac{CD_{AB}}{L} ln(\frac{1-Z_{A,L}}{1-Z_{A,0}}) \tag{4.5}$$

So, to determine the mass transfer rate as moles per second is by multiply cross section area to equation 3.5 to be as following:

$$n_A^{"} = N_A^{"} \times A \tag{4.6}$$

In order to determine the capacity of the evaporation water rate in gram, the molecular weight of water is multiply to equation 3.6 to be as following:

$$m^{\cdot} = n_A^{"} \times M_w \tag{4.7}$$

4.1.2 Convection Mass Transfer

The convection mass transfer takes place when the uniform air flow moves throughout the system carrying water vapor. The total molar transfer rate of water vapor for an entire surface based on the mass transfer convection coefficient is expressed as following:

$$N_{A,s}^{"} = h_m(C_{A,s} - C_{B,\infty}) \tag{4.8}$$

Where the average and local mass transfer convection coefficients are related by an equation of the form:

$$\bar{h_m} = \frac{1}{A_s} \int_{A_s} h_m dA_s \tag{4.9}$$

4.1.3 Evaporation Rate Measurements

Two experimental have been done to measure the evaporation rate for open and closed system. The water level is fixed at a level of 25.4 mm of container depth. The total mass water inside the system is 1418.23 g. Both systems are tested at the same conditions of temperature values

55, 65 and 75°C. However, the weight of evaporation rate is calculated analytically based on the correlation of diffusion coefficient and then applying the equations 5.3-5.6 in order to be in system dimensions. Figure4.3 shows the evaporation water as function of time at 55°C for two systems and analytical solution, indicating the evaporation increasing with time. The analytical solution and open system have some agreement in increasing the amount evaporation water with time. the effect of rising the temperature to be 65°C on the evaporation water are shown in figure4.4.The water evaporation is tend to be stable with time for the closed system comparing with the open system and analytical that are continue increasing with time. Also, the results of water evaporation at 75°C have the similar behaviors for both systems and analytical solution as presented in figure4.5.

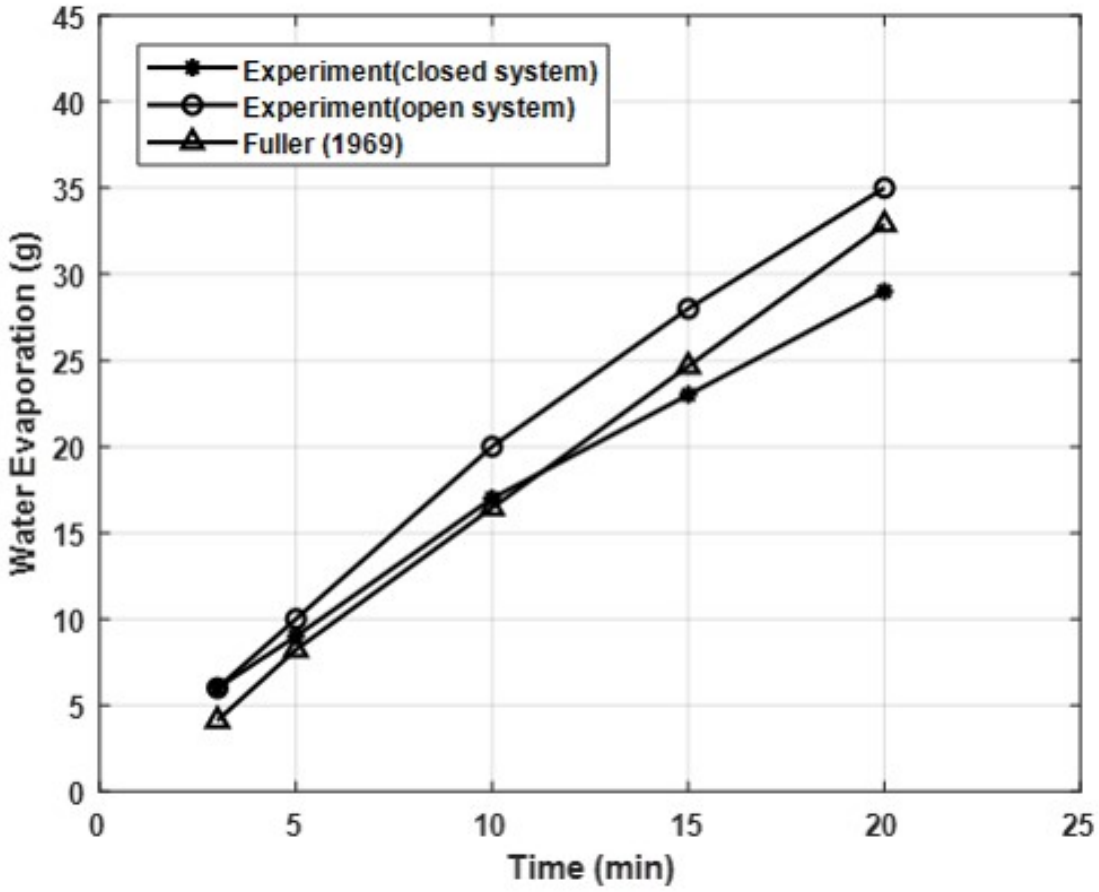

Figure 4.3: Total amount of evaporation water at different times with a constant temperature of 55°C.

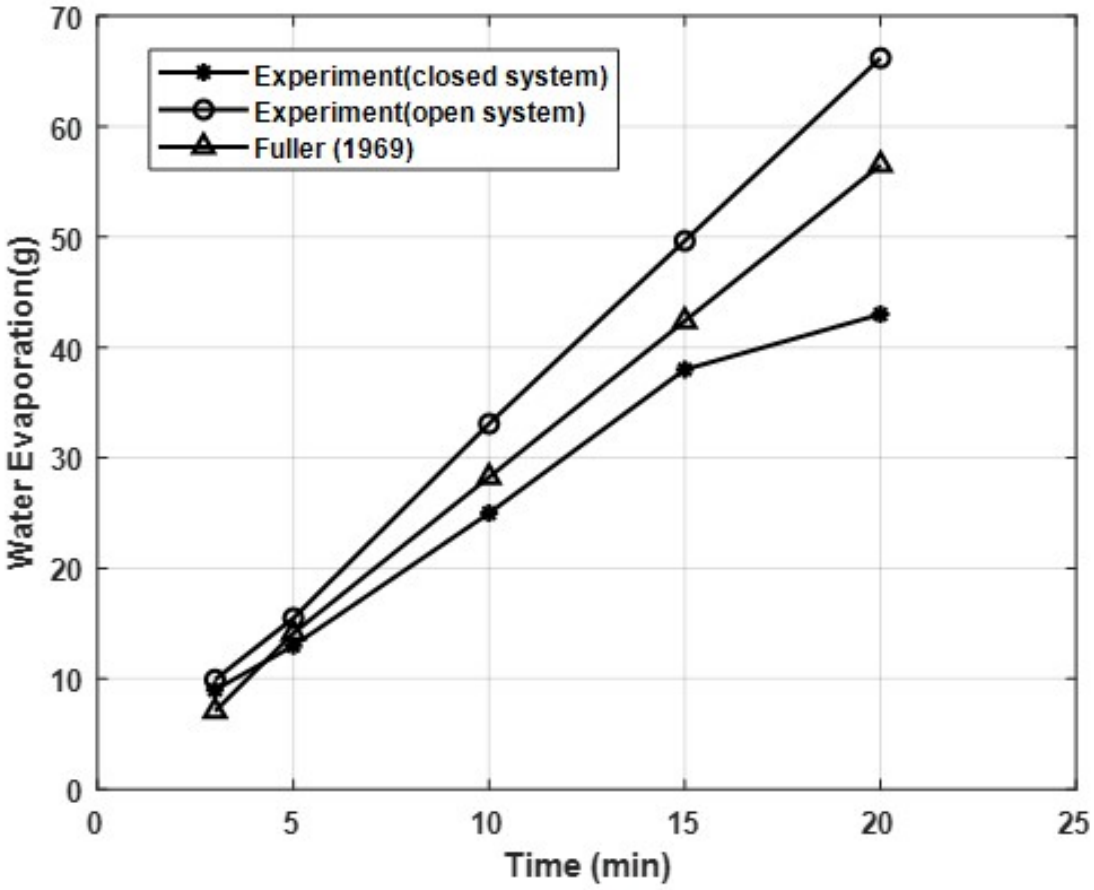

Figure 4.4: Total amount of evaporation water at different times with a constant temperature of $65°C$.

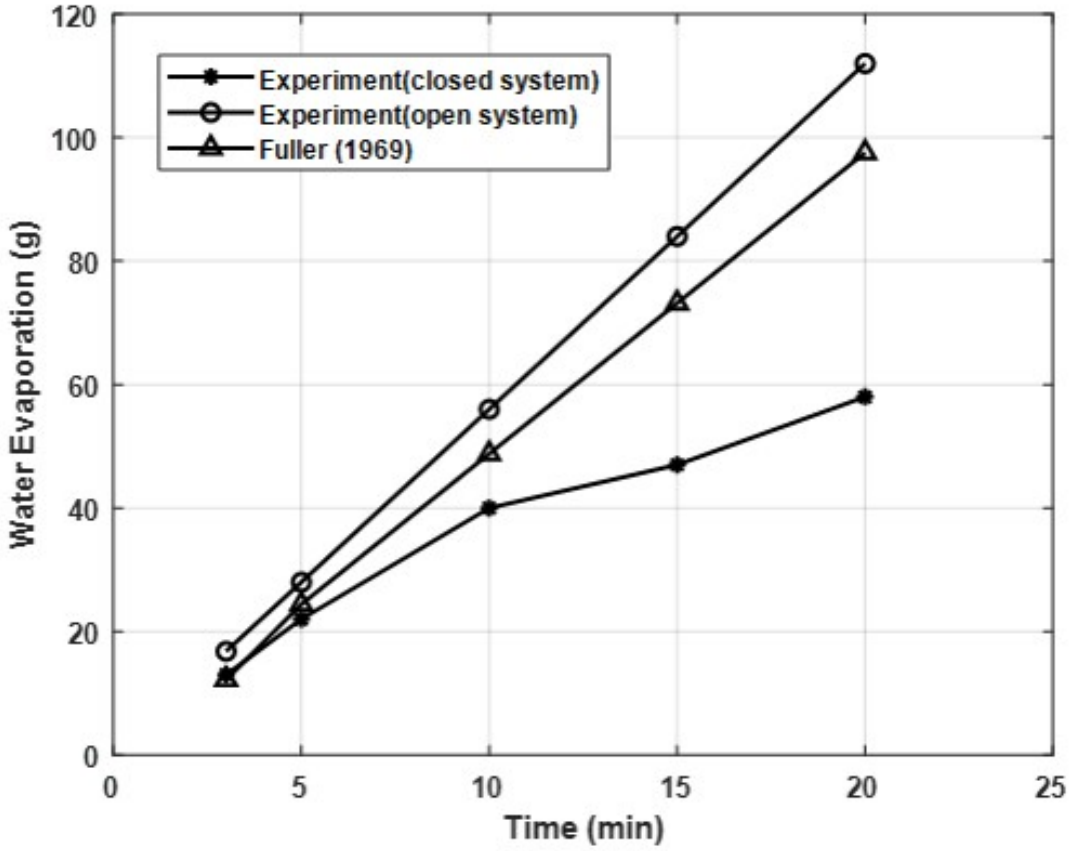

Figure 4.5: Total amount of evaporation water at different times with a constant temperature of $75°C$.

Chapter 5

Experimental Setup and Measuring Techniques for Condensing Water Vapors

This chapter describes the experimental setup used during this work. The purpose of the experimental portion of this paper is to investigate the mechanism of water vapor condensation as a result of the TICP device. In addition, the effect of pressure, temperature and velocity in the amount of water vapor generated was considered.

5.1 Experimental Description

The experiment is comprised of a container that has a diameter of 266.7 mm and a height of 203.2 mm, also has two holes on both sides. The first hole is connected to a valve in order to control the main air flow into the system and the second one is connected to an acrylic pipe, which is included the condensing system TIPC, has a length of 914.4 mm and diameter of 15.875 mm. In addition, the container is heated up from the bottom at a specific temperature by a heat source, is controlled by the power supply. The turbulence-induced particles collision (TIPC) device is conducted by all designs through the experiment. The experiment set up is shown in Figure 5.1.

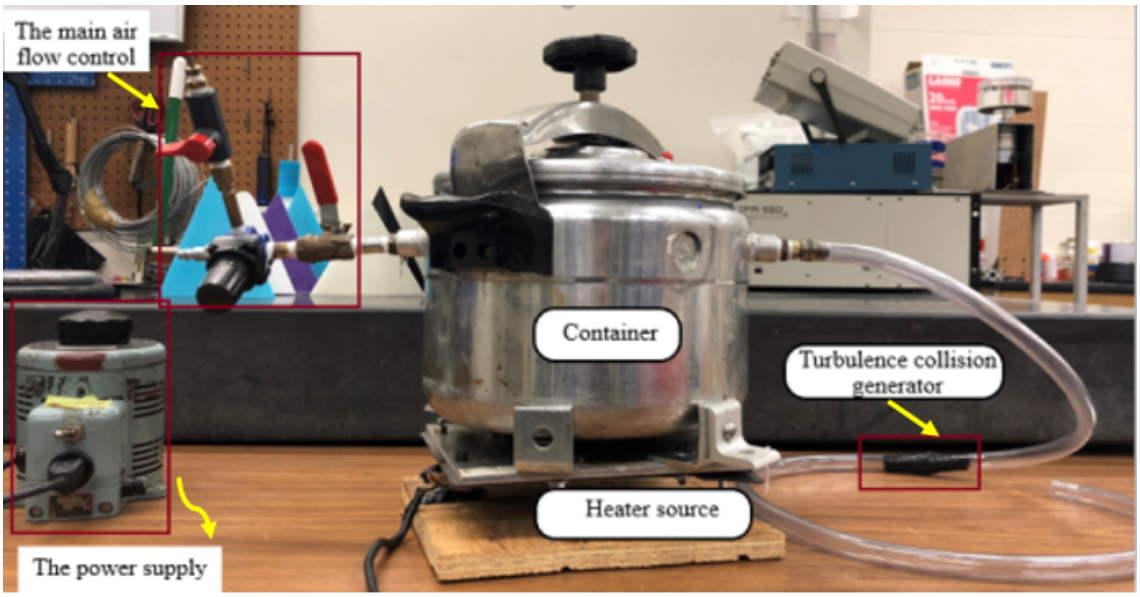

Figure 5.1: Experimental setup for the modeling.

5.2 Steps of Data Measurements

To collect the data from the experiment, paper towel is used as a reference by recording its weight before and after running each experiment. The weight scale used for measurements has an accuracy of 0.01 g. Initially, the container is filled up with 25.4 mm of water. In order to improve the accuracy of the results, heat and air flow pressure are maintained to be constant throughout the experiment. The heat source is measured using a temperature laser sensor and controlled by the power supply. The air flow pressure is measured with a digital manometer and controlled by two valves, the first one controlling the main source flow and the second one controlling the air flow inlet to the system.

The experiment is conducted by heating the water for 5 minutes in order to fill up the empty volume by water vapors. After that, the water vapors are transferred to the TIPC for 2 minutes using the air flow pressurized . Finally, the initial and final weights of a paper towel are used to calculate the total amount of water produced by the TIPC device. The measurement tools used throughout the experiment are shown in figure 5.2.

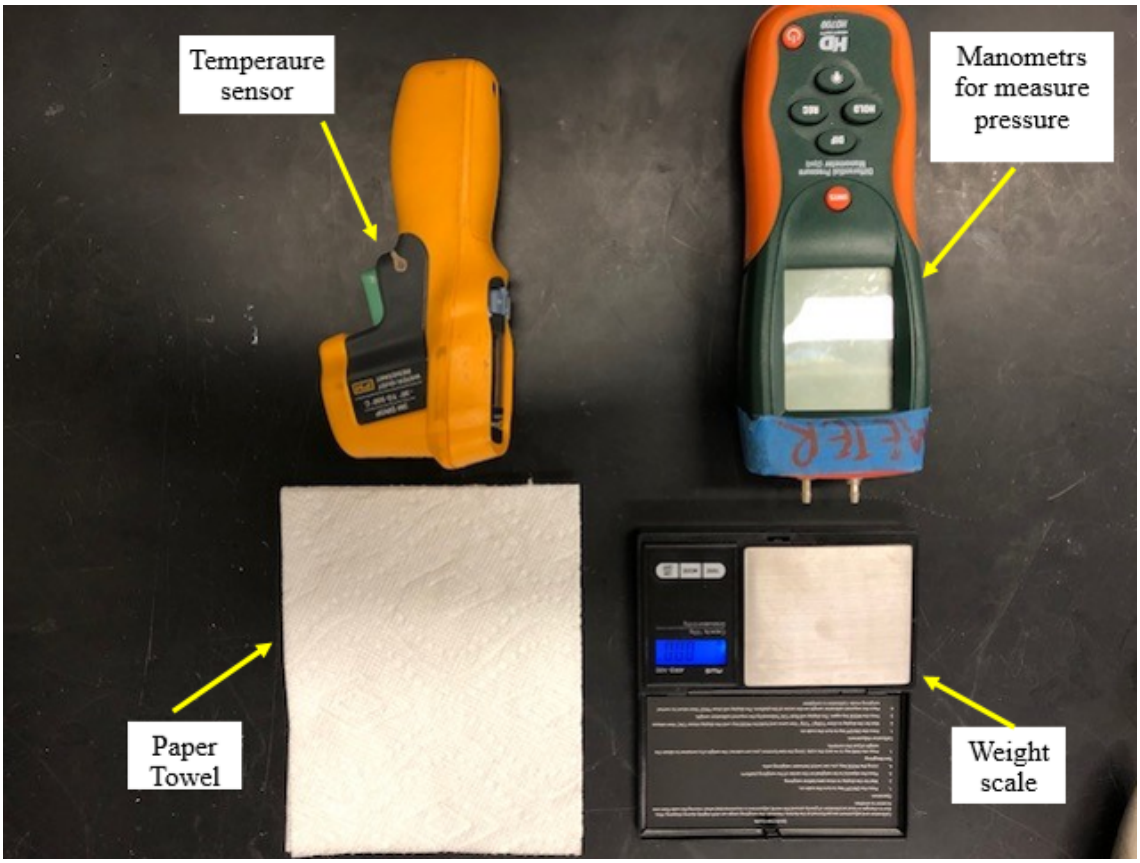

Figure 5.2: Measurement tools for collecting data.

5.3 Experimental Results

The amount of water production as a result of the TIPC device is measured at three different values of temperature 55°C , 65°C and 75°C. Figure 5.3 shows the water production rate as a function of the number of experiment for the configuration 1(A) of the TIPC device with different values of temperature 55°C , 65°C and 75°C, indicating the increasing water production with rising temperature. The water production due to the configuration 1(B) of the TIPC device is presented in figure 5.4, the production rate of water has the similar rate of production with some increasing at 75°C. The similar behaviors of the water production rate for the configuration 1(C) is shown in figure 5.5. The results of other configurations of the TIPC device have similar conducts for water production rate that is affected by increasing temperature. Figures 5.6 , 5.7 , 5.8 and 5.9 show the water production rate as a function of experiment number for configurations 2(A), 2(B), 3 and 4, respectively, of the TIPC device.

RMS error is calculated for each configuration of the TIPC device to compare between models for all configurations. Figure 5.10 shows the water production rate as a function of the temperature for different models of configuration 1 of the TIPC device, indicating the increasing water production with increasing temperature. The models (B) and (C) of configuration 1 give the maximum production of water $75°C$ comparing with model (A). The similar behaviors of the results with less water production for the configuration 2 models (A) and (B) are shown in figure 5.11. The rate of water production is not dramatically changing between models of configuration 2. The last 2 configurations 3 and 4 are designed focused on increasing the surface area of the TIPC device. Figure 5.12 shows the water production rate as a function of the temperature for configurations 3 and 4. The production of water is increasing at a fixed rate with raising the temperature for both configurations 3 and 4 with small change of water production amount. The pressure effect of two values on the TIPC device is presented in figure 5.13, indicating that the high pressure has an insignificant impact on improving the water production amount from water vapor. Increasing the pressure is just reduced the time of blowing the water vapor to the TIPC device because the water vapor is evaporated at a constant rate. Figure 5.14 shows the water production rate as a function of the temperature for single, double and three of using the TIPC device. The effect is not very large on the production of water.

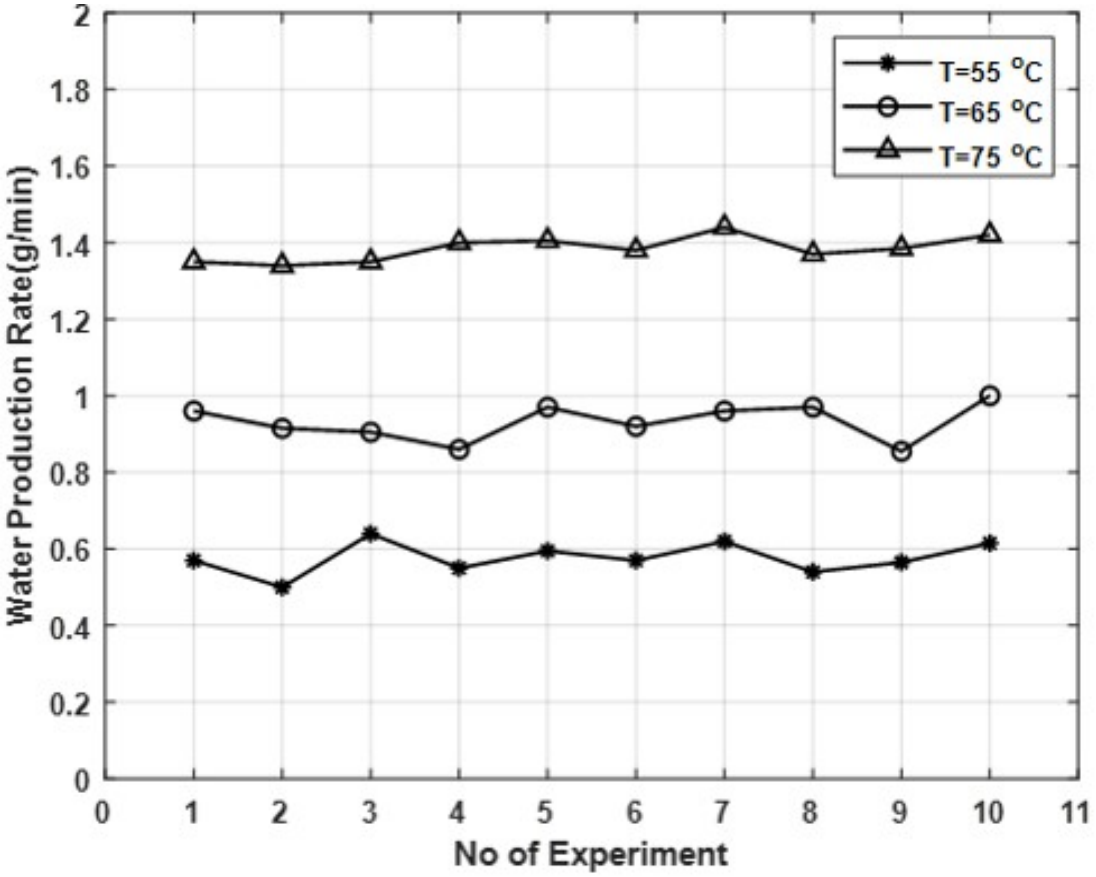

Figure 5.3: The water production rate as a function of experiment number for the configuration 1(A) at different values of temperature 55, 65 and 75$^{\circ}C$.

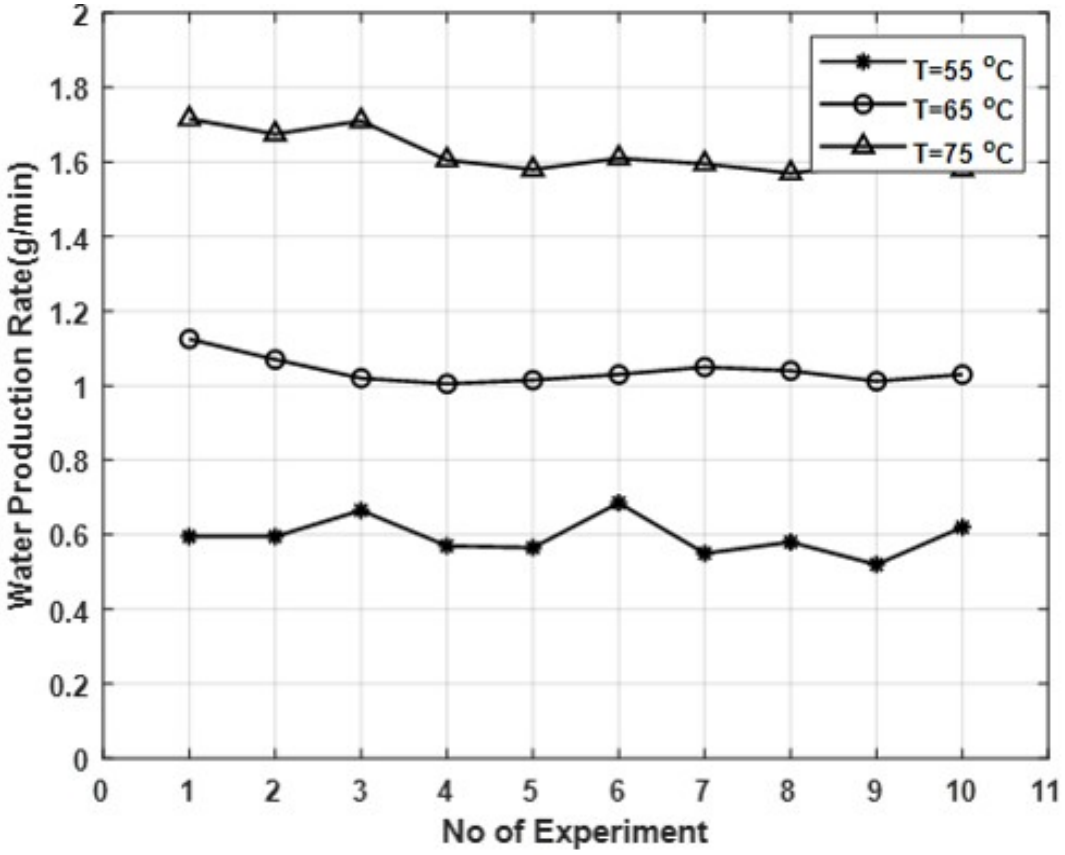

Figure 5.4: The water production rate as a function of experiment number for the configuration 1(B) at different values of temperature 55, 65 and 75°*C*.

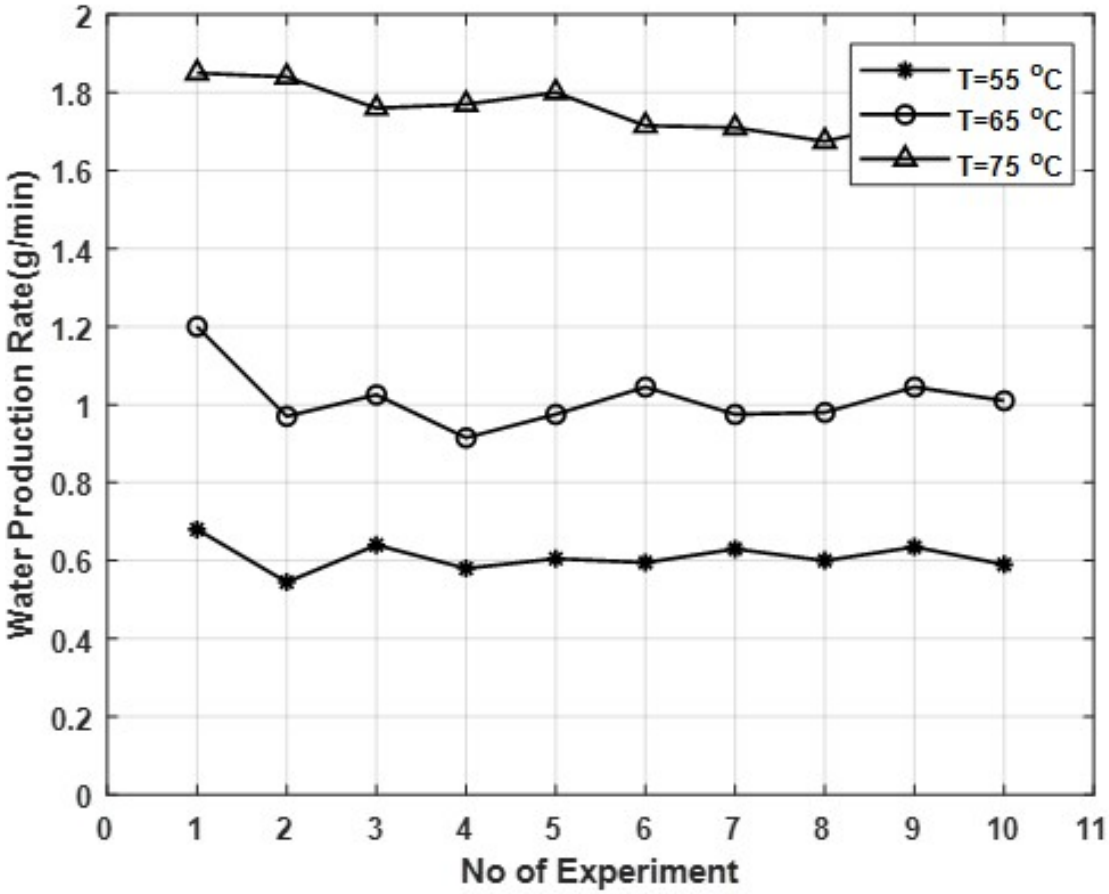

Figure 5.5: The water production rate as a function of experiment number for the configuration 1(C) at different values of temperature 55, 65 and 75°C.

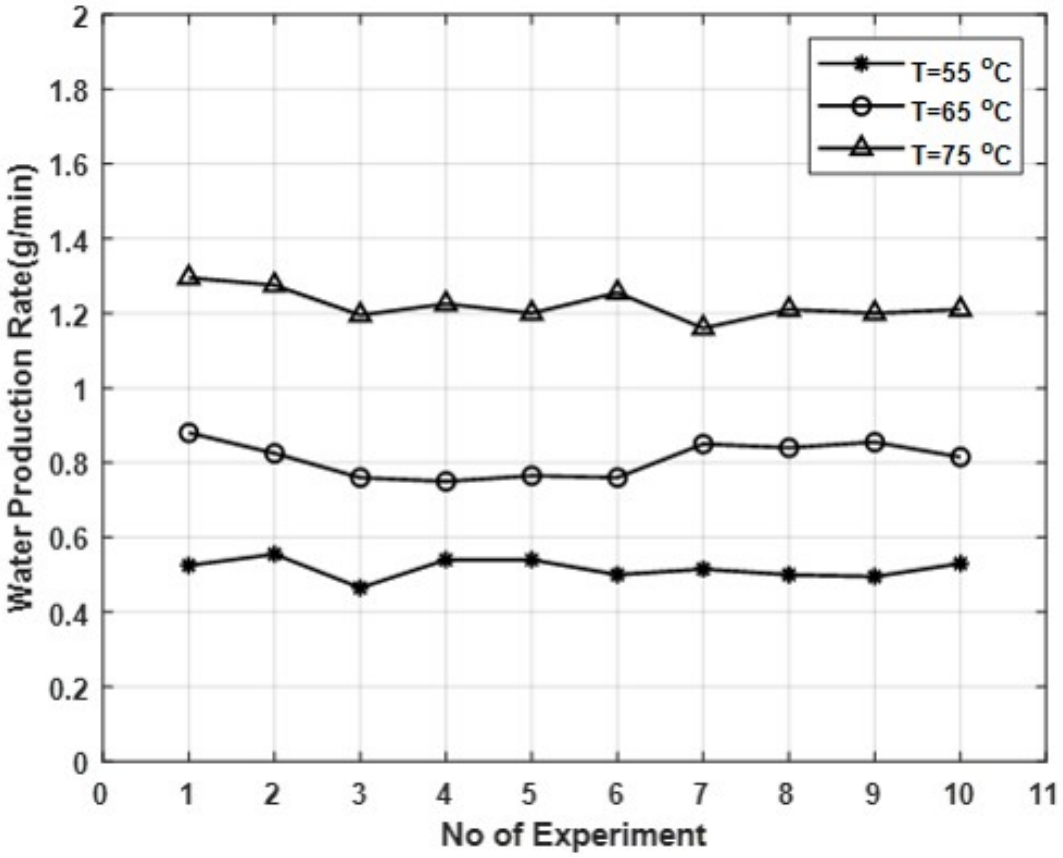

Figure 5.6: The water production rate as a function of experiment number for the configuration 2(A) at different values of temperature 55, 65 and 75$^{\circ}C$.

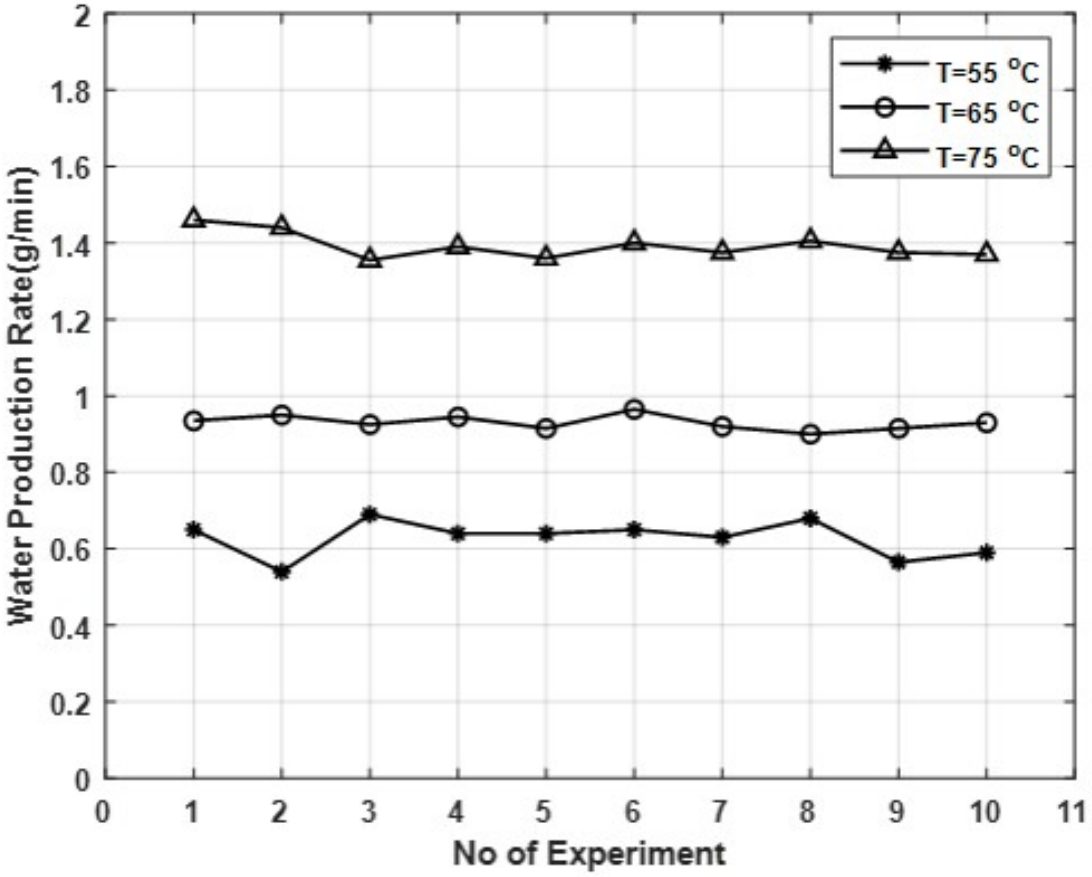

Figure 5.7: The water production rate as a function of experiment number for the configuration 2(B) at different values of temperature 55, 65 and 75°C.

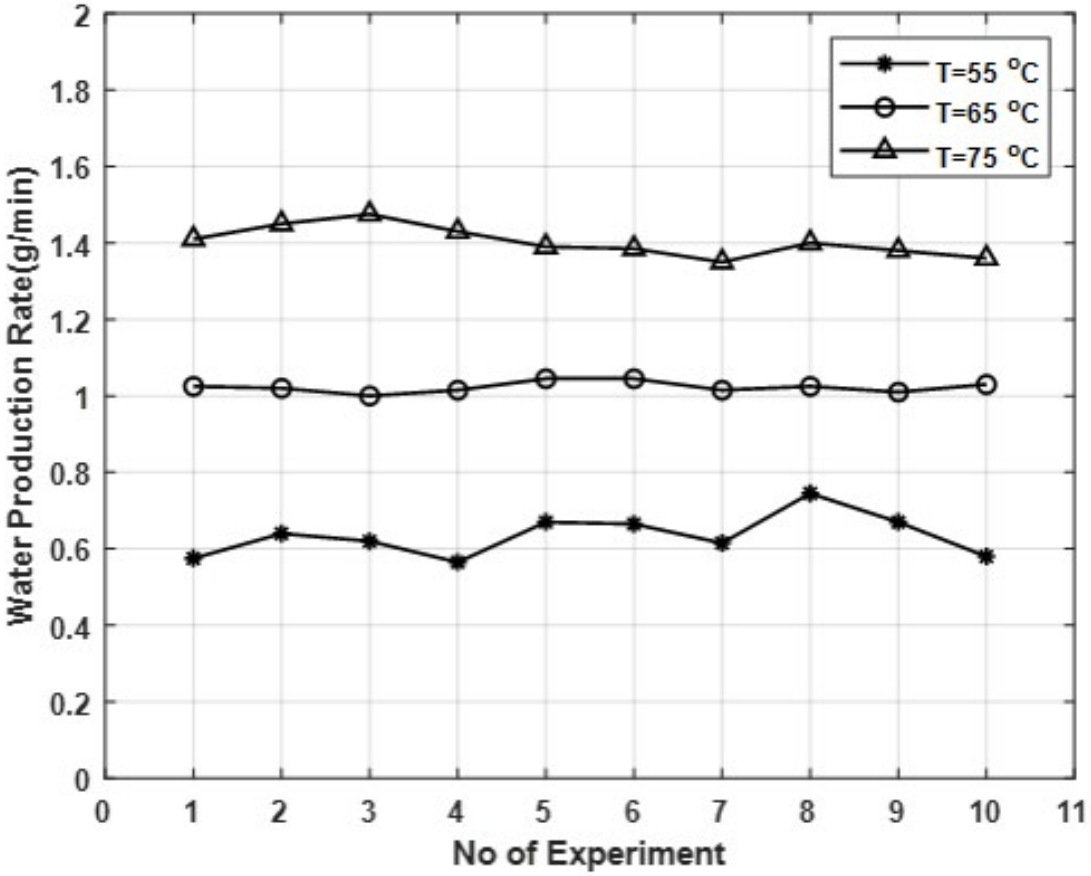

Figure 5.8: The water production rate as a function of experiment number for the configuration 3 at different values of temperature 55, 65 and 75$^{\circ}C$.

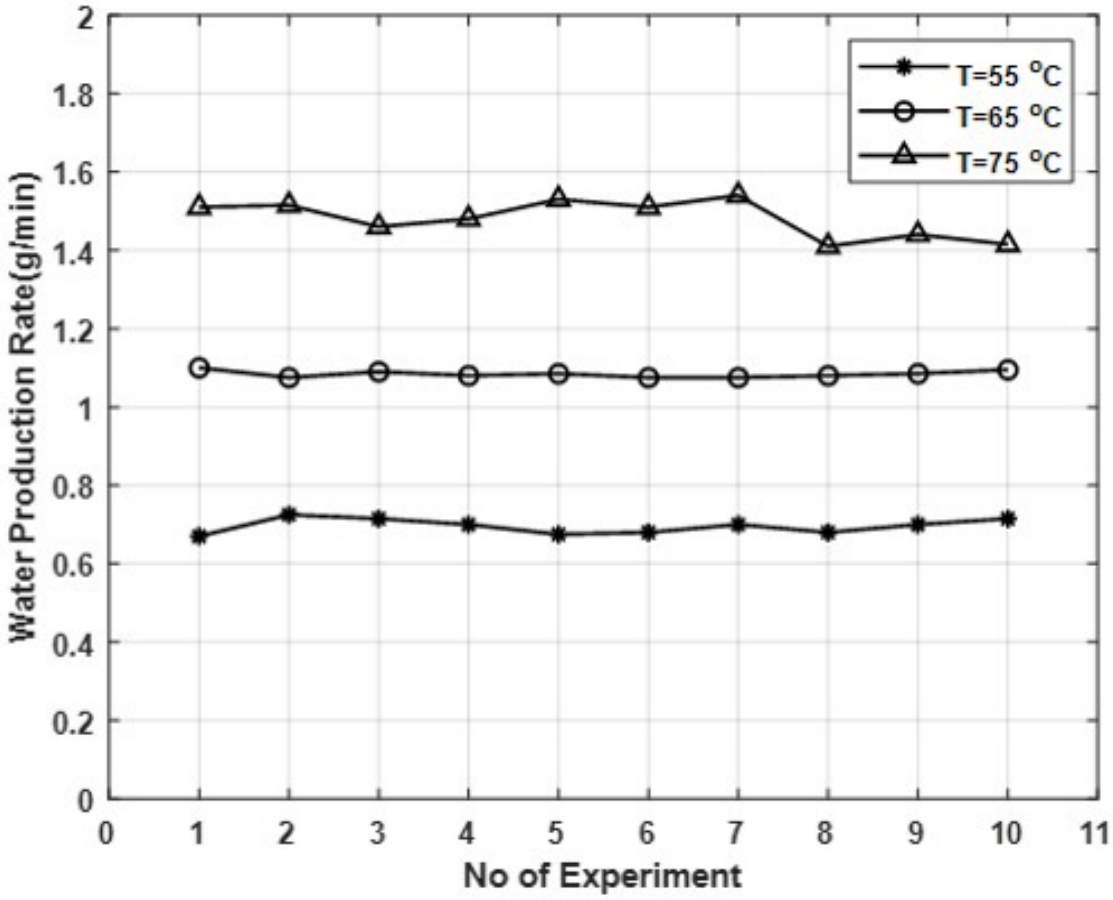

Figure 5.9: The water production rate as a function of experiment number for the configuration 4 at different values of temperature 55, 65 and 75$^{\circ}C$.

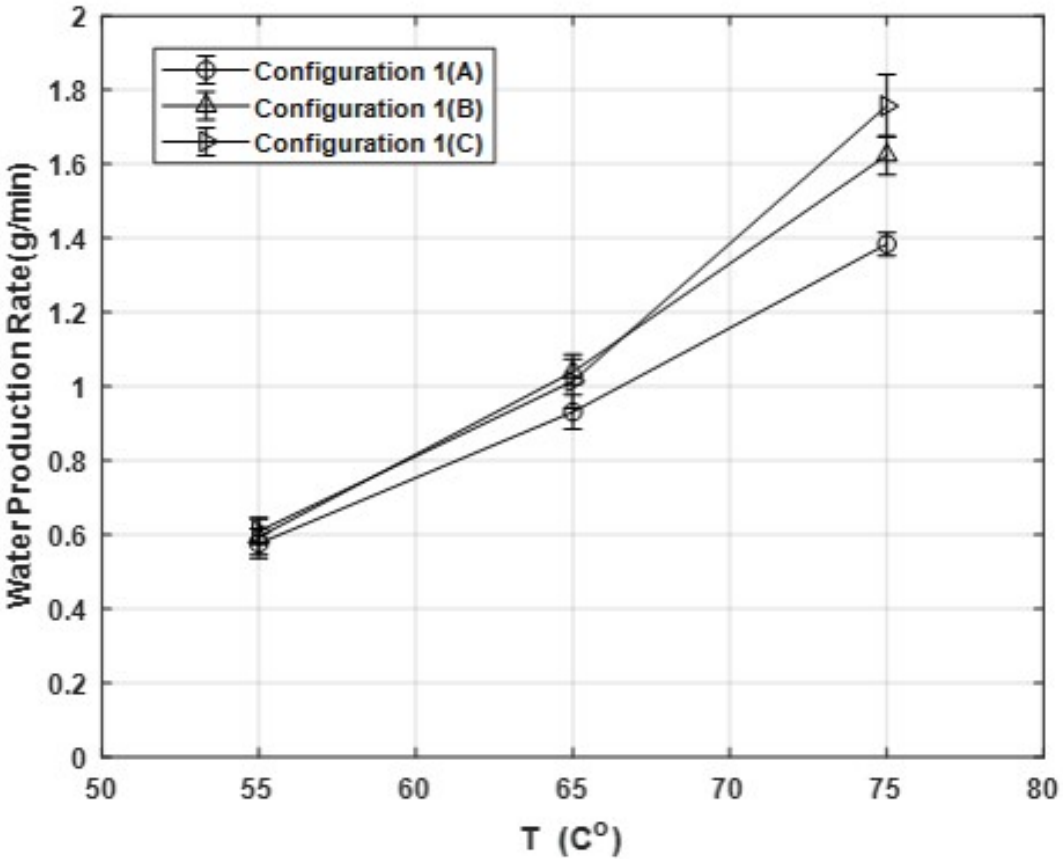

Figure 5.10: The water production rate as a function of temperature for models of configuration 1 (A), (B) and (C).

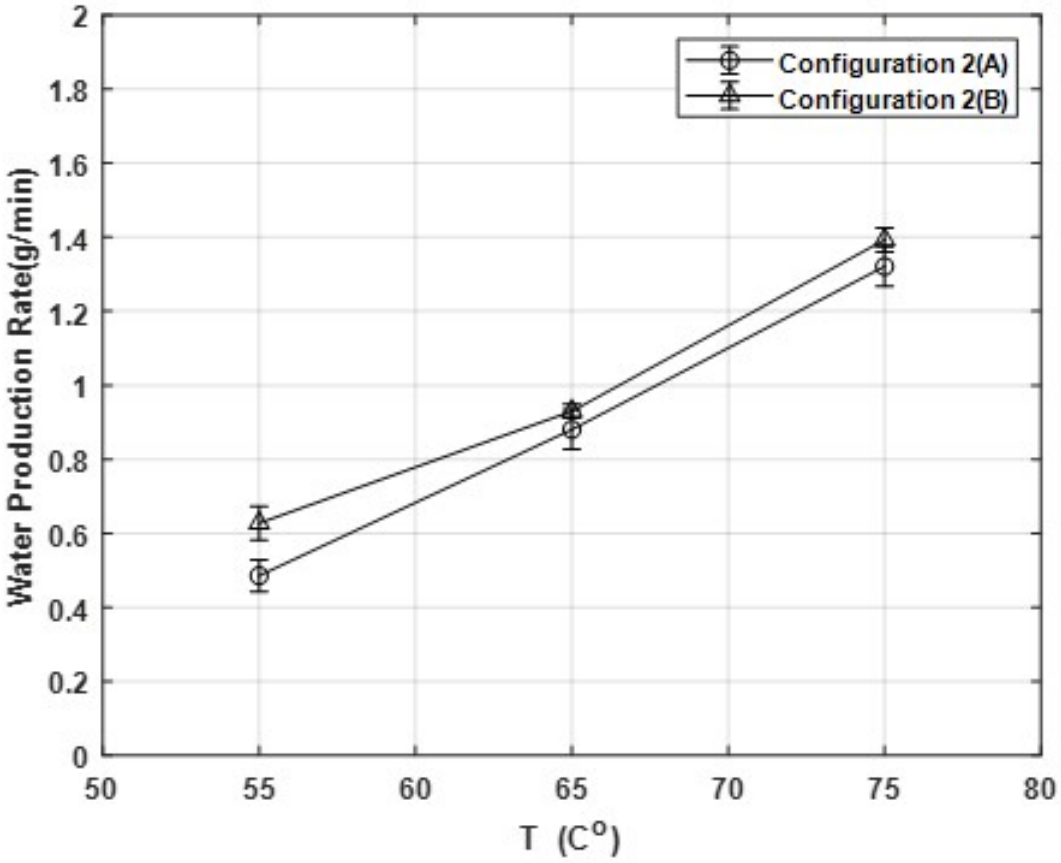

Figure 5.11: The water production rate as a function of temperature for models of configuration 2 (A) and (B).

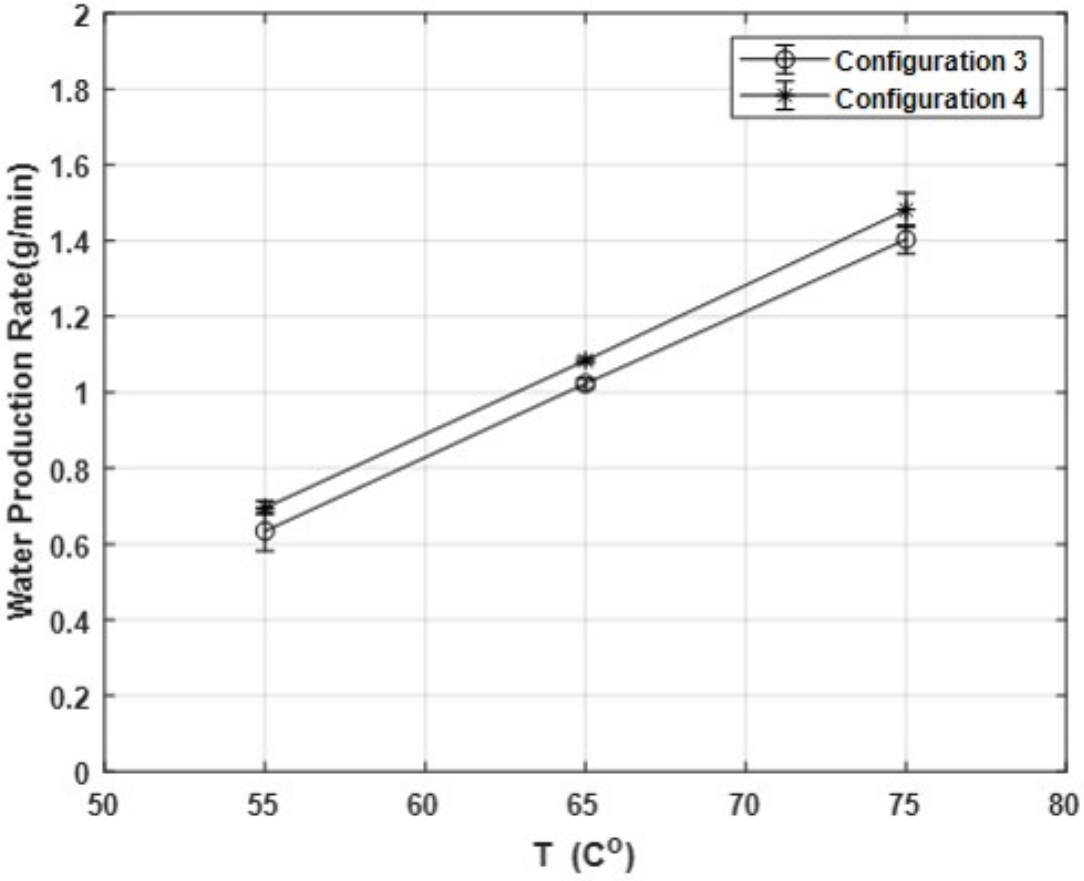

Figure 5.12: The water production rate as a function of temperature for configurations 3 and 4.

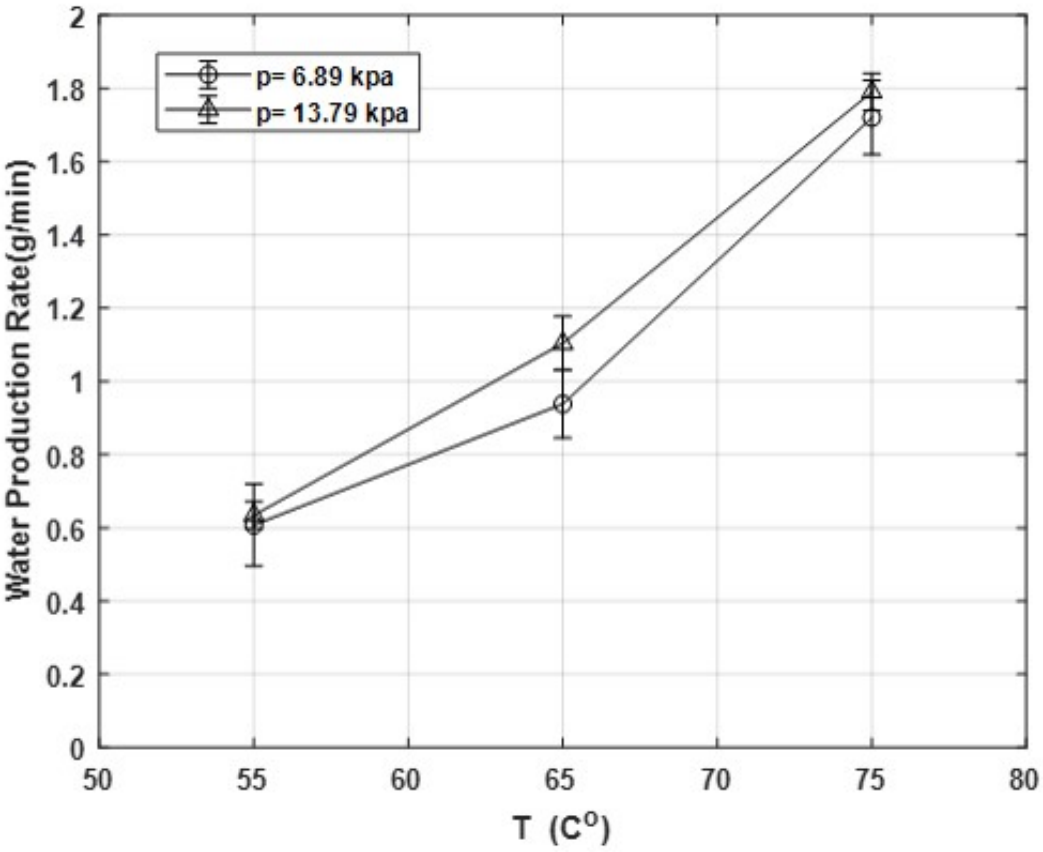

Figure 5.13: The water production rate as a function of temperature for two values of air pressure 6.89 kpa and 13.79 kpa.

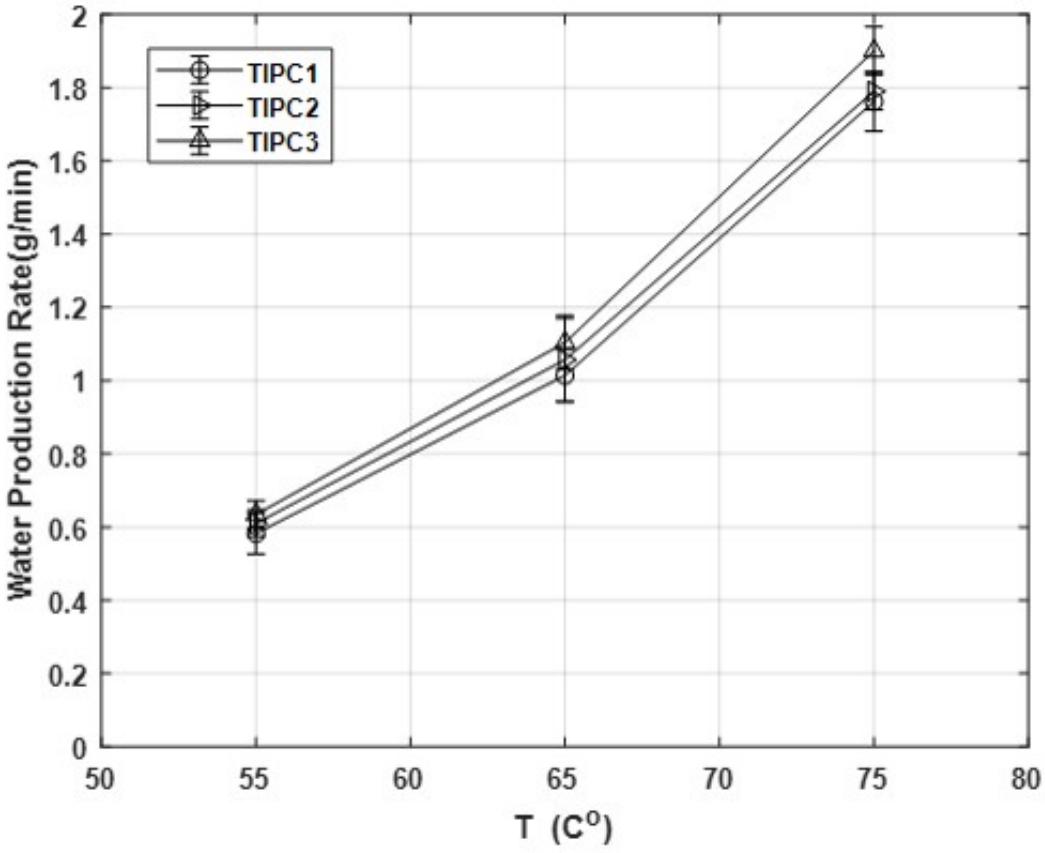

Figure 5.14: The water production rate as a function of temperature for applying single, double and three devices of TIPC.

Chapter 6

Droplets Collision Visualization

To visualize the collision of the droplets in the TIPC device, the luminescent oil dye is used in order to mix with the olive oil in the atomizer. Figure 6.1 shows the oil production rate as function of pressure. The amount of oil is increasing with rising the inlet pressure to the atomizer. The pattern of particles deposition due to the effect of the TIPC is studied in two different ways. First, the particles are projected directly on the plate after passing through the TIPC generator. Second, visualizing the deposition of particles on the inner diameter wall of the pipe due to the TIPC device is obtained.

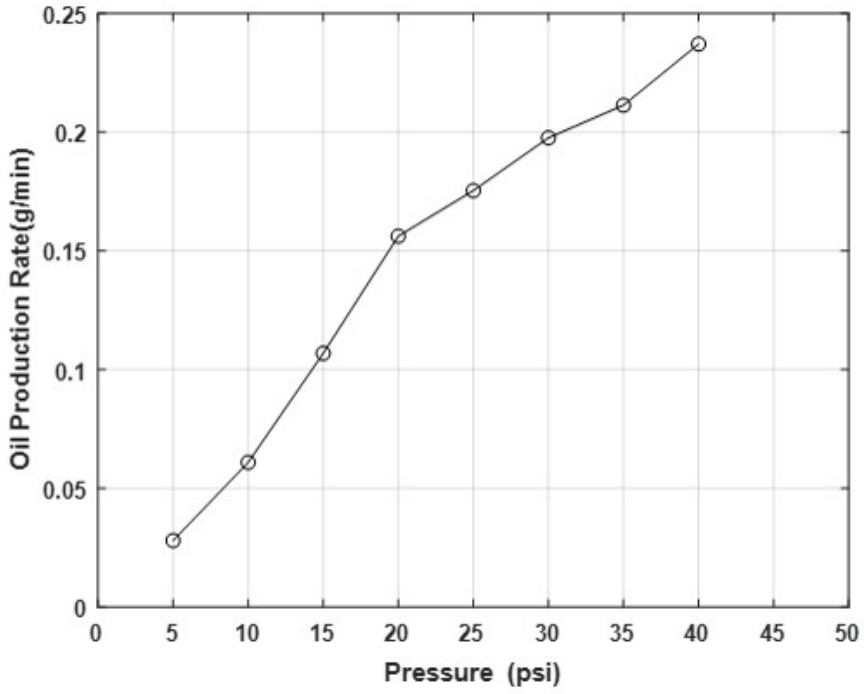

Figure 6.1: The oil production rate as a function of pressure.

6.1 Deposition of Droplets on Plate

To provide a better clarification between the different models of the TIPC approach in terms of efficiency, the impact of droplets deposition on the plate for each model is investigated experimentally by visualization. The main parts for visualizing are composed of an oil atomizer in order to generate particles. The atomizer is connected to the TIPC device using a tube. A solid glass plate is used to make the particles visible through the deposition. A compressed air line is used for feeding air into atomizer by control valve at specific regulated air pressure. The luminescent oil dye has been used for visualization, and two UV lamps are used for excitation luminescent particles. A Basler camera with a pass filter is used for detecting. figure6.2 presents a diagram of the main facility parts for visualization.

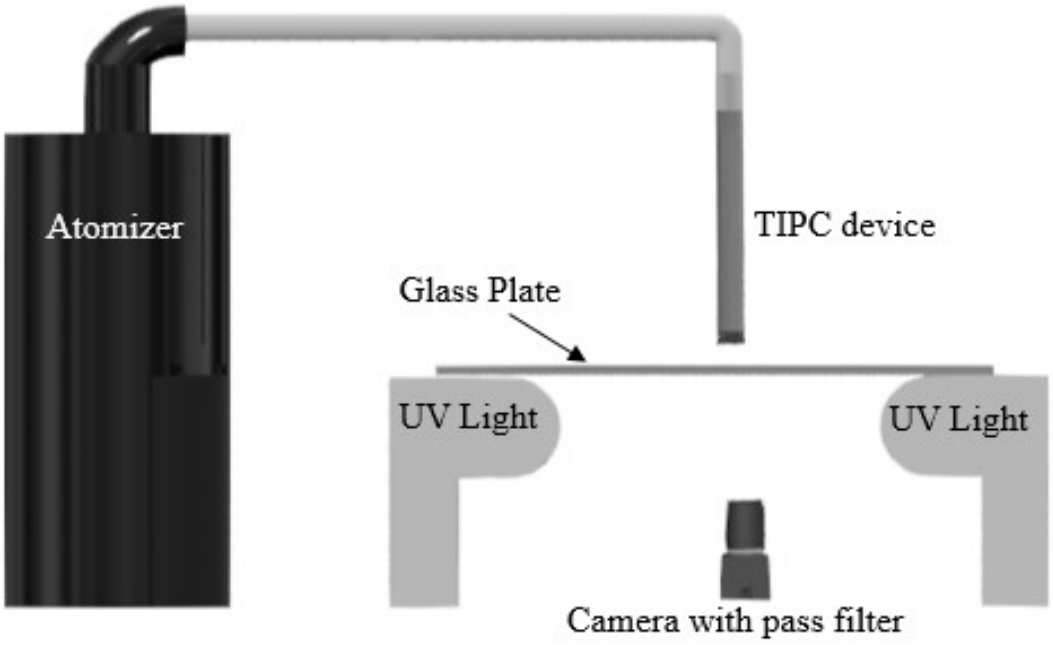

Figure 6.2: A diagram of the main facility parts for visualization.

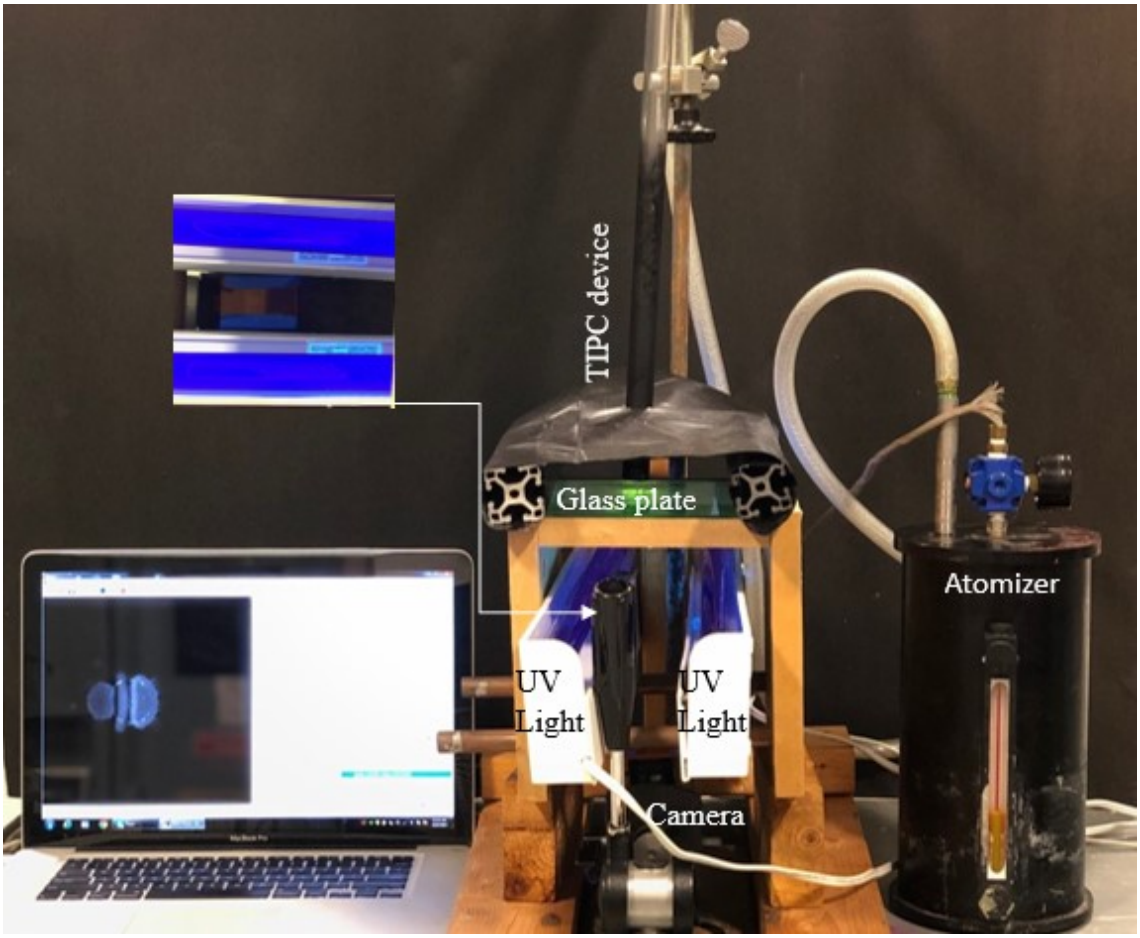

Figure 6.3: A diagram of the main facility parts for visualization.

6.1.1 Experimental Setup

The arrangement of experimental parts through the setup is very important in order to gain a perfect visualization for the deposition particles on the plate surface. The TIPC device is placed perpendicular to the top surface of a plate while the camera with pass optical filter is fixed from the bottom of the plate surface to be focused on the projected area of the TIPC device. Also, two UV lights are placed on both sides for the camera in order to excite the luminescent oil. Since the intensity of luminescent is proportional to the oil thickness on a plate surface. Black Sheet has been used as a background from the top to prevent the effect of light reflection. The experiment setup is presented in figure6.3. The experiment is running after sitting the pressure of air flow into the atomizer, the UV lights and camera where turned on. The air is leaving the atomizer, with a

mixture of droplets olive oil and luminescent oil, through a 15 mm clear vinyl tube. It is connected to a 15.785 mm acrylic pipe which has the TIPC device at the exit. The droplets are projected from the TIPC device vertically onto the plate surface for a certain time. The camera captures the change of the luminescent oil thickness due to emission using UV lights. The distance of the TIPC device to the plate surface is 0.5 mm. It is constant through all experiments. Before each test, the acetone is used to clean the plat surface and the pipe exit in order to get rid of the luminescent oil droplets around the TIPC device. In this study, several models of the TIPC device have been tested. The first model is a cylinder shape with two different diameters. The second model is a plate shape with two different widths. The third model is an oval body shape. The fourth model is a cylindrical rod shape. The first three shapes are placed in vertically while the last shape is placed in horizontally to the pipe. The effect of velocity on each model is investigated at two different pressures, 5 psi and 20psi.

To evaluate the efficiency and the impact of pressure for each model of the TIPC design, 200 consecutive images have been taken for 20 seconds with an average of 10 frames per second (fps). Each design has a special pattern of distribution during deposition. The results are extracted based on the deposition velocity of oil droplets by using Optical flow open source [43]. The ensemble-averaged of the velocity field is calculated. Also, the averaged intensity difference between 200 images is calculated for each model using MATLAB code.

6.1.2 Configuration 1 of the TIPC System

The first configuration is a cylinder model. Figure 6.5 shows the luminescent intensity images of the deposition of particles at different times for the cylinder design (TIPC) with a diameter of D = 12.7 mm and at a pressure equal to 5 psi. The raw images in figure6.4 present the pattern of deposition particles due to increasing the pressure to be equal to 20 psi. The cylinder diameter is reduced to be 10.16 mm and tested at the same values of pressure respectively, 5 psi and 20 psi. Figures 6.6 and 6.7 show the luminescent intensity images of particles deposition for two pressures. Clearly, the effect of high pressure and large diameter are more effective in raising the velocity and the amount of particles deposition. At pressure 20 psi, two big droplets are formed directly on the wall at t = 5 s in the cylinder shape (TIPC) by a 12.7 mm and a 10.16 mm, respec-

tively. The pattern of deposited droplets is more rapidly and heavily deposited for large diameter. Also, it is observed that the diameter of two big droplets is about 4 mm at the stagnation point. Figures 6.8 and 6.9 explain the ensemble-averaged of oil distribution velocity at two pressures for each cylinder diameter (12.7 mm and 10.16 mm).

The change of intensity is illustrated the concentration of oil thickness due to the deposition [44]. The averaged intensity difference between 200 images is calculated by the integrated intensity of deposited particles with respect to time. Figure6.10 shows the integrated intensity of deposited particles for a large cylinder diameter (D = 12.7 mm) at two different pressures. At the same conditions of pressure values, the integrated intensity of deposited particles for a small cylinder diameter (D = 12.7 mm) is presented in figure6.11. It can be noticed that based on the results of the integrated intensity of deposited droplets for both cylinder diameters, the pressure at 20 psi is led to increasing the amount of luminescent oil deposition.

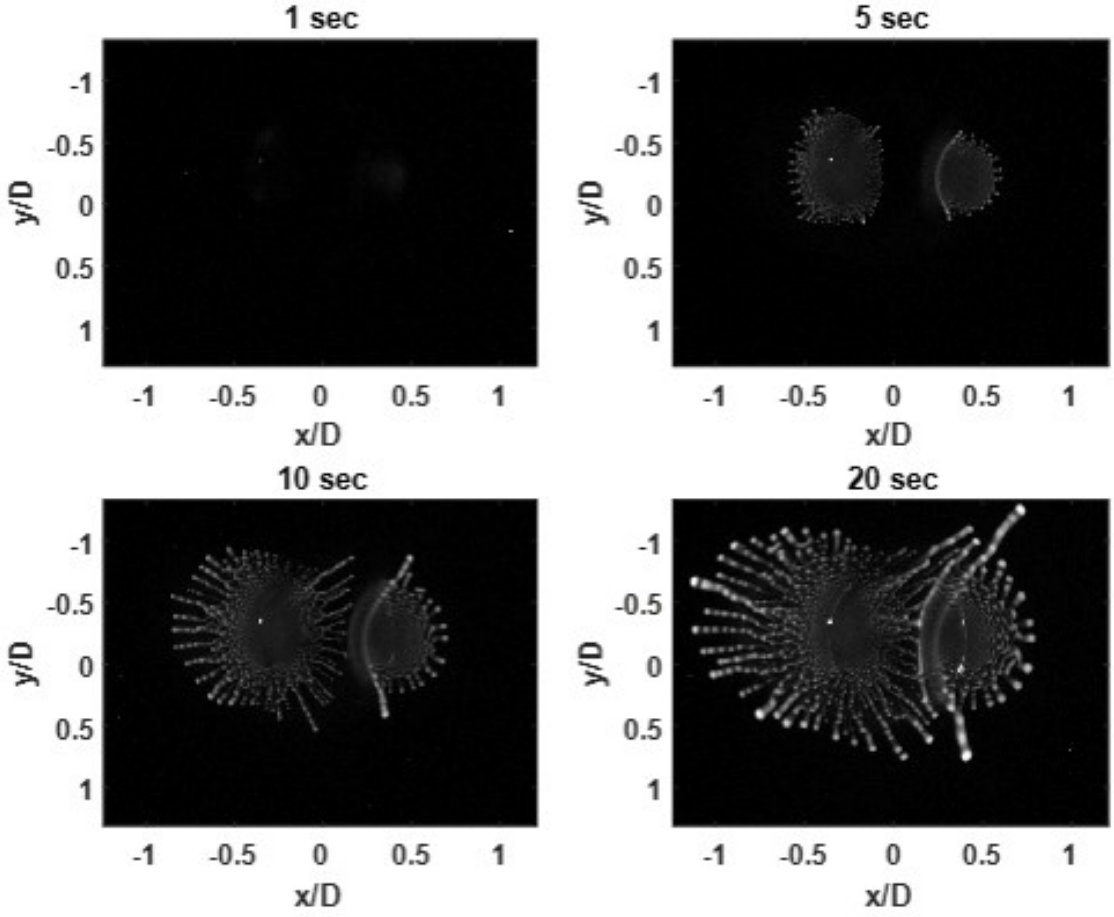

Figure 6.4: luminescent intensity images of particles deposition at different times as a result of Cylinder shapes (D =12.7 mm, 5 psi).

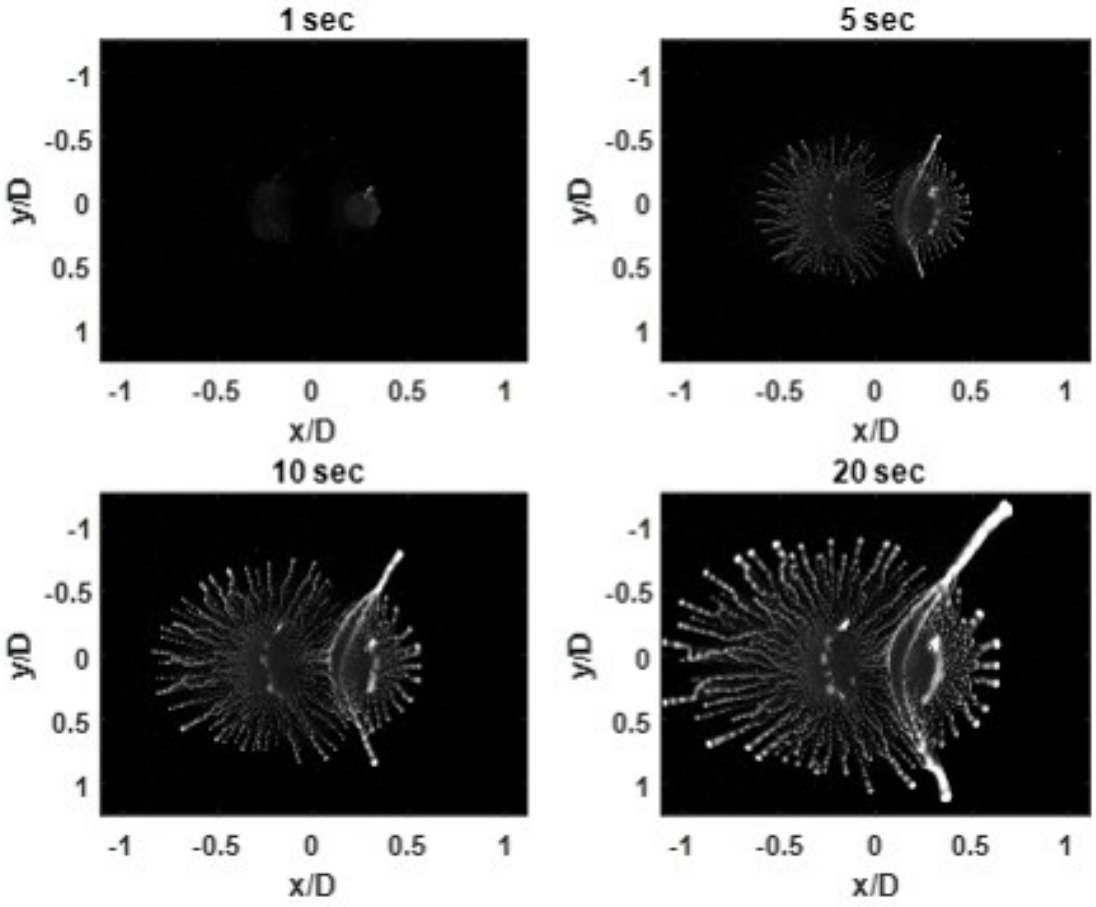

Figure 6.5: luminescent intensity of particles deposition at different times as a result of Cylinder shape (D =12.7 mm, 20 psi).

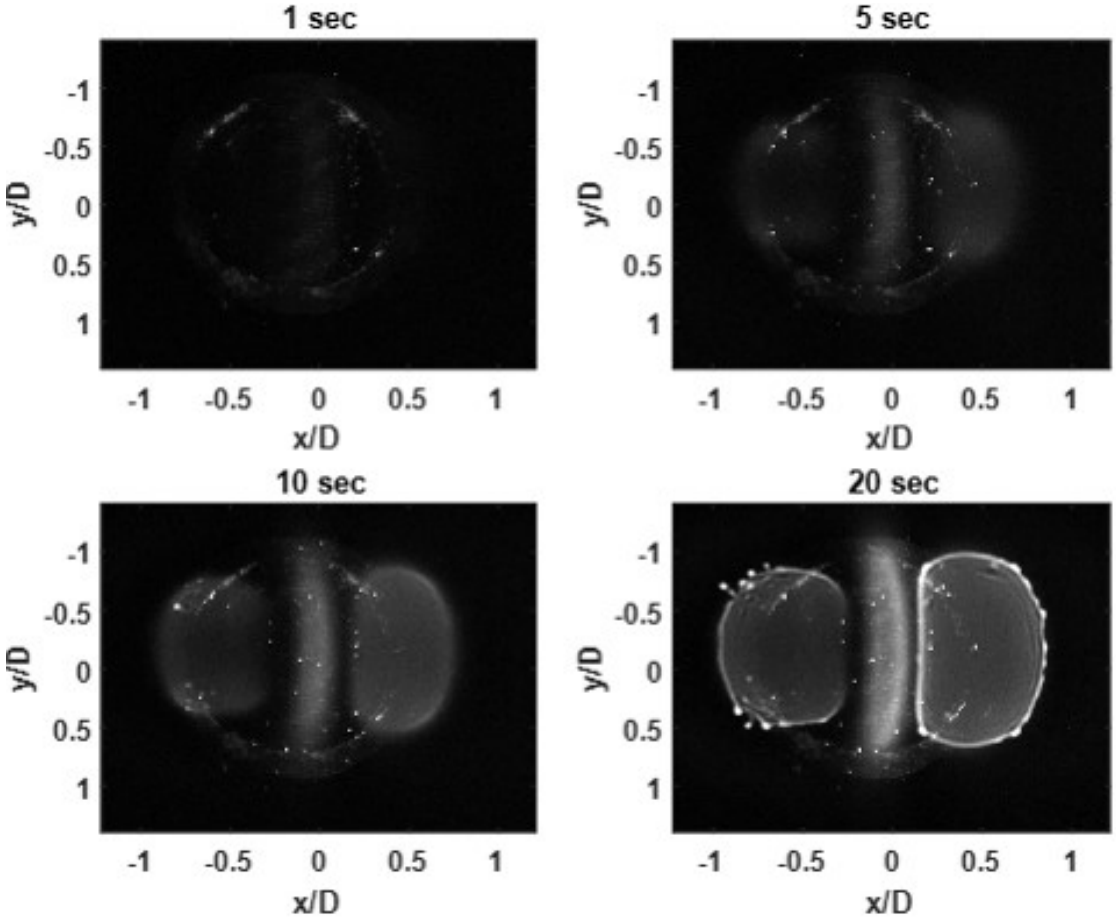

Figure 6.6: luminescent intensity of particles deposition at different times for Cylinder shape (D =10.16 mm, 5 psi).

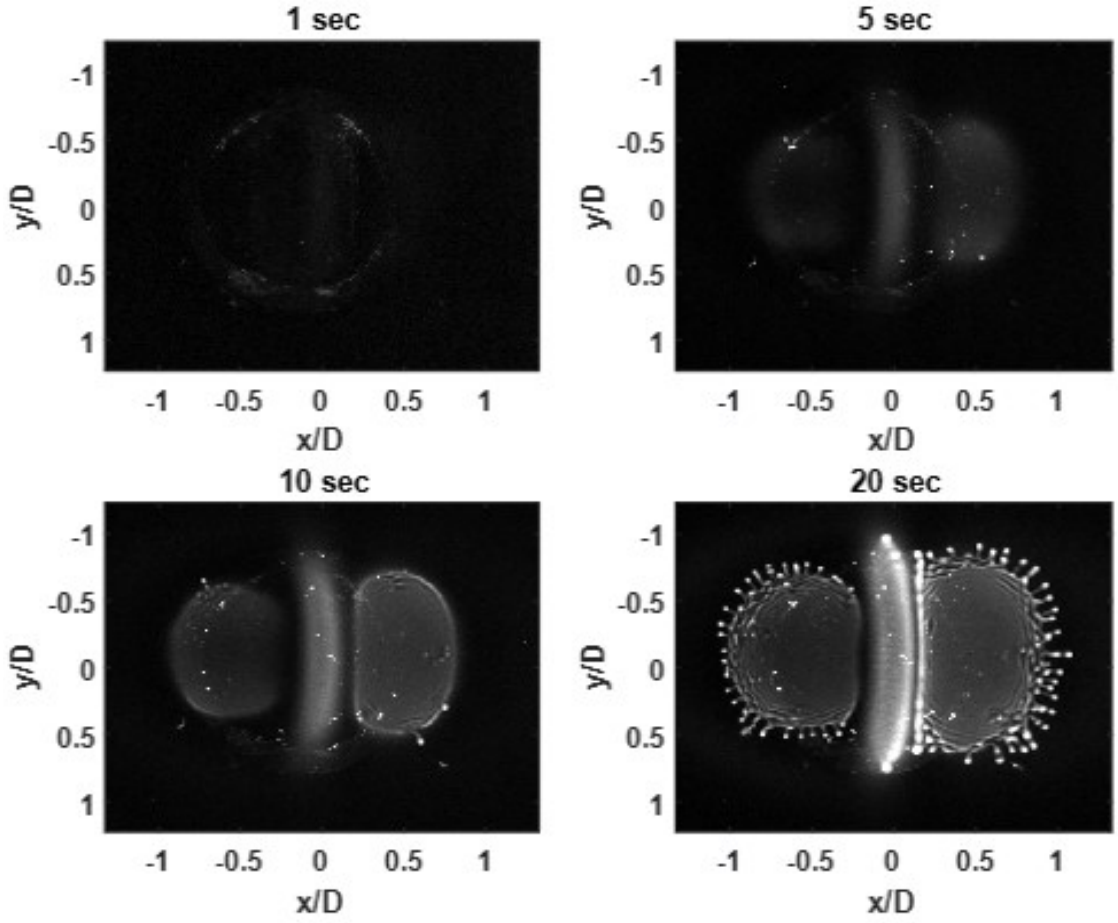

Figure 6.7: luminescent intensity images of particles deposition at different times for Cylinder shape (D =10.16 mm, 20 psi).

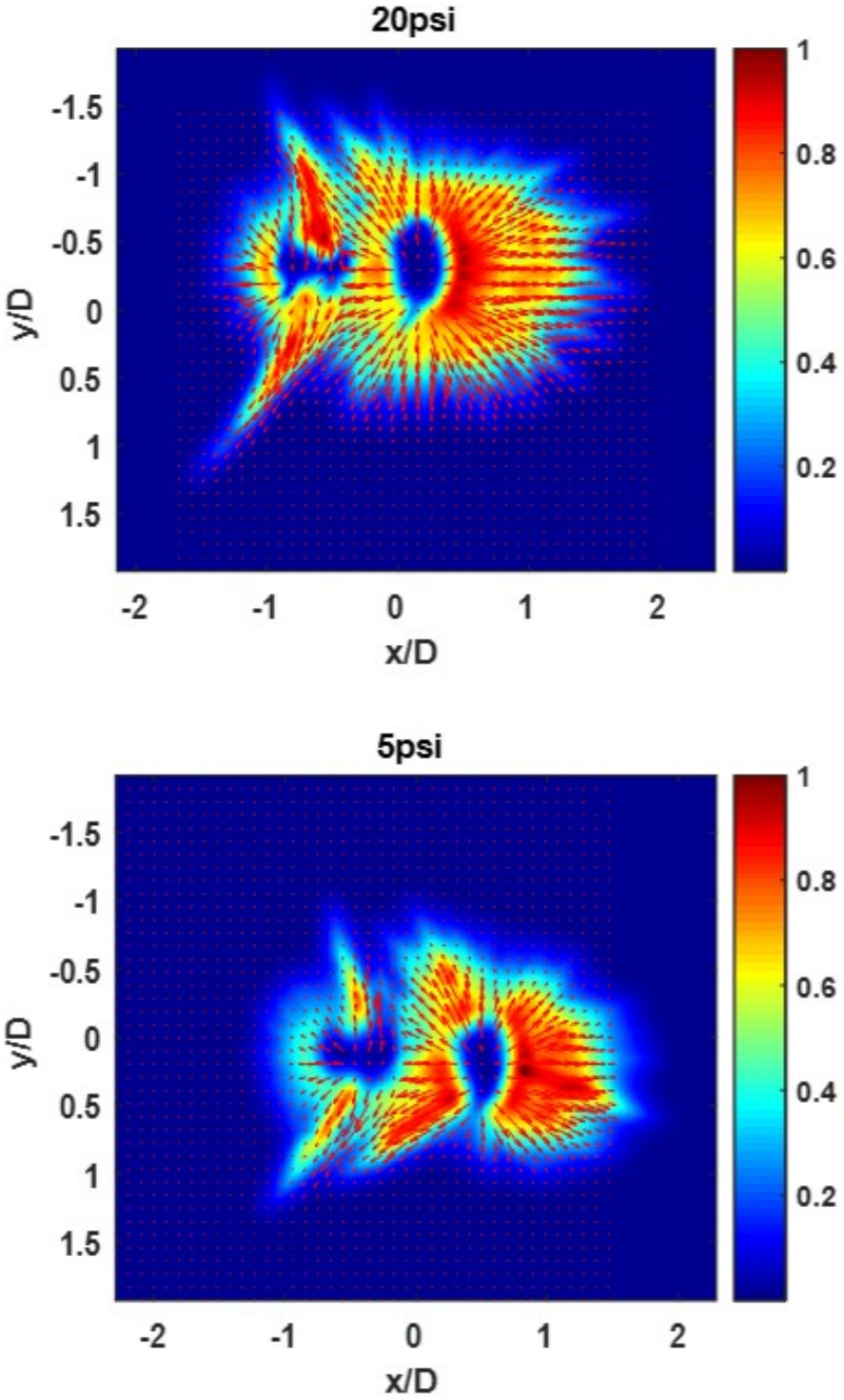

Figure 6.8: Ensemble-averaged velocity magnitude field of oil droplets distribution through deposition onto the glass surface (Cylinder D =12.7 mm).

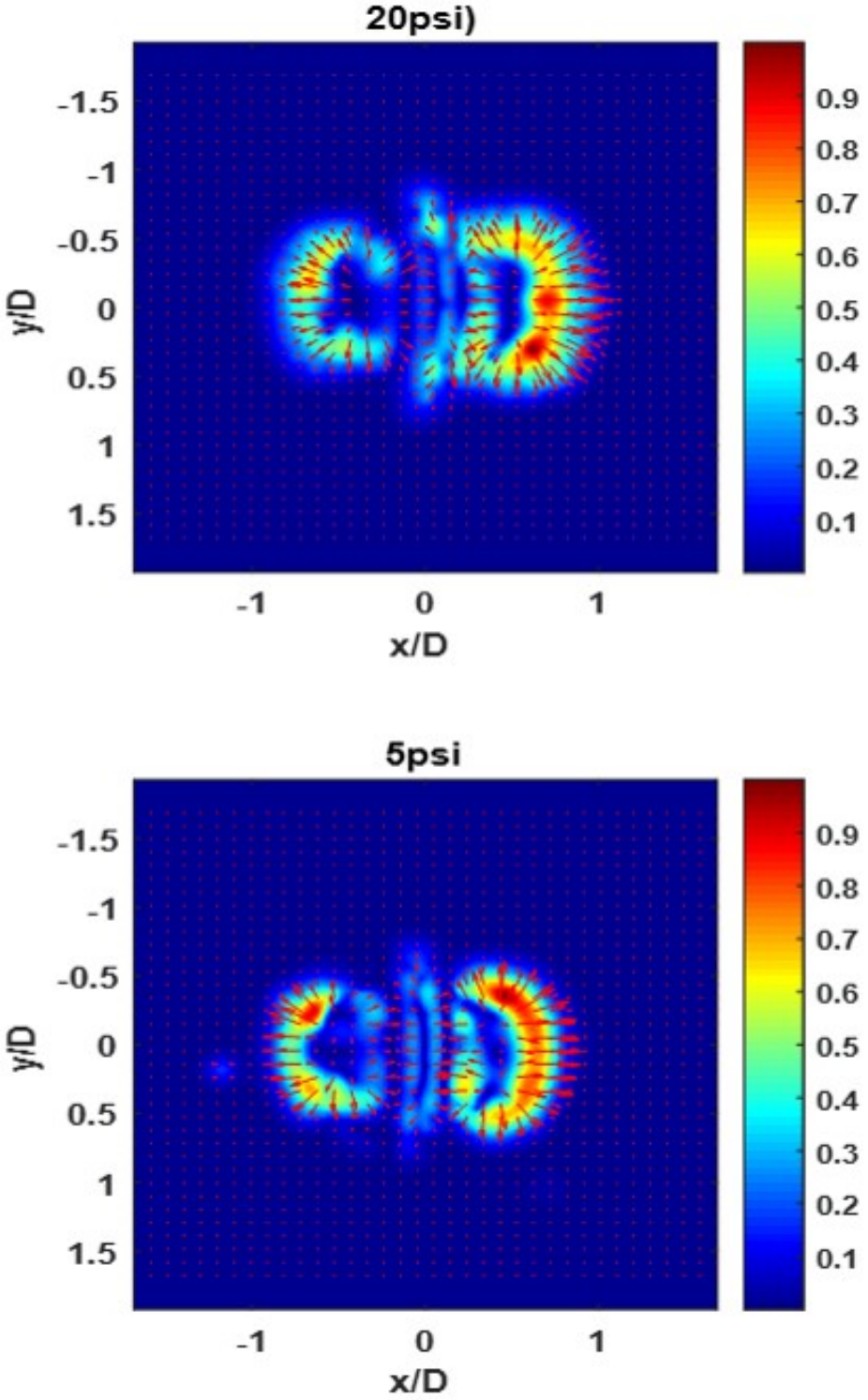

Figure 6.9: Ensemble-averaged velocity magnitude field of oil droplets distribution through deposition onto the glass surface (Cylinder D =10.16 mm).

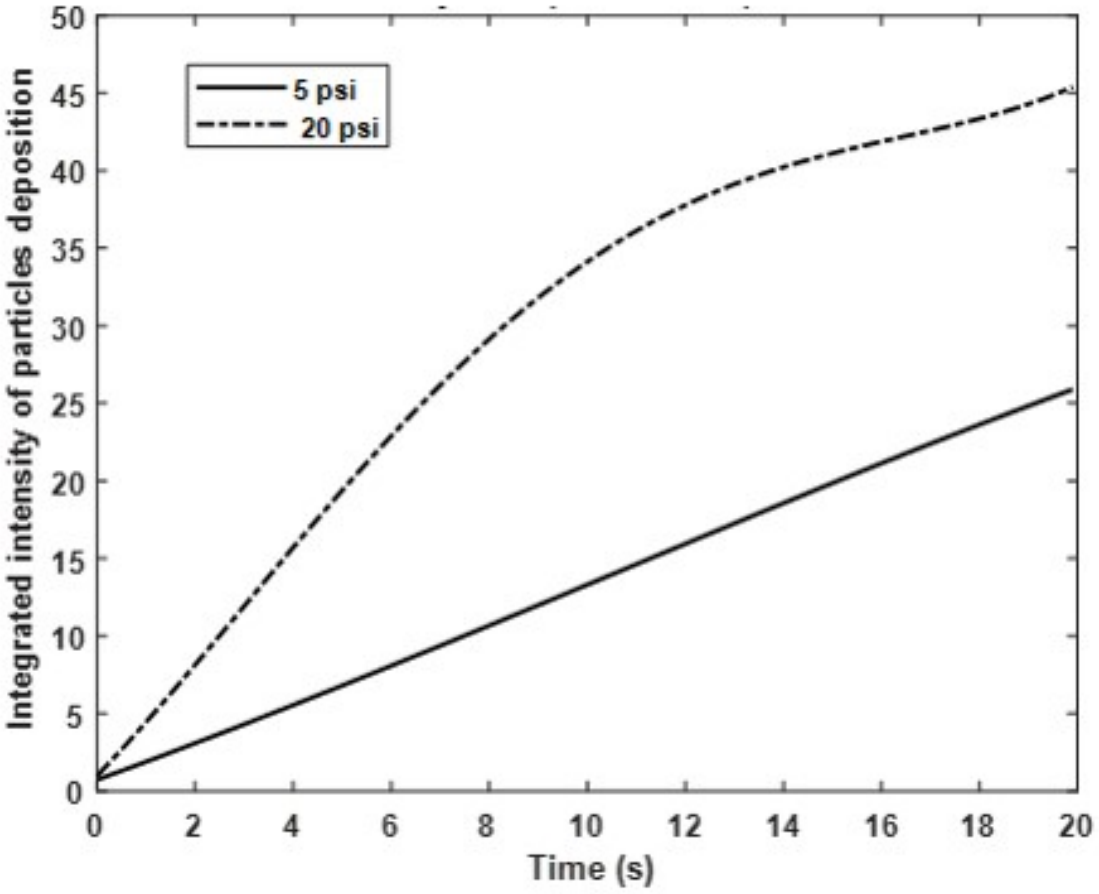

Figure 6.10: Ensemble-averaged velocity magnitude field of oil droplets distribution through deposition onto the glass surface (Cylinder D =12.7 mm).

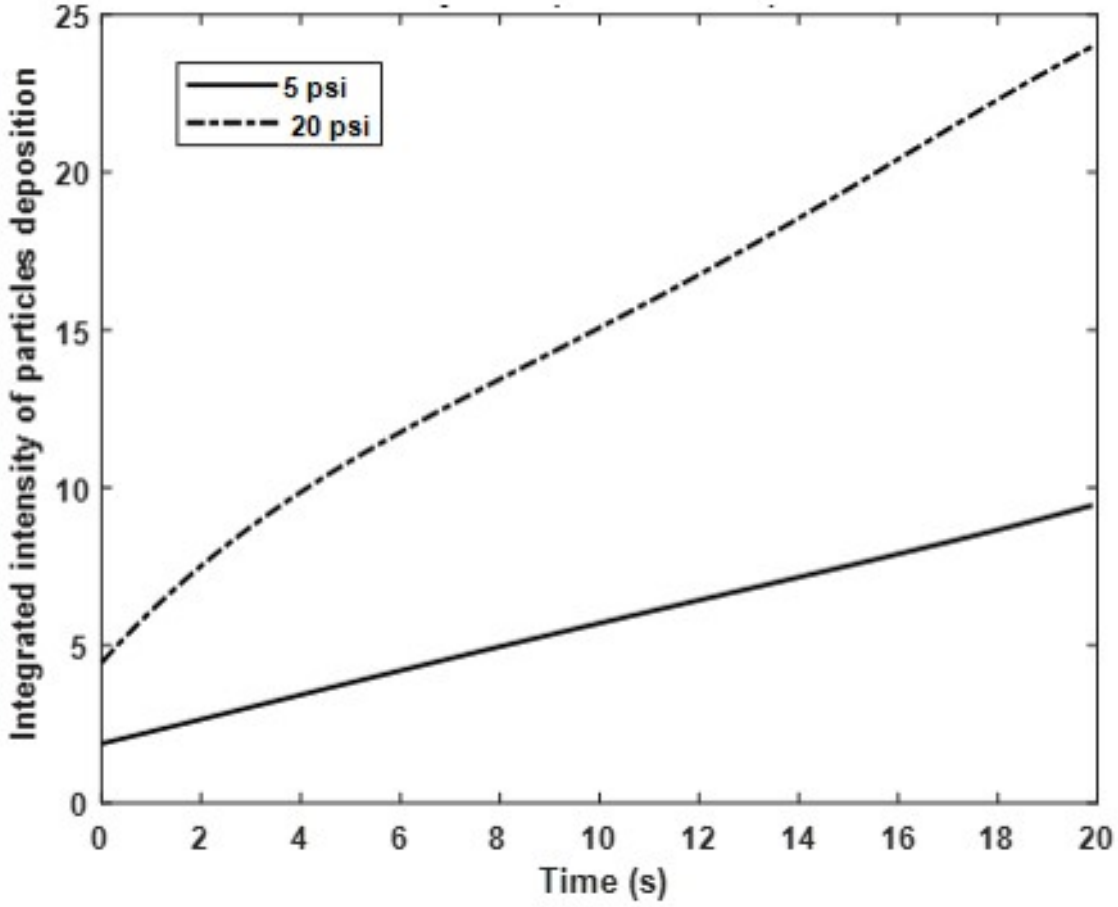

Figure 6.11: Ensemble-averaged velocity magnitude field of oil droplets distribution through deposition onto the glass surface (Cylinder D =10.16 mm).

6.1.3 Configuration 2 of the TIPC Device

The diamond shape is the second configuration of the TIPC device. It has been investigated at the same test conditions for the first configuration. The patterns of deposited droplets that are presented in figure 6.12 were created by using the Diamond shape (TICP) with a width of 12.7 mm at a pressure equal to 5 psi. Figure 6.13 explains the effect of increasing pressure from 5 psi to be 20 psi for the same diamond design. The influence of changing the width of the diamond to be 10.16 mm at the same test conditions of pressure values is shown in figures 6.14 and 6.13. The width plate of 12.7 mm has an irregular shape of particles distribution at both pressures with variation in the amount of deposited luminescent oil particles. Figures 6.16 and 6.17 show the ensemble-averaged of oil distribution velocity for each plate width (12.7 mm and 10.16 mm) at two pressures (5psi and 20 psi).

The change of intensity has been investigated with respect of time based on the pressure values that are applied on each plate width. The intensity of deposited droplets is integrated in order to calculate the averaged intensity difference between 200 images. Figure 6.18 shows the integrated intensity of particles deposition at two different pressures (5 psi and 20 psi) for the plate width of 12.7 mm. Figure 6.19 shows a comparison between 5 psi and 20 psi of pressure by integrated the intensity of deposited droplets over the time of projecting. The high pressure (20 psi) has a significant effect in increasing the amount of luminescent oil due to particles collision.

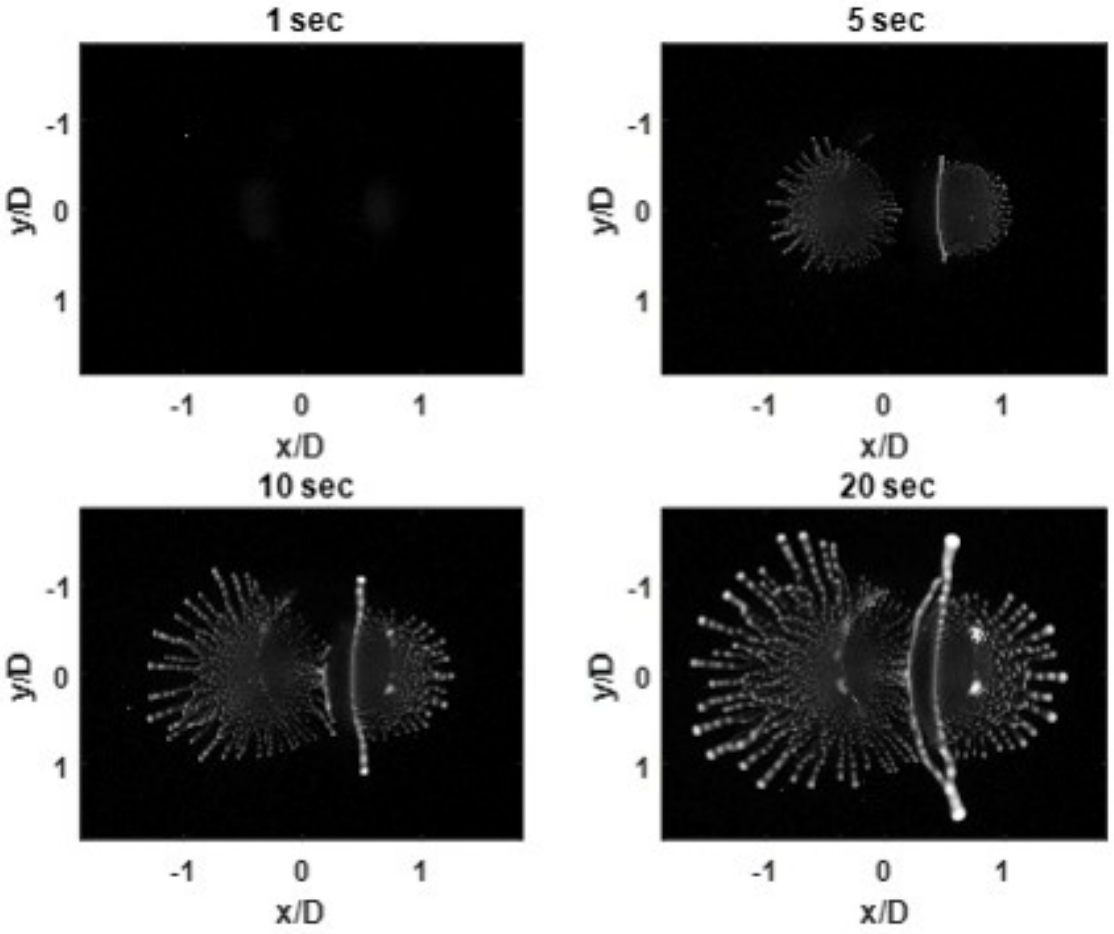

Figure 6.12: luminescent intensity images of particles deposition at different times for Diamond shape (W =12.7 mm, 5 psi).

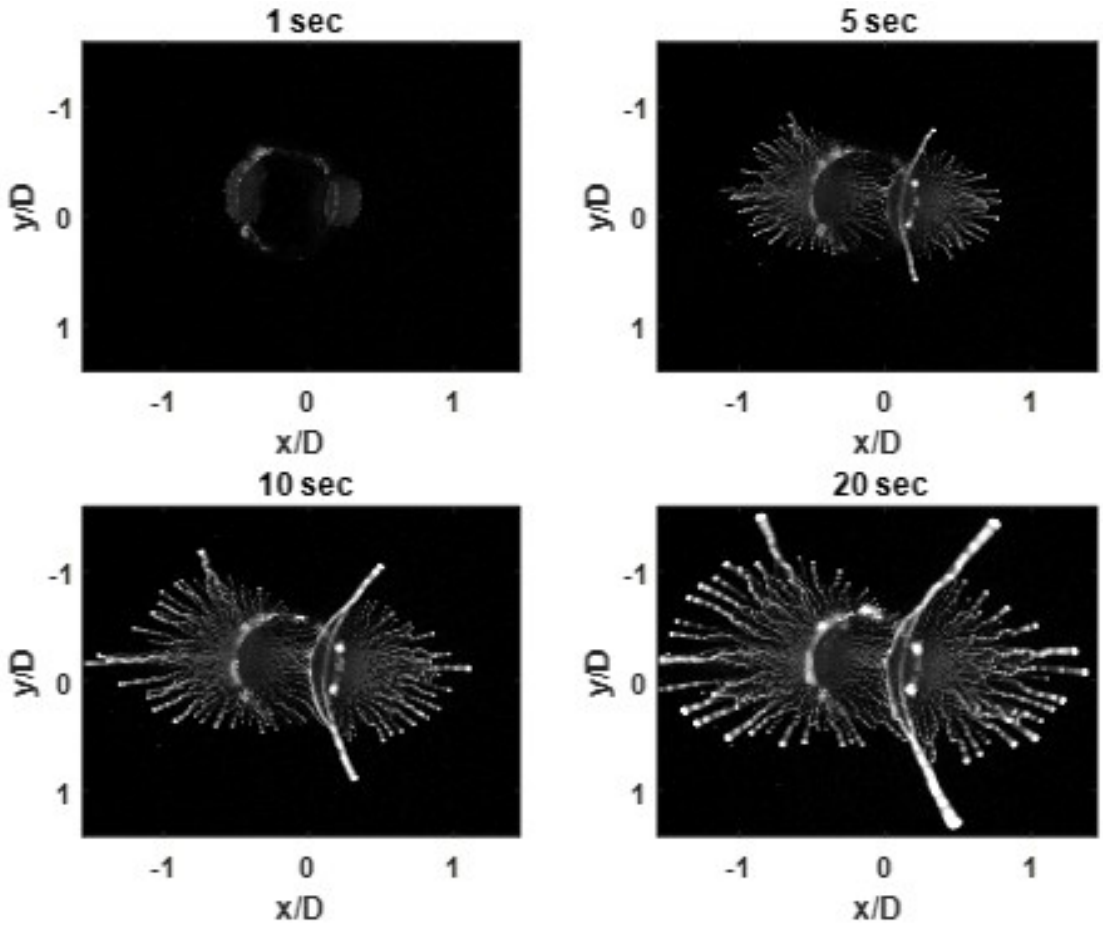

Figure 6.13: luminescent intensity images of particles deposition at different times for Diamond shape (W =12.7 mm, 20 psi).

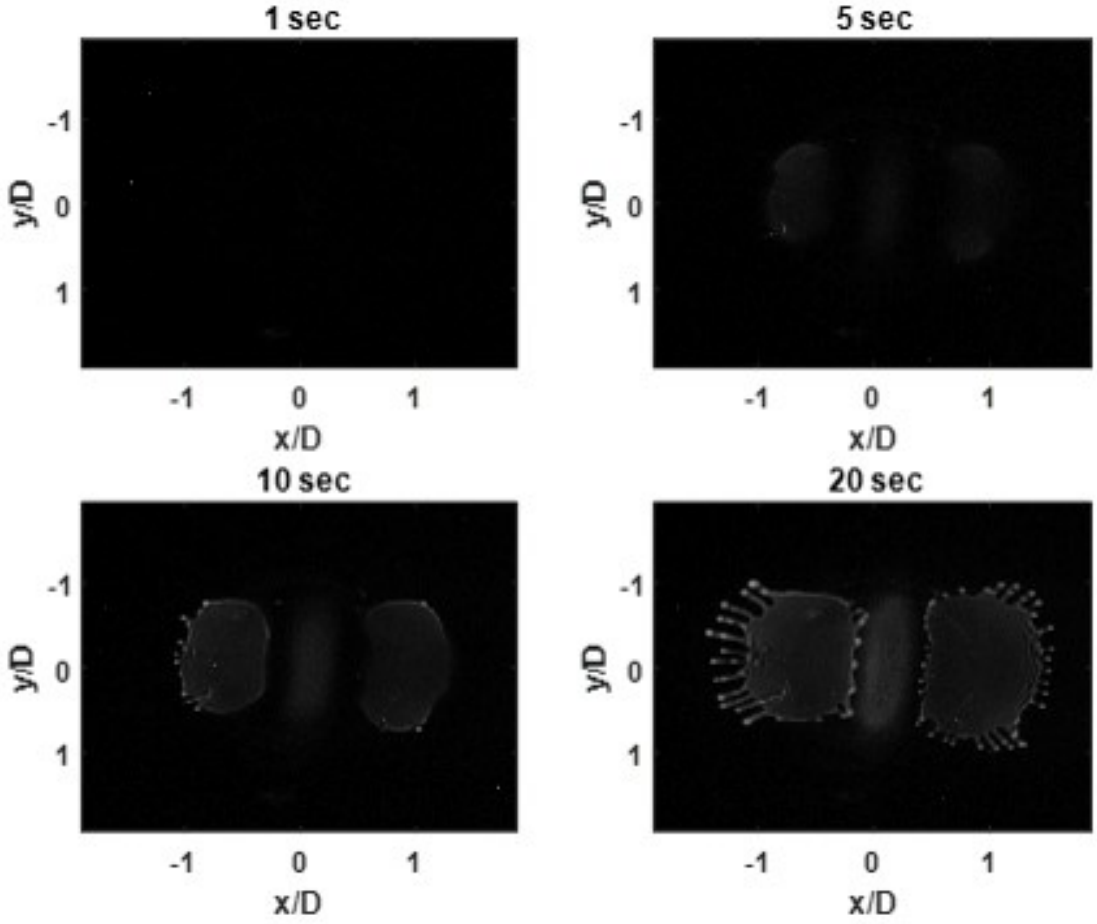

Figure 6.14: luminescent intensity images of particles deposition at different times for Diamond shape (W =10.16 mm, 5 psi).

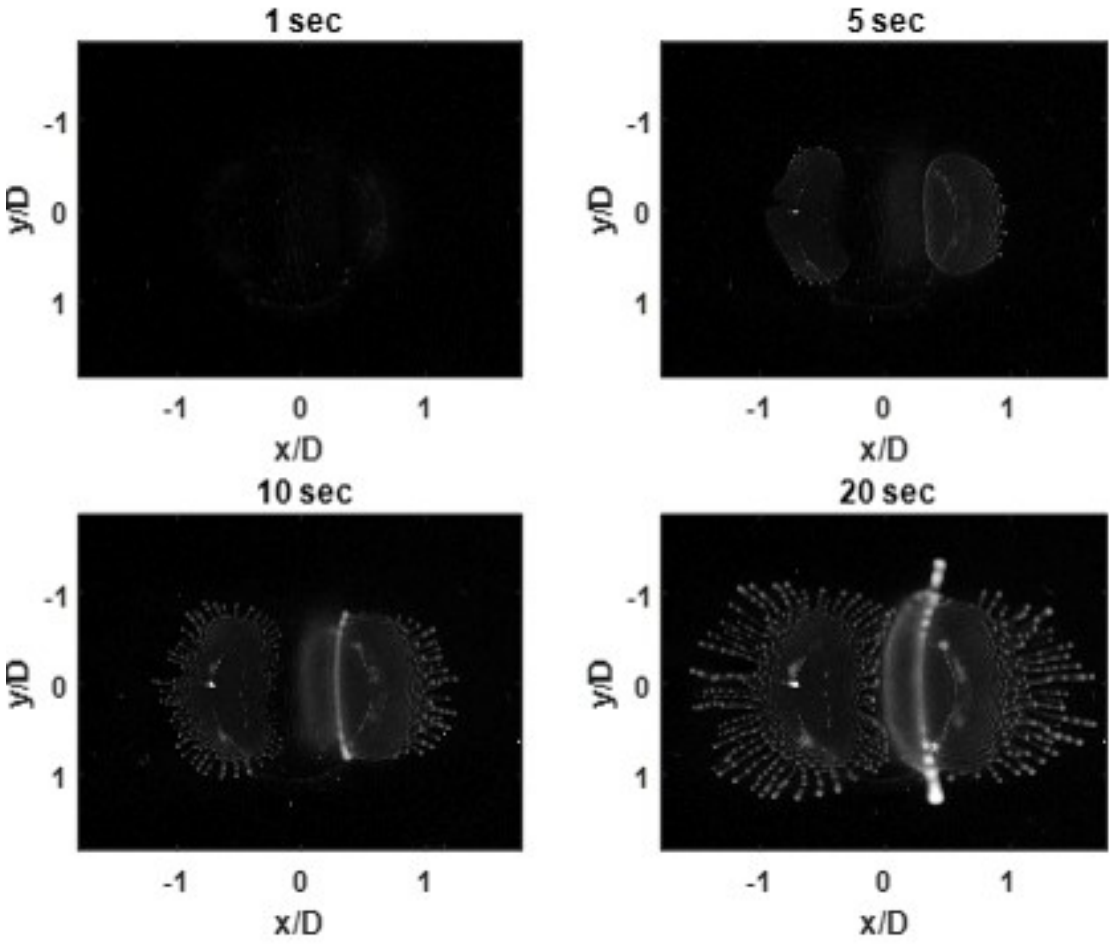

Figure 6.15: luminescent intensity images of particles deposition at different times for Diamond shape (W =10.16 mm, 20 psi).

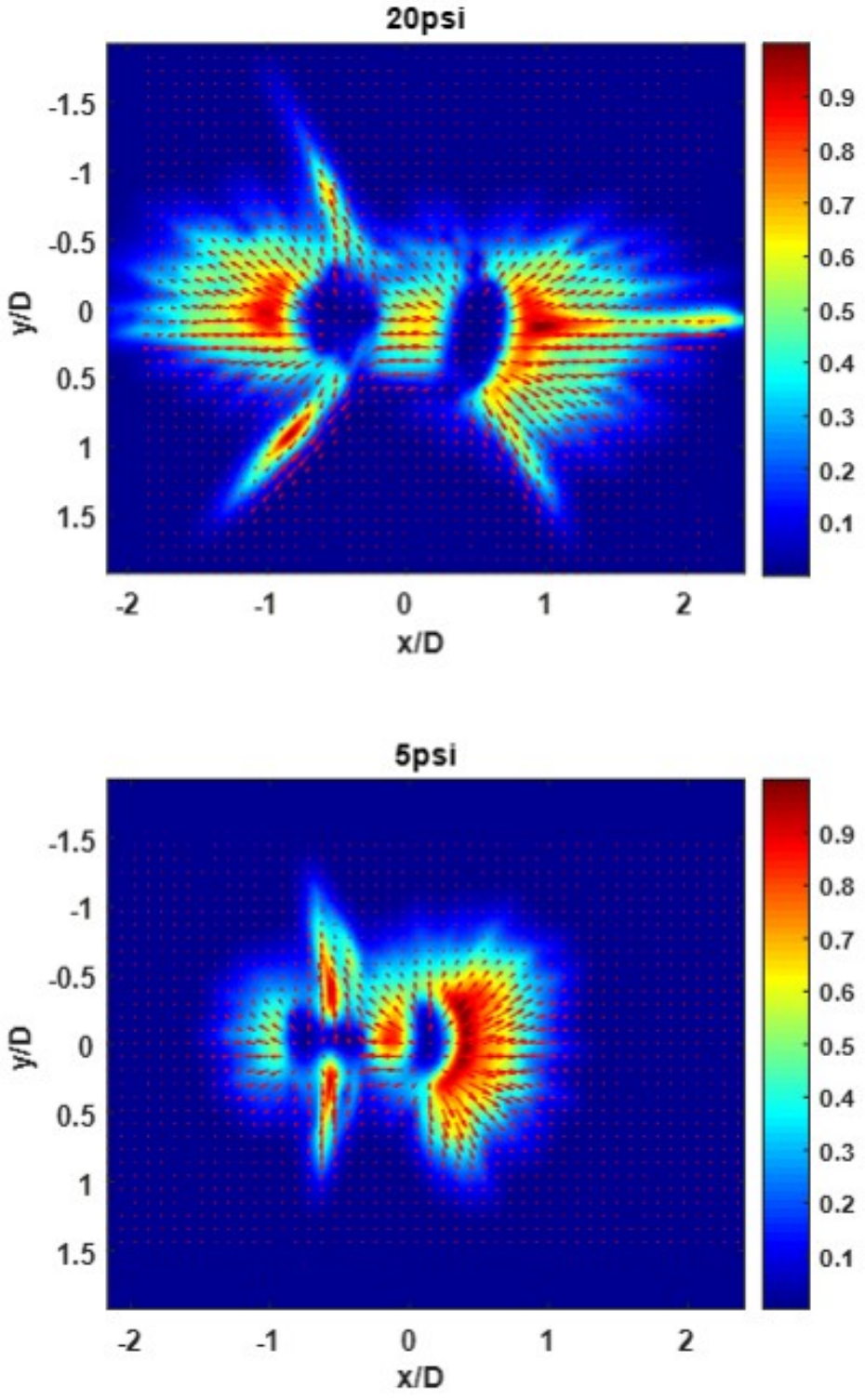

Figure 6.16: Ensemble-averaged velocity magnitude field of oil droplets distribution through deposition onto the glass surface (Diamond W =12.7 mm).

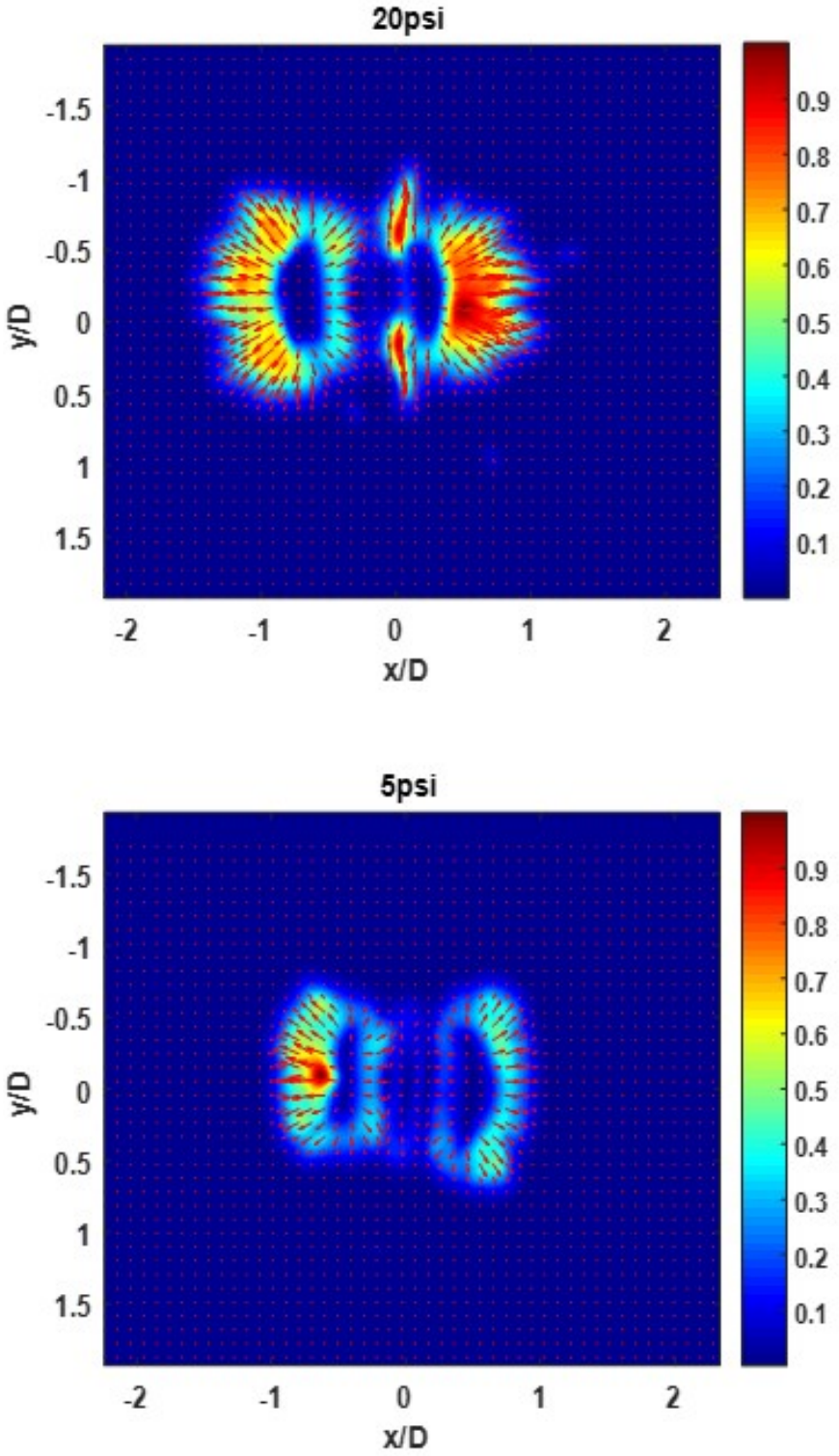

Figure 6.17: Ensemble-averaged velocity magnitude field of oil droplets distribution through deposition onto the glass surface (Diamond W =10.16 mm).

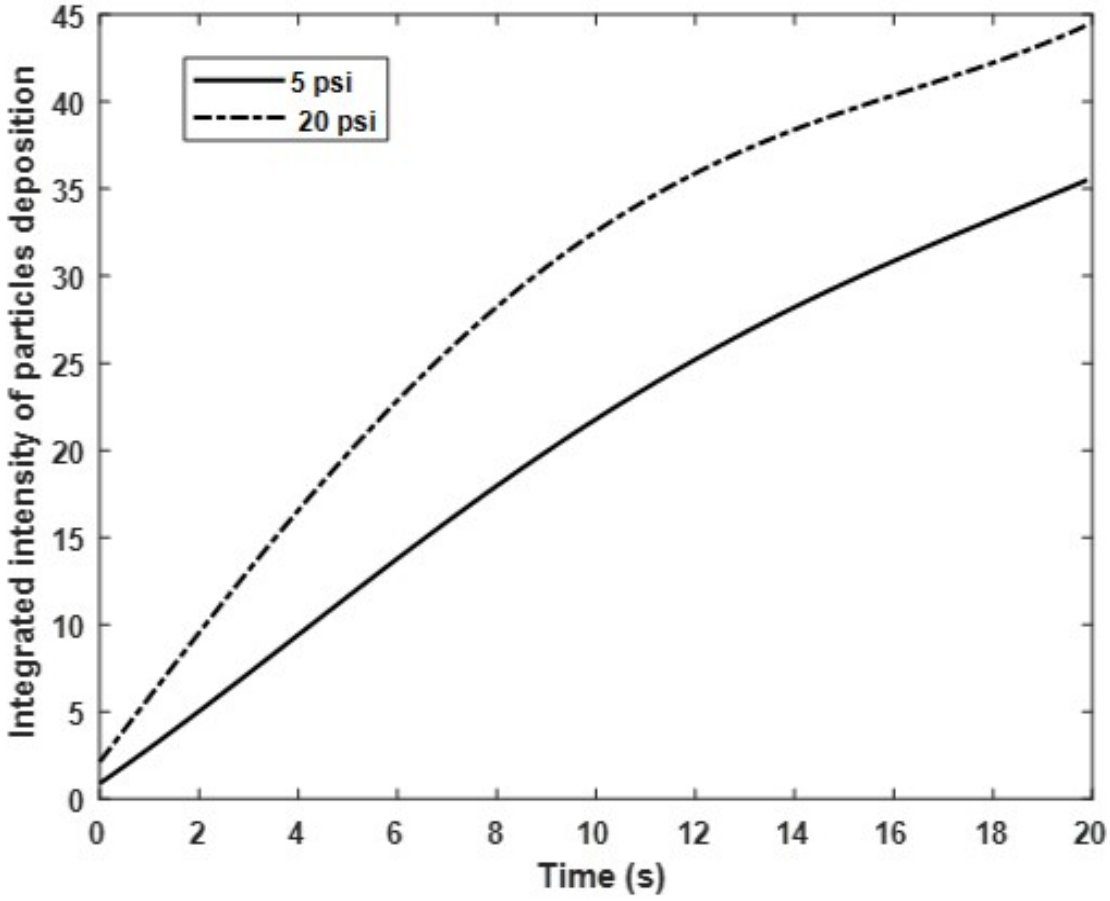

Figure 6.18: Integrated intensity of deposited droplets at two values of inlet pressure (Diamond W =12.7 mm).

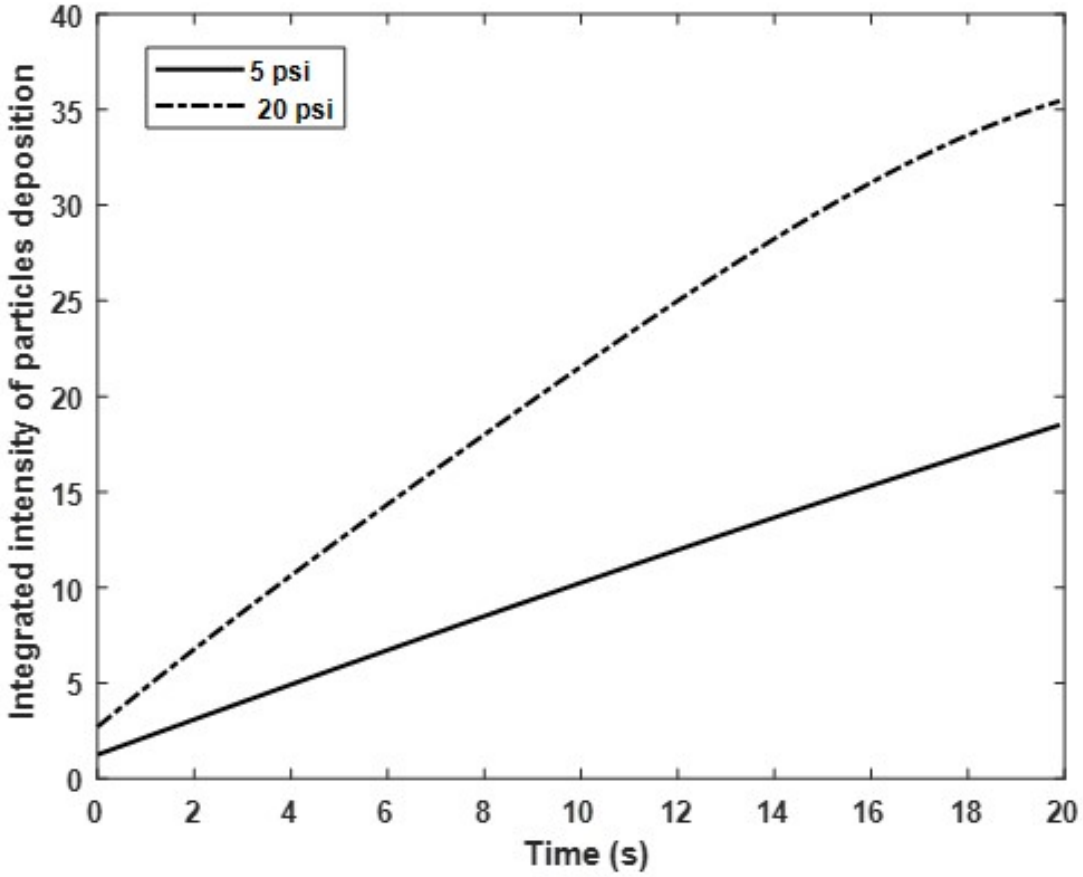

Figure 6.19: Integrated intensity of deposited droplets at two values of inlet pressure (Diamond W =10.16 mm).

6.1.4 Configuration 3 of the TIPC Device

The Oval body is conducted to be the third configuration of the TIPC design. It has been tested at the same pressure conditions, respectively, 5 psi and 20 psi. Figure 6.20 show the luminescent intensity images of deposited particles at different times at 5psi. The effect of increasing pressure to be 20 psi is presented in figure 6.21. The luminescent intensity of particles deposition is formed at the faster time comparing at low pressure (5 psi). Figure 6.22 show the pattern of the ensample-averaged velocity magnitude field of oil droplets distribution for two pressures (20 psi, 5 psi). Figure 6.23 illustrate the amount of deposited droplets at pressure values are 5 psi and 20 psi using the averaged intensity difference between 200 images, is calculated by integrated intensity if deposited particles with respect of time.

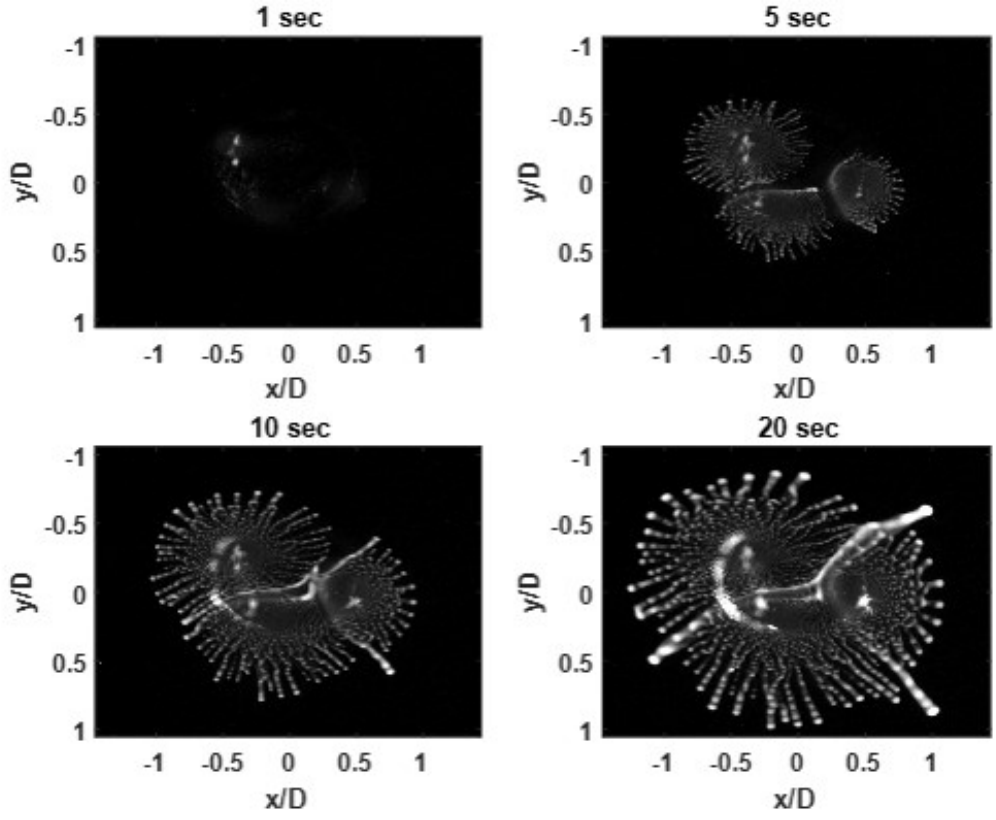

Figure 6.20: luminescent intensity images of particles deposition at different times for Oval Curve shape (W =10.16 mm and L=25.4 mm, 5 psi).

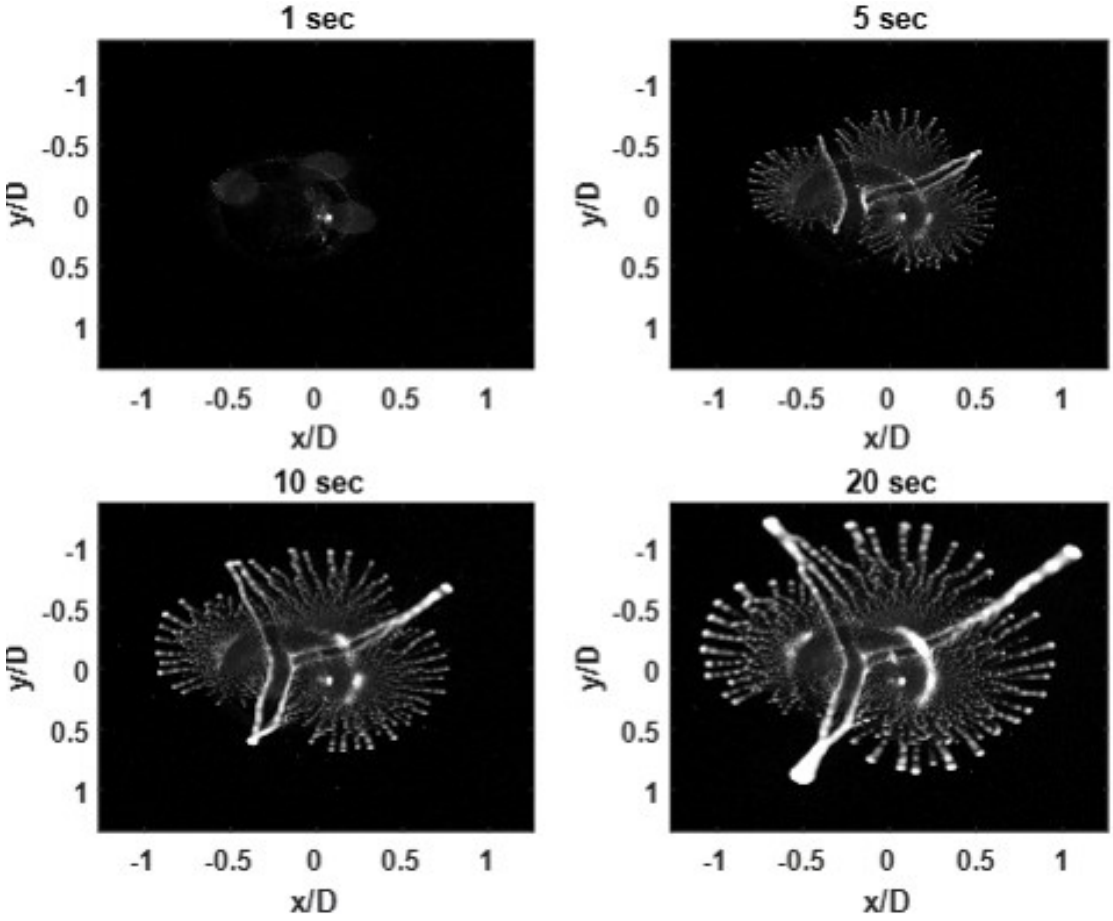

Figure 6.21: luminescent intensity images of particles deposition at different times for Oval body shape (D =12.7 mm and L =25.4 mm, 20 psi).

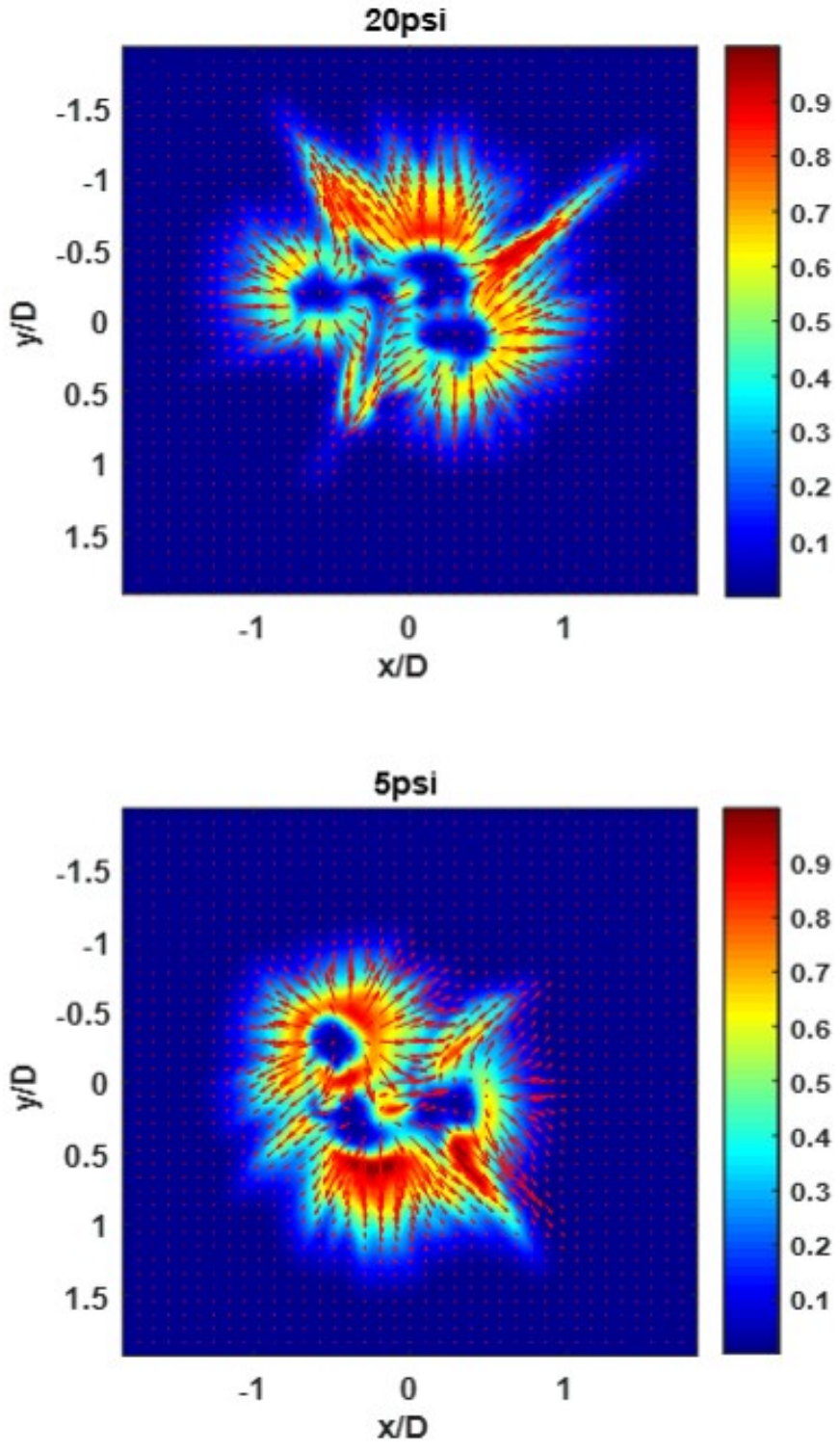

Figure 6.22: Ensemble-averaged velocity magnitude field of oil droplets distribution through deposition onto the glass surface (Oval body).

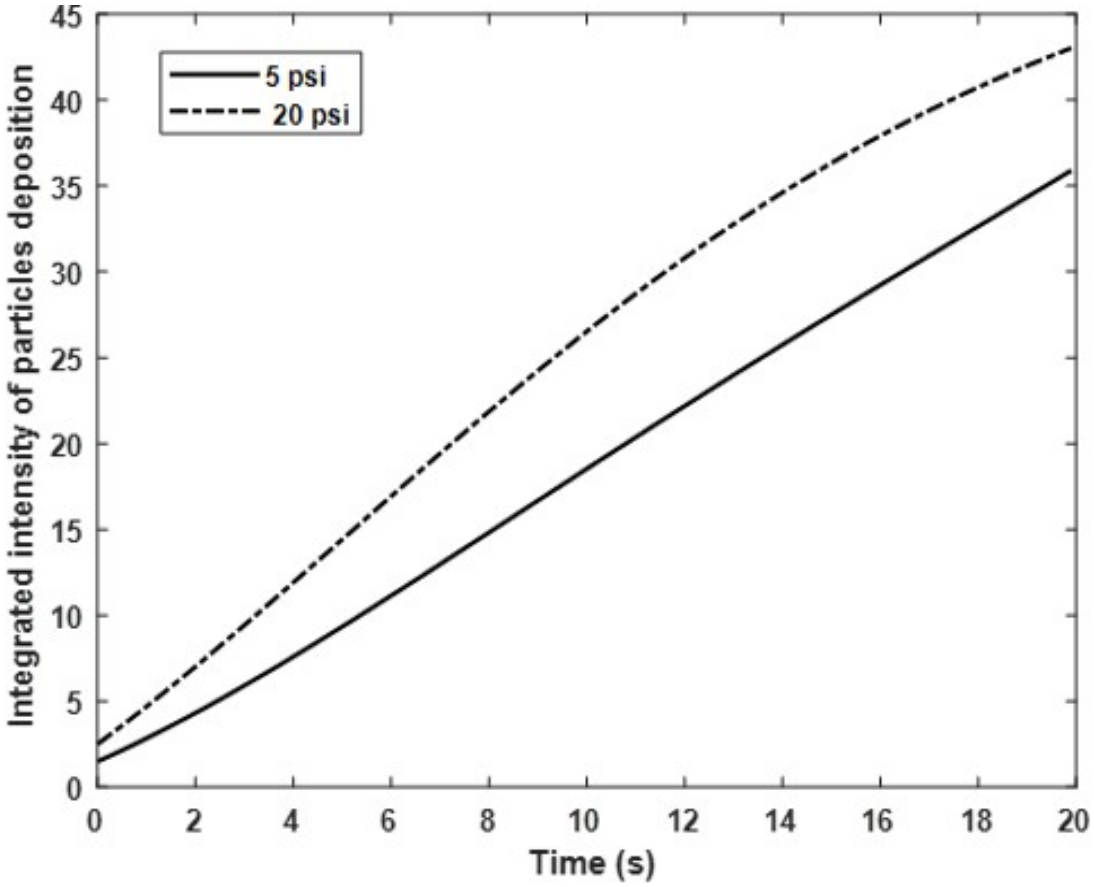

Figure 6.23: Integrated intensity of deposited droplets at two values of inlet pressure (Oval body).

6.1.5 Configuration 4 of the TIPC Device

The fourth configuration of the TIPC device is a cylindrical rod has a diameter of 12.7 mm and a length of 25.4 mm. It is designed to investigate the effect of increasing the surface area for the TIPC device. Figure 6.24 show the luminescent intensity images of particles deposition at different times at inlet pressure is equal to 5 psi and 12.22 m/s. The formation of liquid droplets deposited on a glass wall is weak compared with previous designs at the same test conditions. Also, it can be seen that in figure 6.25 with increasing the pressure to be 20 psi and 27.3 m/s. For both cases of pressure, the ensemble-averaged velocity magnitude field of oil droplets distribution as is shown in figure 6.26. The intensity of deposited particles is integrated with respect to time in order to determine the averaged intensity difference between 200 images at both pressures. The result of the integrated intensity of deposited particles is shown in figure 6.27.

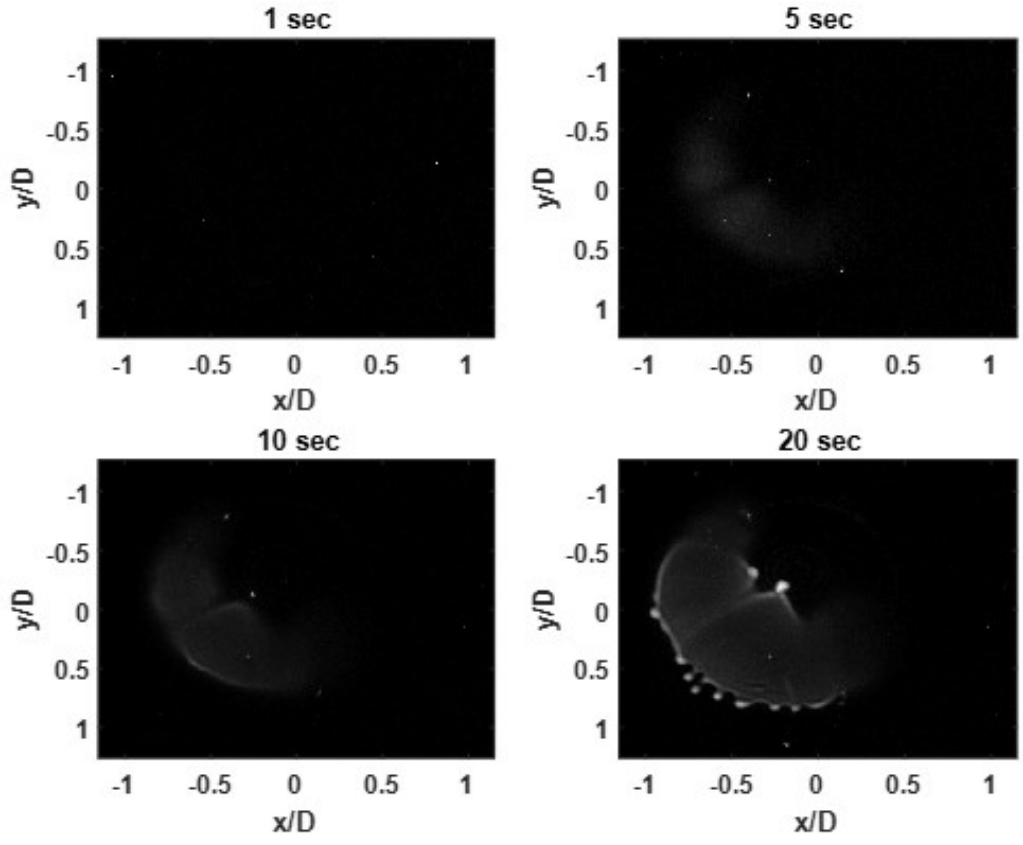

Figure 6.24: luminescent intensity images of particles deposition at different times for Cylindrical rod shape (D =12.7 mm, 5 psi).

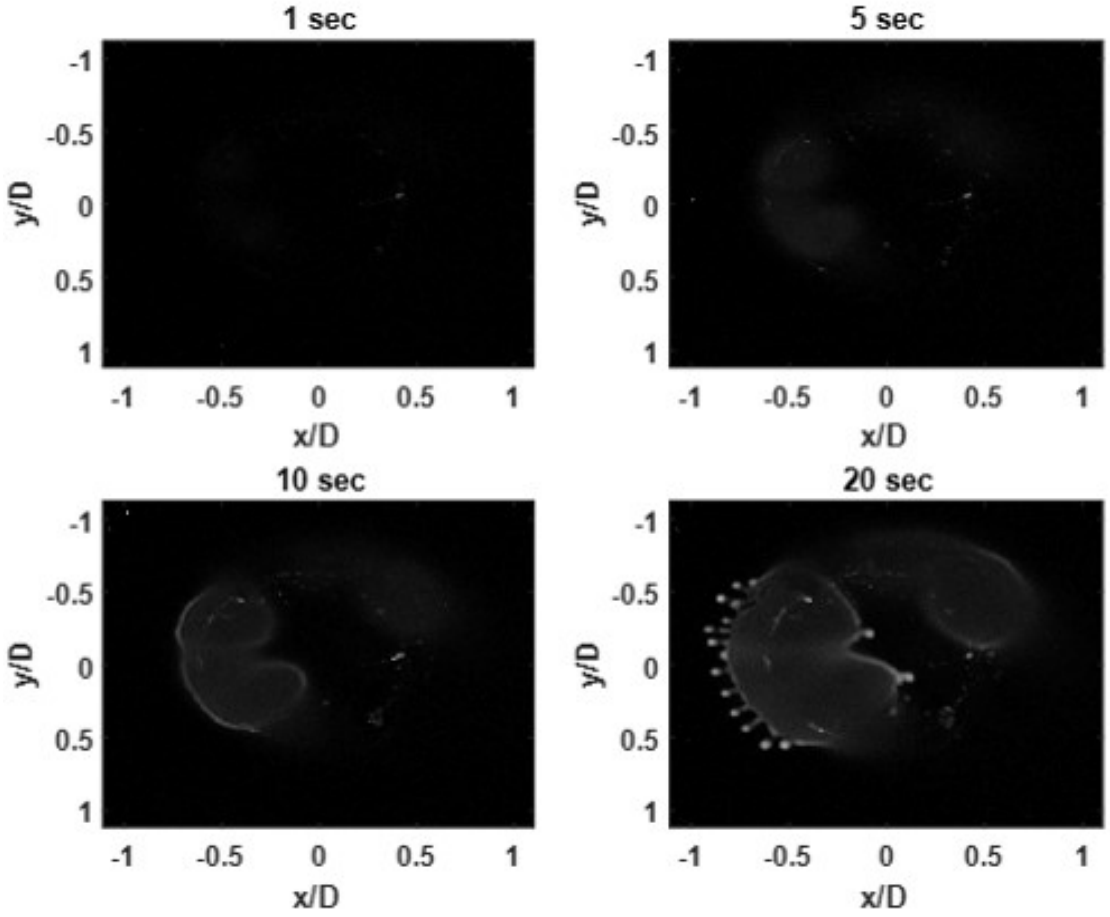

Figure 6.25: luminescent intensity images of particles deposition at different times for Cylindrical rod shape (D =12.7 mm, 20 psi).

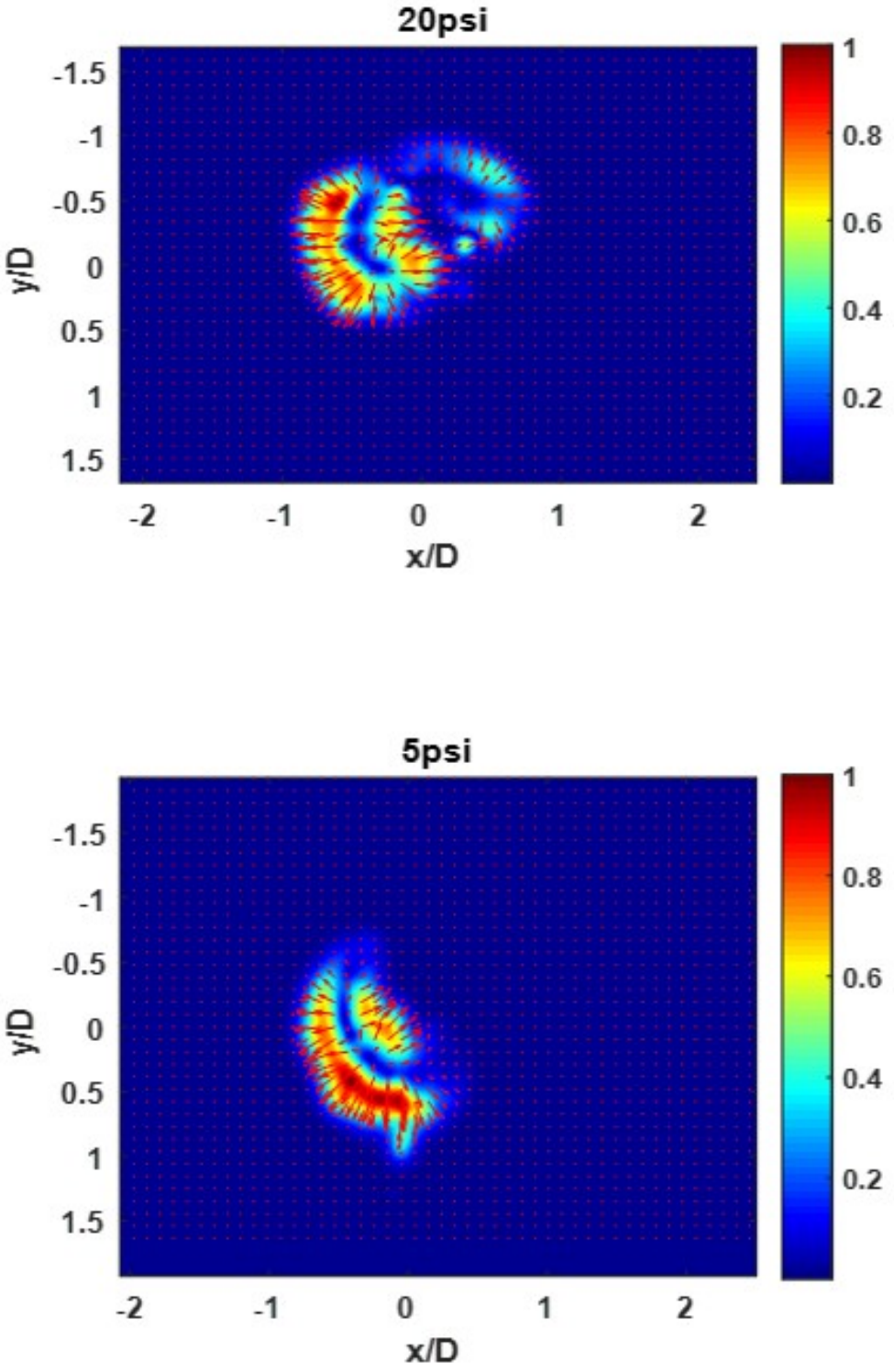

Figure 6.26: Ensemble-averaged velocity magnitude field of oil droplets distribution through deposition onto the glass surface at different values of pressure (Cylindrical rod).

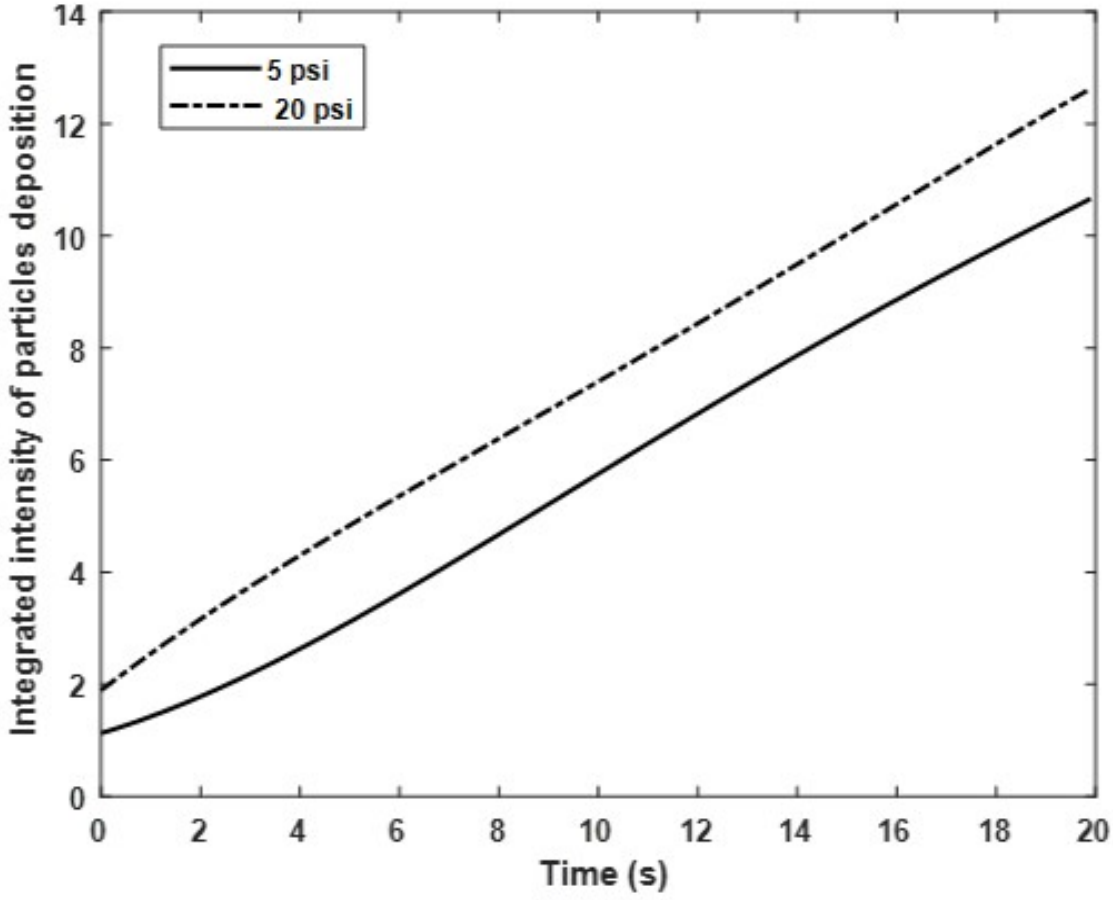

Figure 6.27: Integrated intensity of deposited droplets at two values of inlet pressure (Cylindrical rod).

6.2 Visualization of Droplets Deposition in the Pipe

To explore the physical mechanism of the TIPC device inside the pipe in terms of the formation of the deposited droplets, experiment was conducted. The experimental setup is presented in figure 6.28. The atomizer is used to generate the particles which are mixed with luminescent dye. The camera is mounted to be perpendicular to the flow direction in order to detect the luminescent oil droplets that are excited by using UV lights. Different values of pressure were applied through the experiment respectively, 10 psi, 20 psi and 40 psi. Three different design of the TIPC devise have been used to visualize the oil liquid deposited inside the pipe.

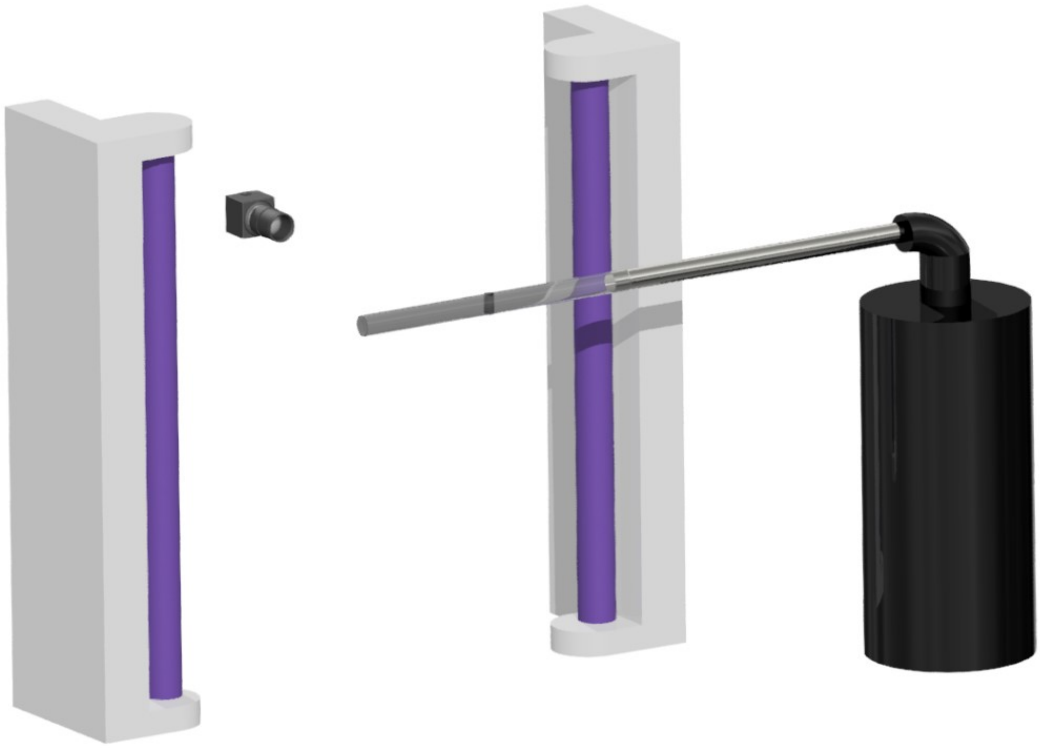

Figure 6.28: Diagram of the experimental setup for visualization inside the pipe.

6.2.1 Cylinder Shape of the TIPC Device

The visualization of deposited oil droplets, due to the cylinder design with a diameter of 12.7 mm, has been done at various values of pressure. First visualization is implemented at 10 psi with flow velocity is equal to 17.98 m/s. Figure 6.29 shows the luminescent intensity images of

droplets deposition inside the pipe at different times and test conditions of the first visualization. The pressure inlet is changed to be 20 psi for the second visualization. It is shown in Figure 6.30. The measured velocity in this case is equal to 27.3 m/s. Figure 6.31 shows the visualization images of the third case at inlet pressure equal to 40 psi and 41.4 m/s of velocity flow. The deposited droplets inside the pipe are formed such as a triangle shape with time for all cases through visualization. The forming speed of deposited particles is based on the pressure value, where the time period of formation is reduced by increasing the pressure. The velocity magnitude field of oil droplets deposition is calculated for all visualized images using optical flow. Figure 6.32 shows the ensemble-averaged velocity magnitude field of oil droplets at each pressure respectively, 10 psi, 20psi and 40 psi. The change of intensity is calculated by integrated the averaged intensity for 200 images for each case. The results of integrated intensity are normalized by the maximum value of intensity at high pressure (40 psi). Figure 6.33 shows the integrated intensity normalized of deposited droplets at different pressures.

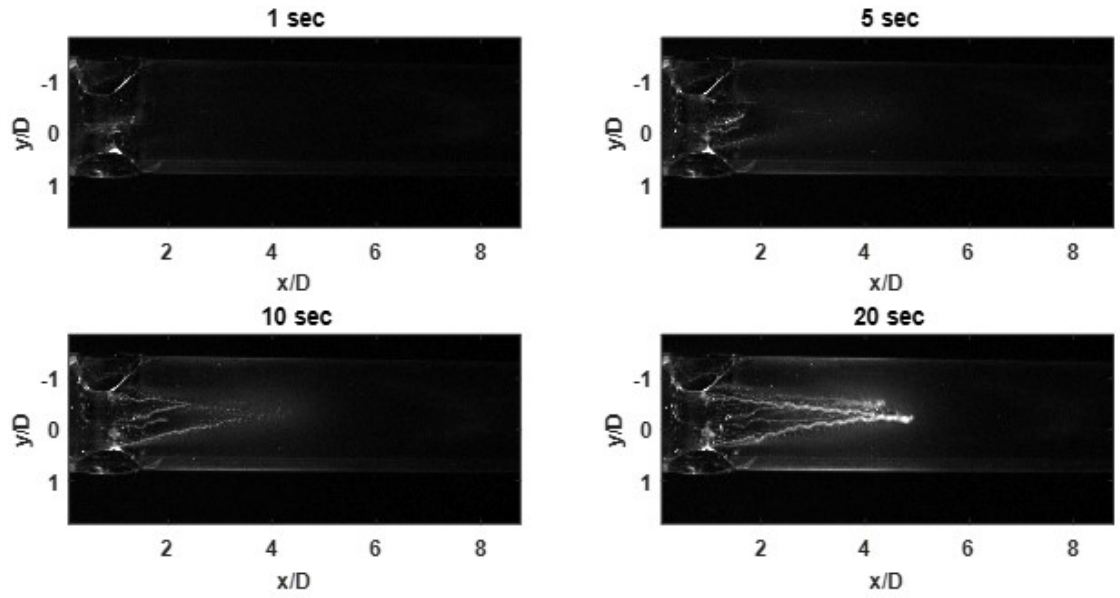

Figure 6.29: Visualization luminescent intensity images of deposited droplets at different times at 10 psi (Cylinder D =12.7 mm).

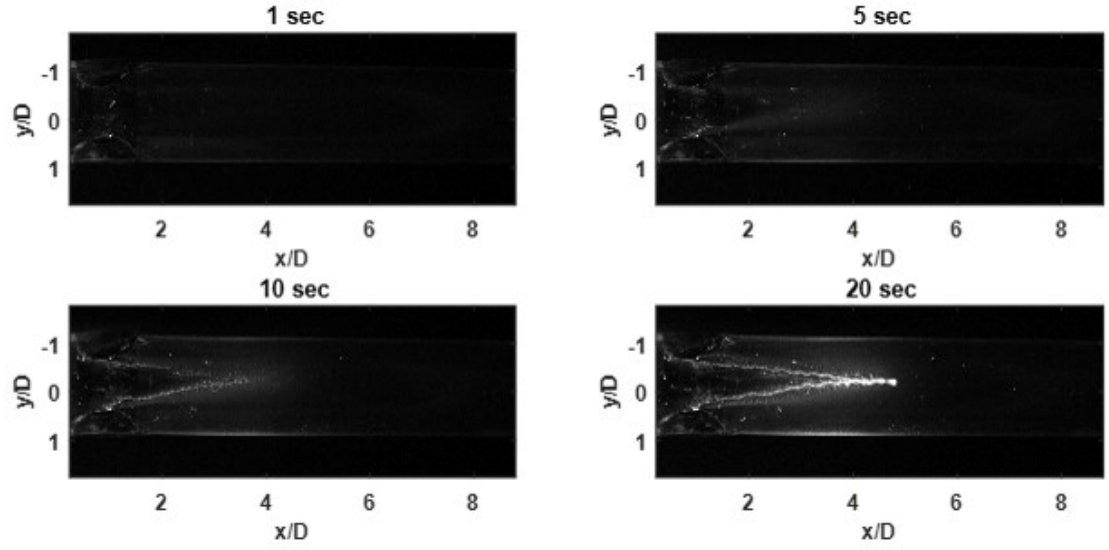

Figure 6.30: Visualization luminescent intensity images of deposited droplets at different times at 20 psi (Cylinder D =12.7 mm).

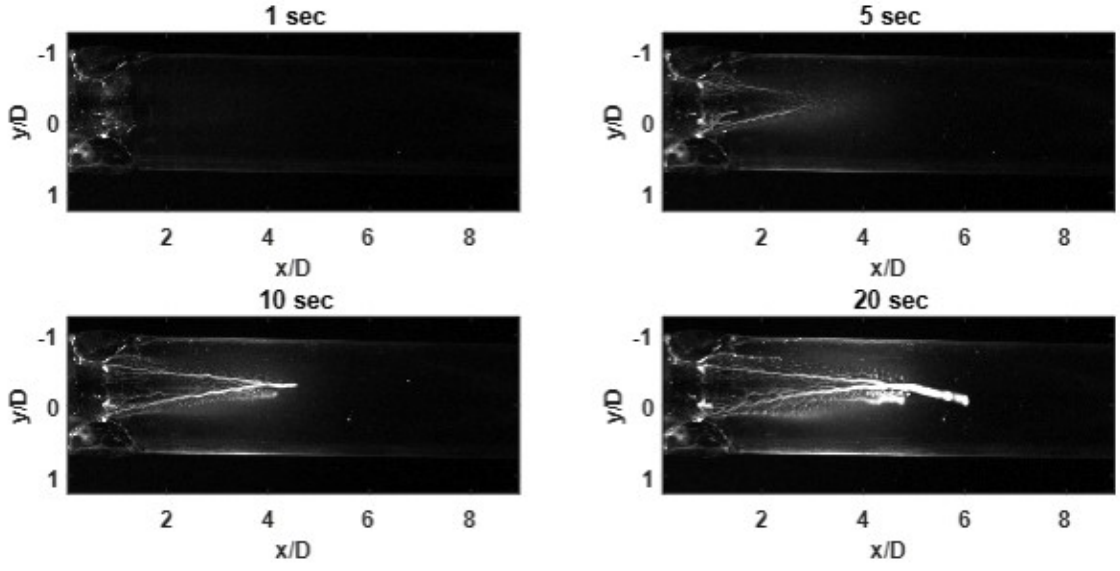

Figure 6.31: Visualization luminescent intensity images of deposited droplets at different times at 40 psi (Cylinder D =12.7 mm).

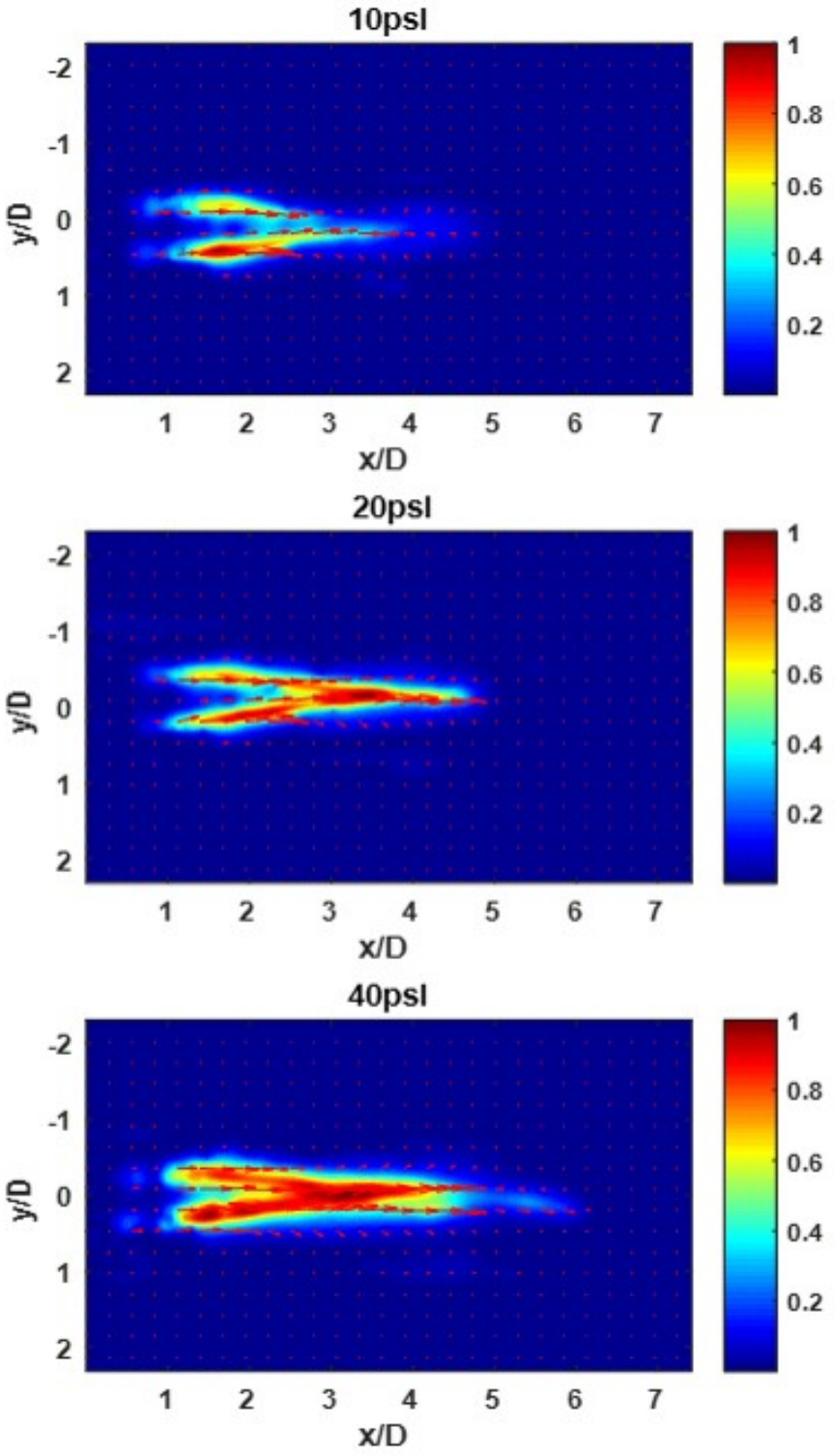

Figure 6.32: The ensemble-averaged velocity magnitude field of oil droplets deposition at different pressures (Cylinder D =12.7 mm).

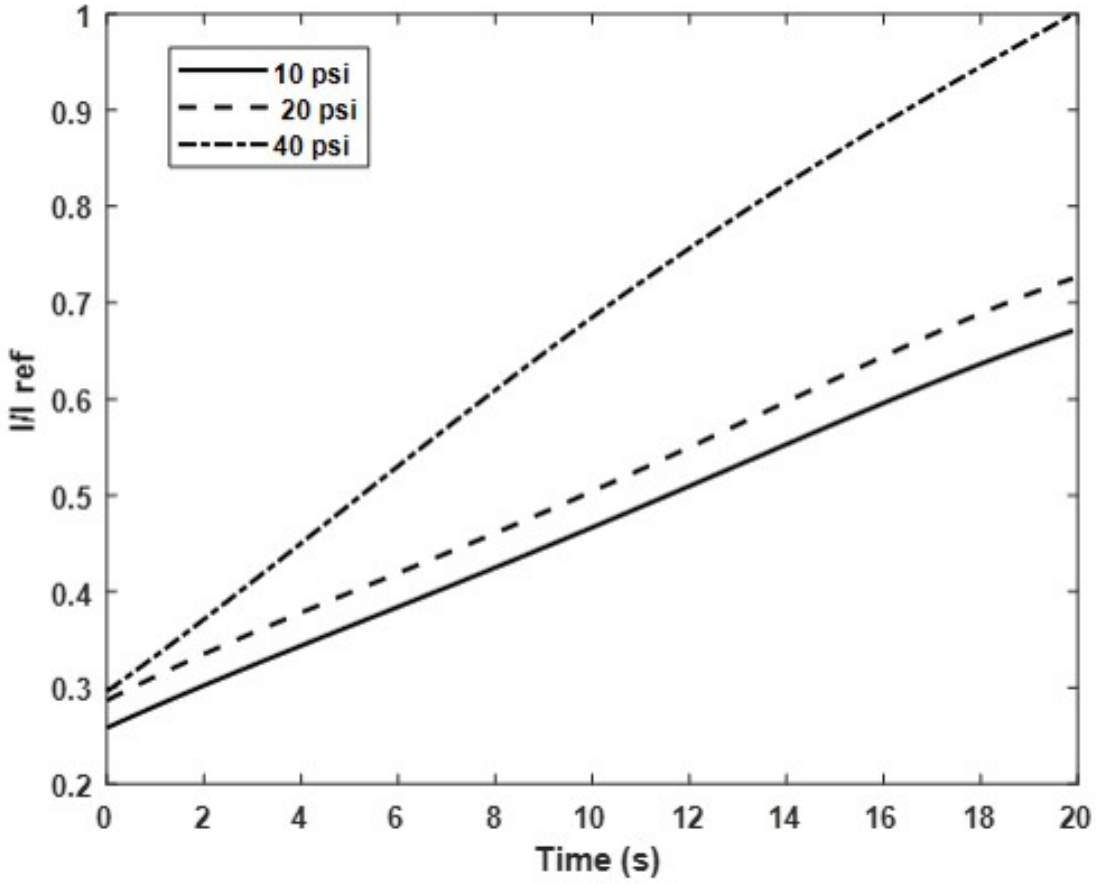

Figure 6.33: Normalized of the integrated intensity of deposited droplets at different pressures (Cylinder D =12.7 mm).

6.2.2 Diamond Dhape of the TIPC Device

The plate shape with a width of 12.7 mm has been used to clarify how the TIPC device works using visualization. It has been affected by three different values of pressures respectively, 10 psi, 20 psi and 40 psi. The visualization of the first effect is shown in figure 6.34 at different times and at certain conditions of pressure and flow velocity (10 psi and 17.98 m/s). The second effect is visualized at 20 psi and 27.3 m/s of flow velocity. It is presented at different times in figure6.35. Figure 6.36 shows the visualization of the third effect where the pressure is equal to 40 psi and flow velocity is equal to 41.4 m/s. The ensemble-averaged velocity magnitude field of oil droplets deposition inside the pipe at different pressures is shown in figure 6.37. The averaged intensity difference between 200 images is calculated for each pressure. Figure 6.38 shows the normalization of the integrated intensity of deposited particles at different pressures, 10 psi, 20 psi and 40 psi.

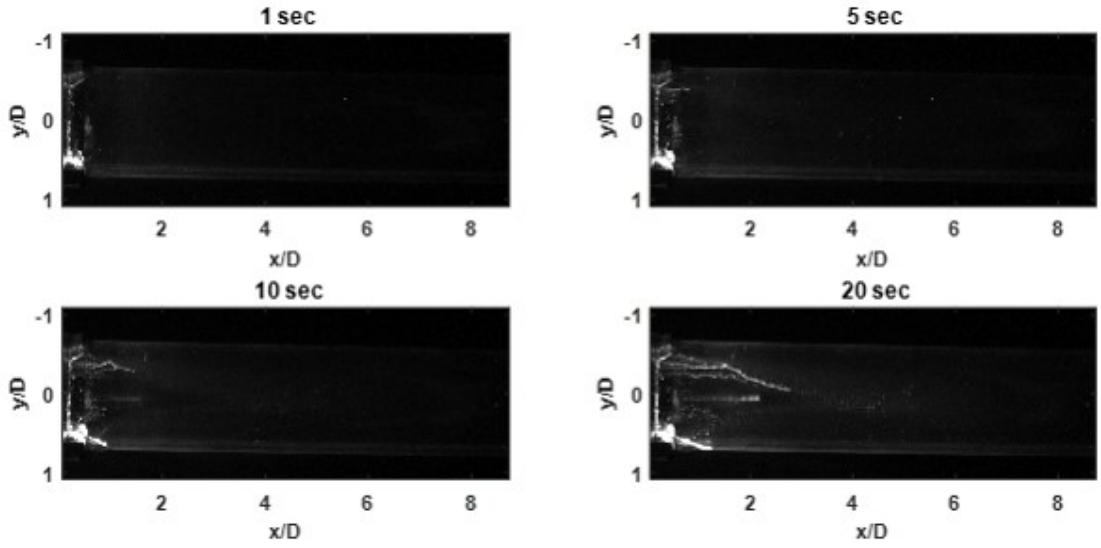

Figure 6.34: Visualization luminescent intensity images of deposited droplets at different times at 10 psi (Diamond W =12.7 mm).

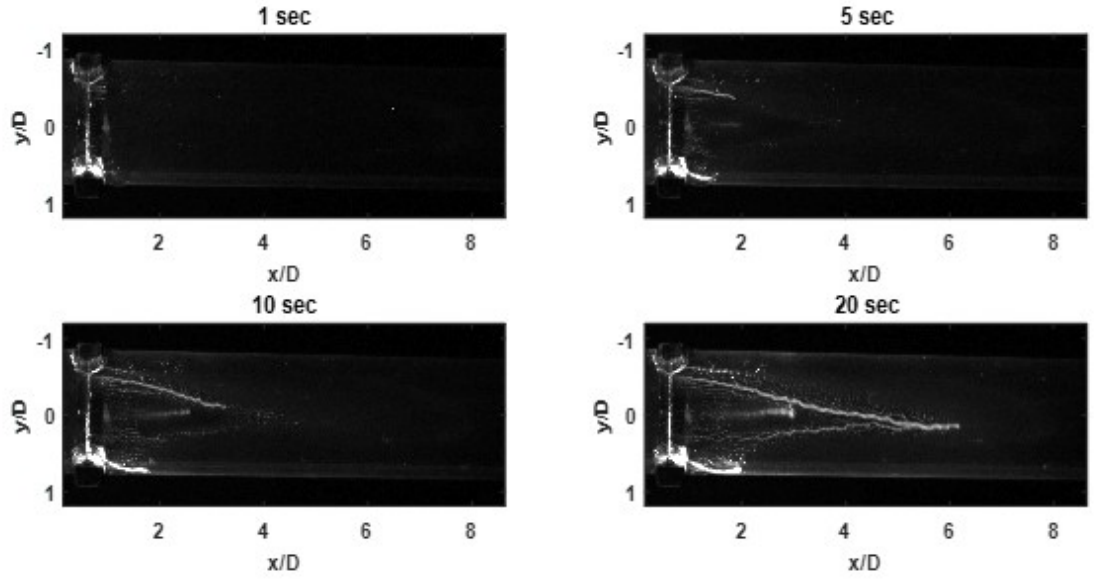

Figure 6.35: Visualization luminescent intensity images of deposited droplets at different times at 20 psi (Diamond W =12.7 mm).

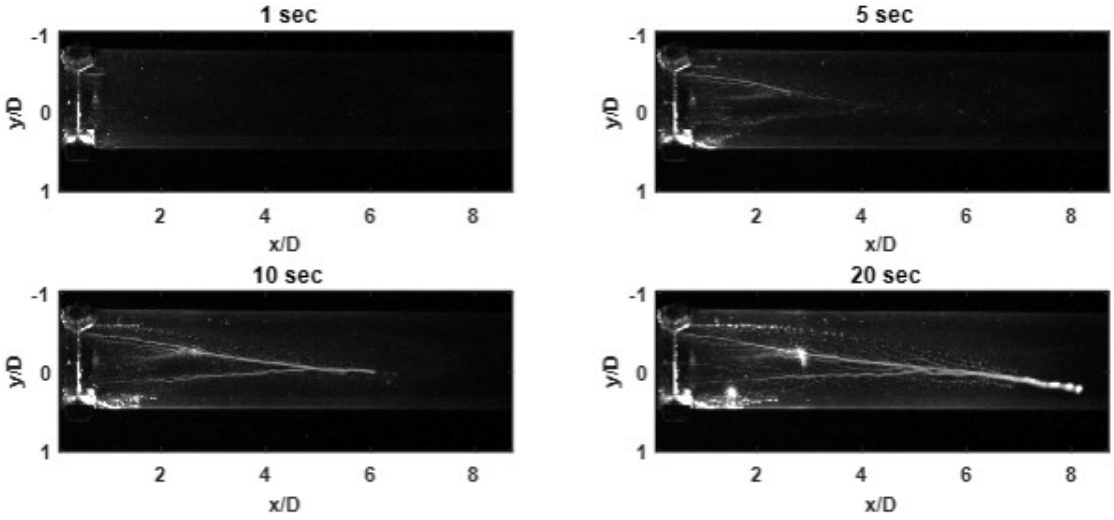

Figure 6.36: Visualization luminescent intensity images of deposited droplets at different times at 40 psi (Diamond W =12.7 mm).

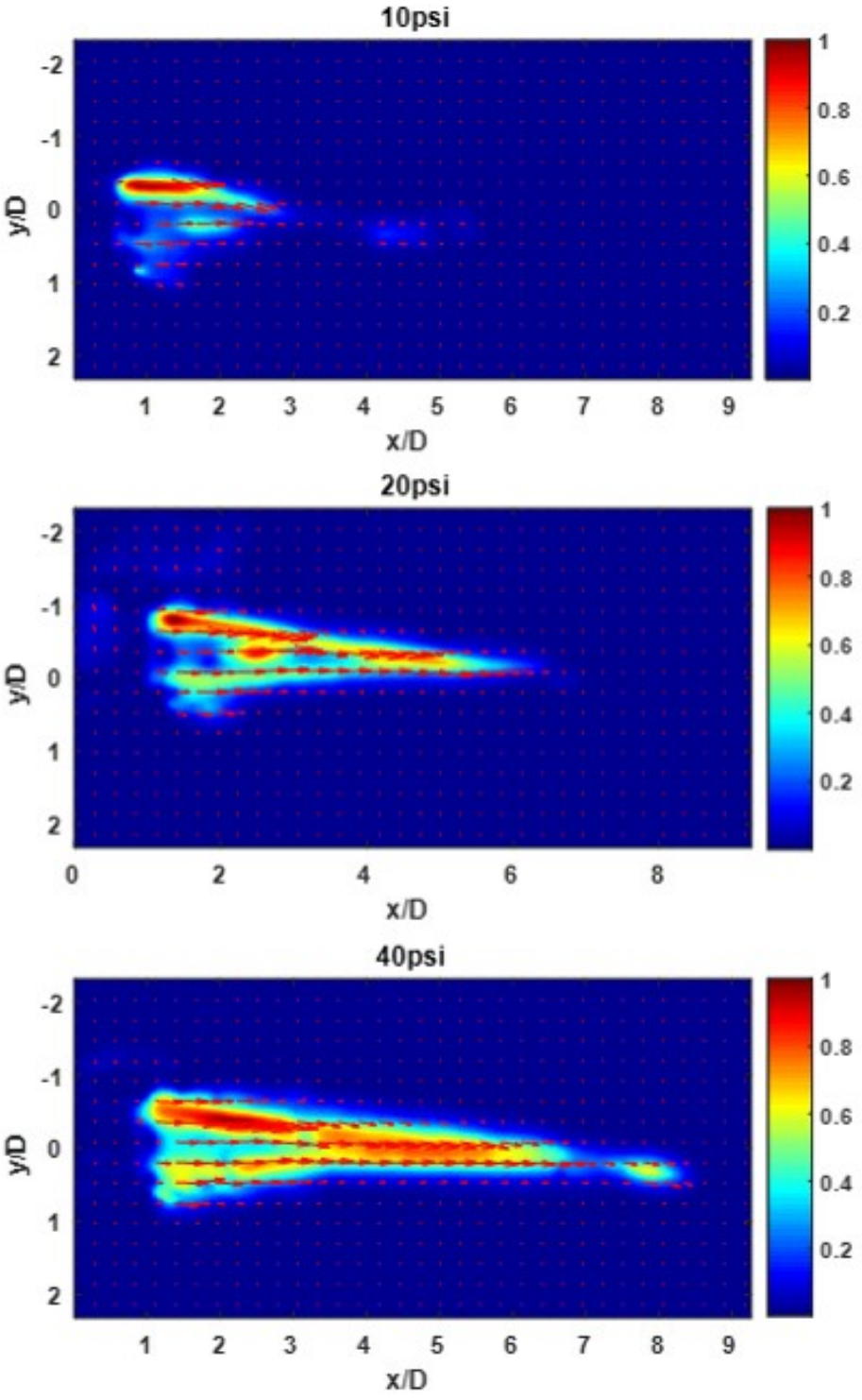

Figure 6.37: The ensemble-averaged velocity magnitude field of oil droplets deposition at different pressures (Diamond W =12.7 mm).

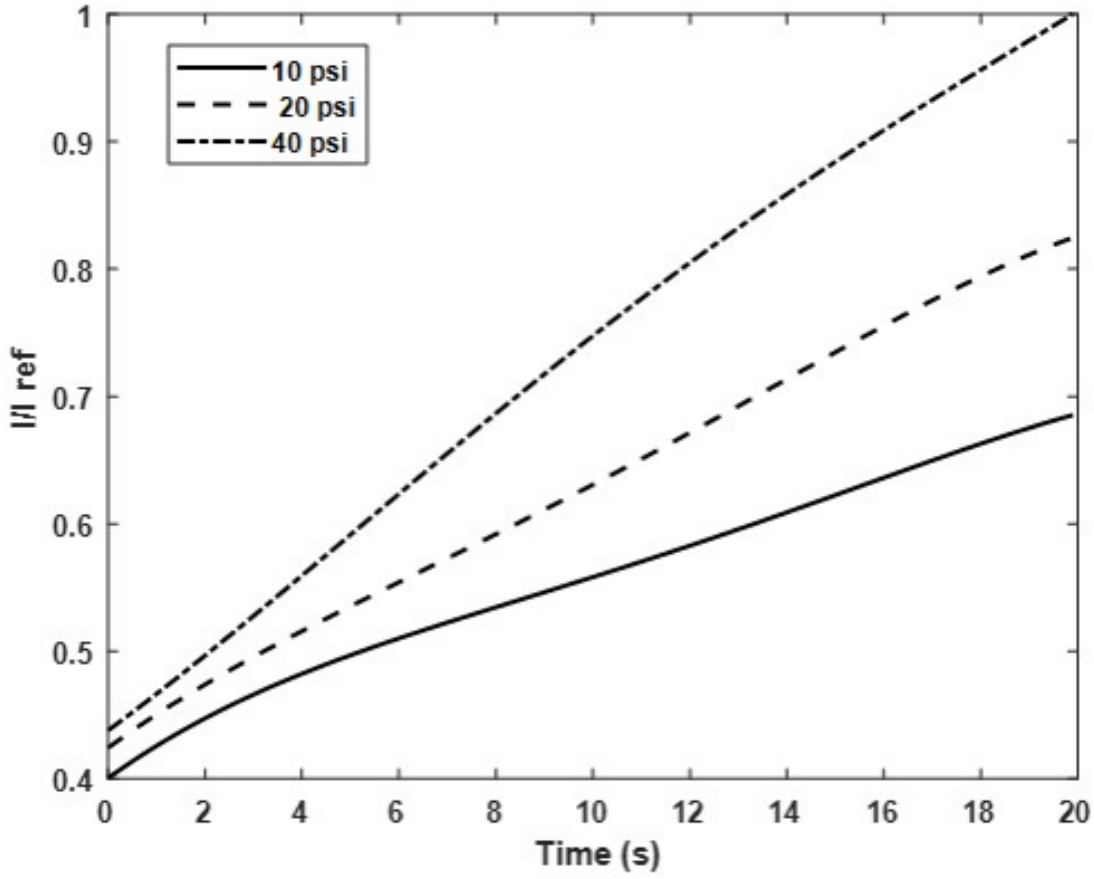

Figure 6.38: Normalized of the integrated intensity of deposited droplets at different pressures (Diamond W =12.7 mm).

6.2.3 Oval Body Shape of the TIPC Device

The deposited particles, in the pipe due to the oval body shape of the TIPC device, are visualized at the same conditions for the two previous models of the TIPC device, Cylinder and Diamond. Figure 6.39 shows the visualization of deposited particles at different times based on the luminescent intensity changing. The inlet pressure is equal to 10 psi with 17.98 m/s of flow velocity. The visualization of the deposited droplets as a result of increasing inlet pressure to be 20 psi with 27.3 m/s of flow velocity, is presented in figure6.40 at different times. The last visualization is implemented at a pressure equal to 40 psi and 41.4 m/s of velocity flow. The luminescent intensity images of deposited particles from last visualization are shown in figure6.41 at different times. For all values of pressures, the ensemble-averaged velocity magnitude field of oil droplets deposition is calculated and presented in figure6.42. The concentration of deposited droplets is changed with changing inlet pressure value. The luminescent intensity of deposited particles is the integarted with respect of time to illustrate the effect of pressure values on the concentration of deposited droplets. Figure 6.43 shows the normalization of the integrated intensity of deposited droplets at different pressure values that are 10 psi, 20 psi and 40 psi.

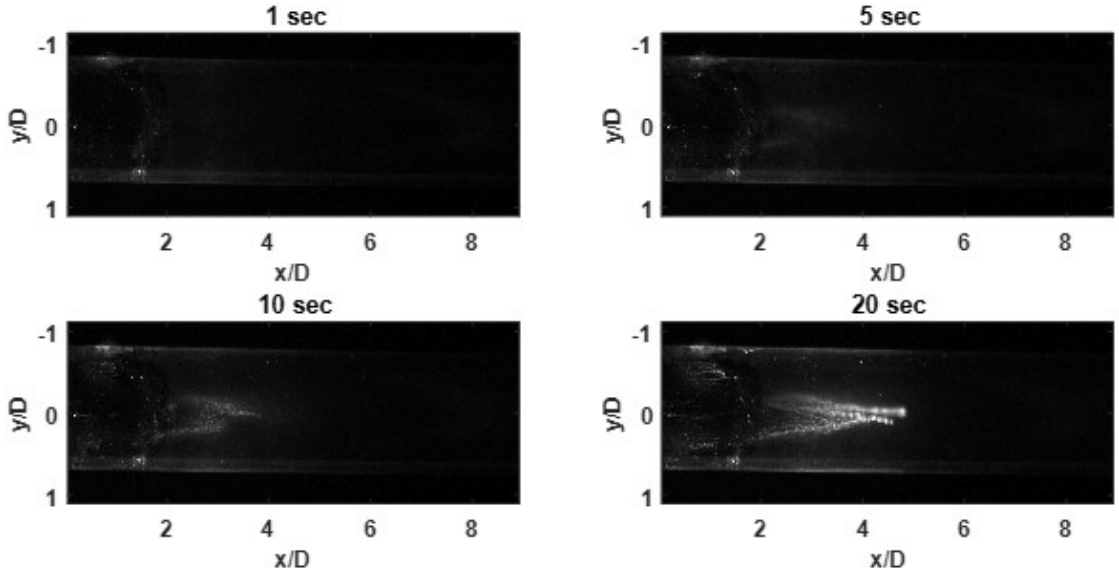

Figure 6.39: Visualization luminescent intensity images of deposited droplets at different times at 10 psi (Oval body).

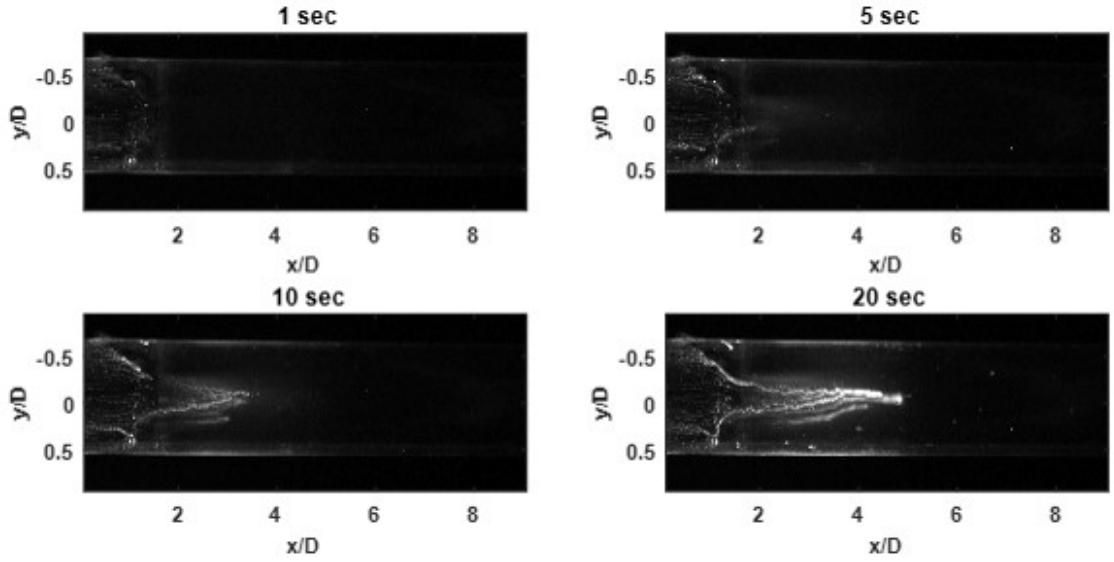

Figure 6.40: Visualization luminescent intensity images of deposited droplets at different times at 20 psi (Oval body).

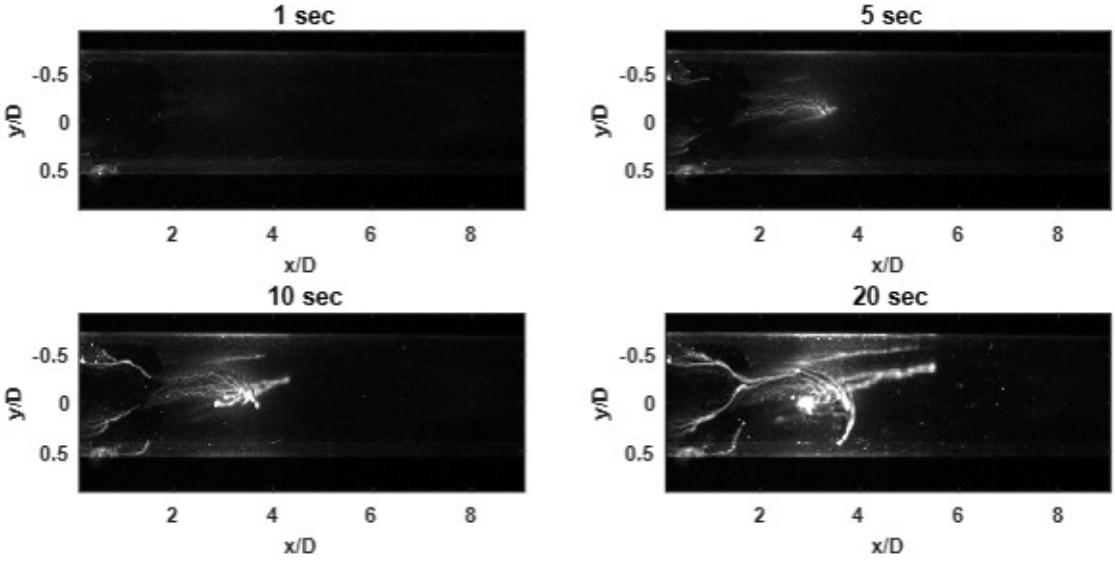

Figure 6.41: Visualization luminescent intensity images of deposited droplets at different times at 40 psi (Oval body).

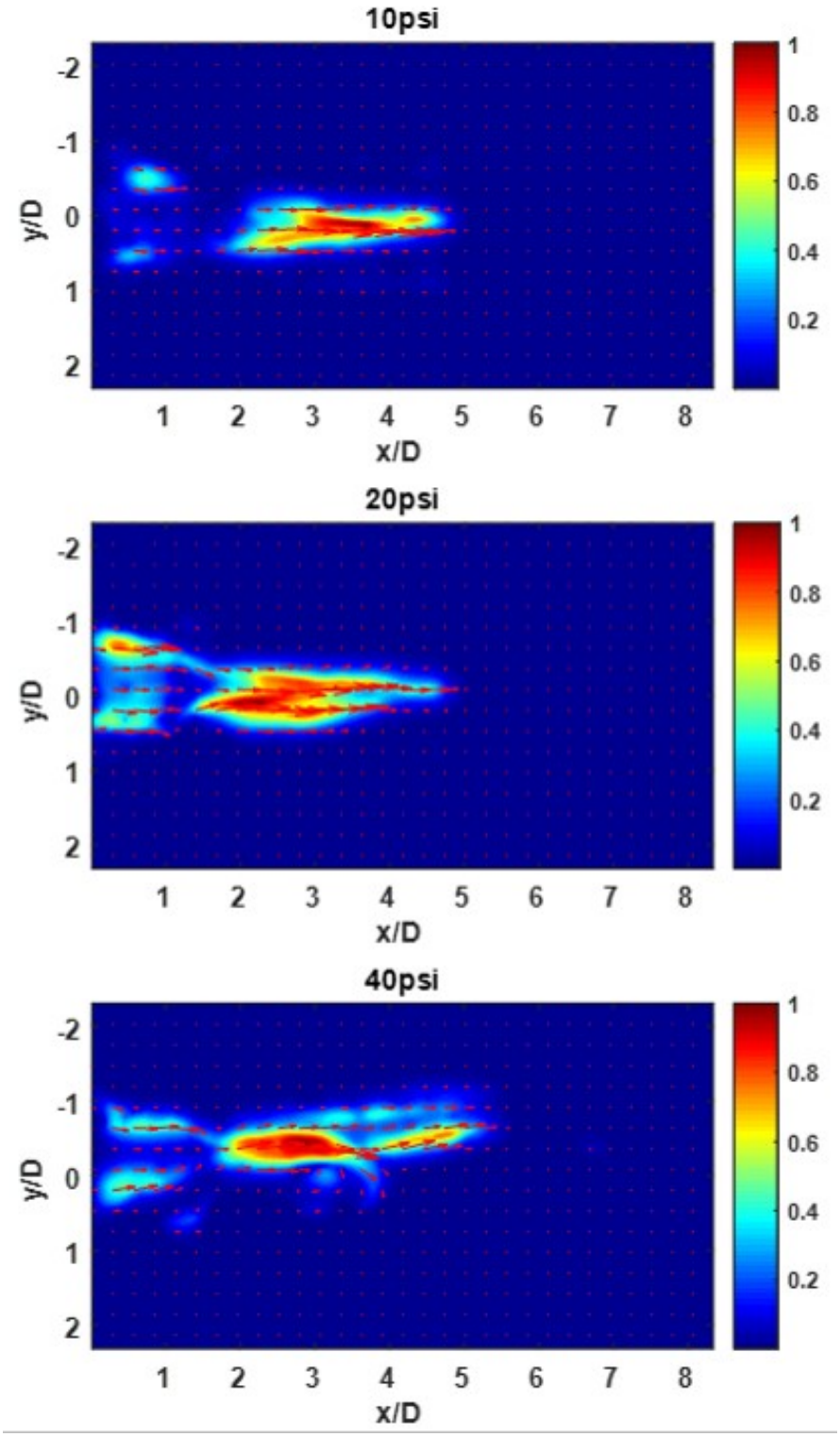

Figure 6.42: The ensemble-averaged velocity magnitude field of oil droplets deposition at different pressures (Oval body).

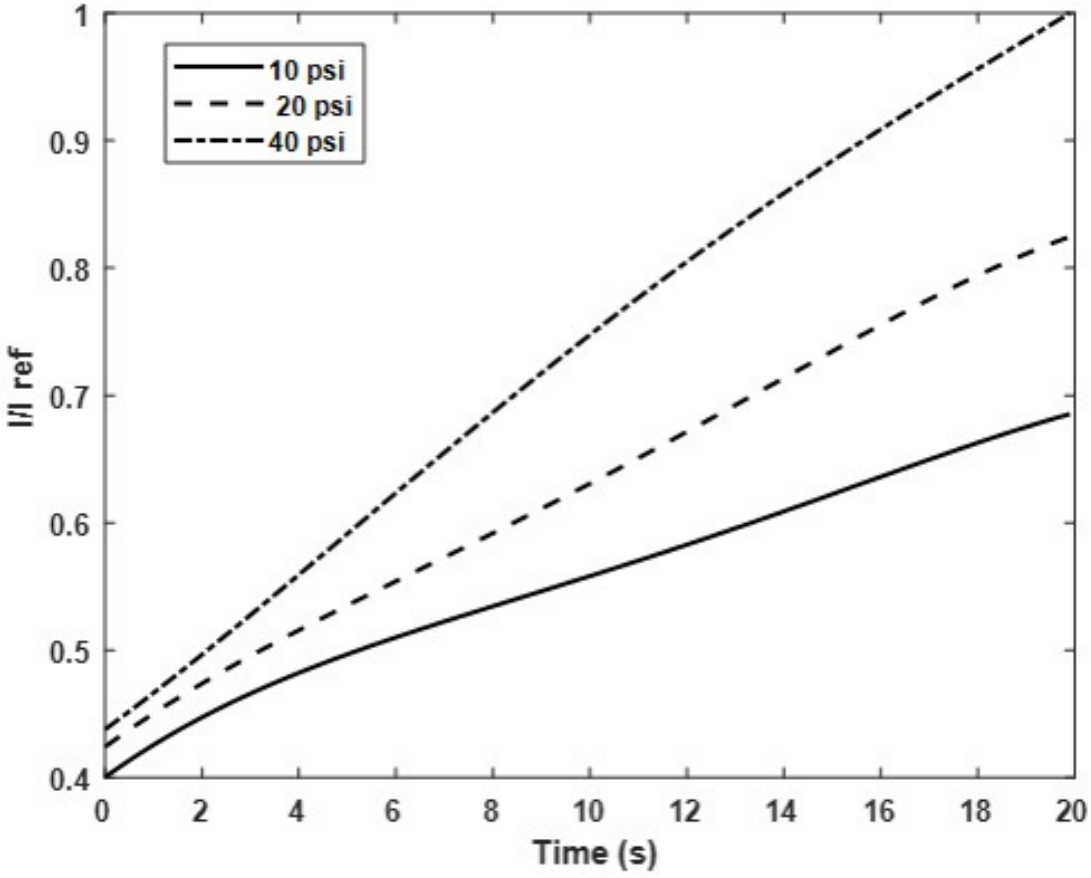

Figure 6.43: Normalized of the integrated intensity of deposited droplets at different pressures (Oval body).

Chapter 7

Numerical Solution

7.1 Procedure Description

This chapter is explained using a commercial software package ANSYS FLUENT Workbench 19.1 in order to determine the flow characteristics, velocity, kinetic energy and Reynold stress, that are produced through the TICP device. Three configurations of the TICP have been investigated numerically using ANSYS Fluent at inlet velocity is equal to 41.4 m/s. This value is calculated experimentally using the manometer, based on the Bernoulli's equations: $V = \sqrt{\frac{2\Delta p}{\rho}}$.

The inputs required in ANSYS FLUENT Workbench 19.1 to carry out the numerical solution are shown in figure 7.1. The first requirement of the simulation is to build the geometry and generate the mesh using ANSYS Workbench, the mesh characteristics for the TIPC configurations are presented in table 7.1. Next, define the type of viscus model and the boundary conditions in FLUENT Software. Then, the results of calculation can be obtained at the end using FLUENT software.

Table 7.1: Mesh characteristics

Models	Nodes	Elements
Cylinder	8830	8150
Diamond	17127	15880
Oval Body	21471	15880

The turbulence kinetic energy, k, and its rate of dissipation, ε, are obtained from the fol-

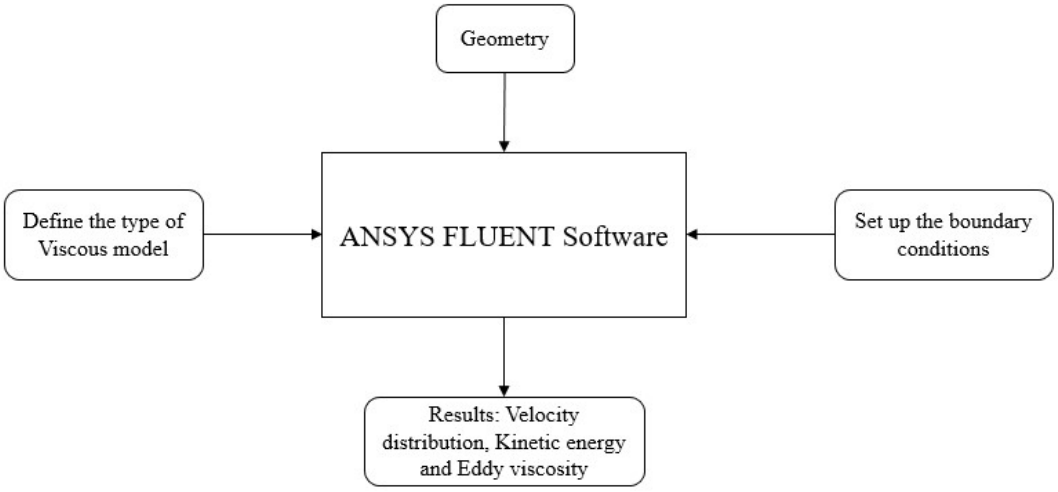

Figure 7.1: Schematic of the inputs required in ANSYS FLUENT 19.1 and outputs.

lowing transport equations:

$$\frac{\partial}{\partial t}(\rho k)+\frac{\partial}{\partial x_i}(\rho k u_i)=\frac{\partial}{\partial x_j}\left[\left(\mu+\frac{\mu_t}{\sigma_k}\right)\frac{\partial k}{\partial x_j}\right]+G_k+G_b-\rho\varepsilon-Y_M+S_k \tag{7.1}$$

and

$$\frac{\partial}{\partial t}(\rho \varepsilon)+\frac{\partial}{\partial x_i}(\rho \varepsilon u_i)=\frac{\partial}{\partial x_j}\left[\left(\mu+\frac{\mu_t}{\sigma_k}\right)\frac{\partial \varepsilon}{\partial x_j}\right]+G_{1\varepsilon}\frac{\varepsilon}{k}(G_k+G_{3\varepsilon}G_b)-G_{2\varepsilon}\rho\frac{\varepsilon^2}{k}+S_\varepsilon \tag{7.2}$$

In these equations, G_k represents the generation of turbulence kinetic energy due to the mean velocity gradients, calculated as described in in Modeling Turbulent Production in the k-ε Models. G_b is the generation of turbulence kinetic energy due to buoyancy, calculated as described in Effects of Buoyancy on Turbulence in the k-ε Models. Y_M represents the contribution of the fluctuating dilatation in compressible turbulence to the overall dissipation rate, calculated as described Effects of Compressibility on Turbulence in the k-ε Models. $G_{1\varepsilon}$, $G_{2\varepsilon}$, and $G_{3\varepsilon}$ are constants. σ_k and σ_ε are the turbulent Prandtl numbers for K and ε , respectively. S_k and S_ε are user-defined source terms.

The Turbulent viscosity is modeling by applying the following equation:

$$\mu_t=\rho C_\mu\frac{k^2}{\varepsilon} \tag{7.3}$$

Where μ_t is the turbulent (eddy) viscosity and C_μ is a constant.

The model constants $G_{1\varepsilon}$, $G_{2\varepsilon}$, $G_{3\varepsilon}$, σ_k *and* σ_ε have the default values as following :

$G_{1\varepsilon}$ =1.4, $G_{2\varepsilon} = 1.92, G_\mu$ =0.09, $\sigma_k = 1.0$, $\sigma_\varepsilon = 1.3$.

7.2 Results

Figure 7.2(a) shows the velocity distribution for the fluid flow (water vapor) through the configuration 1(B) of the TIPC device.The maximum value of velocity is generated on both sides of the pipe due to the TIPC device.The turbulent kinetic energy and eddy viscosity fields are shown in figures 7.2(b) and 7.2(c). The TKE is produced and focused behind the cylinder directly. The velocity distribution field for the configuration 2(B) of TIPC device is presented in figure 7.3(a). The high velocity is generated on both sides of pipe as a result of the TIPC device and continue for a certain distance. Figure 7.3(b) and figure 7.3(c) show the kinetic energy and eddy viscosity fields, respectively. Figure 7.4(a) shows the velocity distribution for the fluid flow through the configuration 4 of TIPC device. The velocity is increased to maximum on both sides of the pipe along the surface area of the TIPC model. Figure 7.4(b) show the kinetic energy field for the configuration 4 of the TIPC device while the viscous viscosity field for the same model is shown in figure 7.4(c).

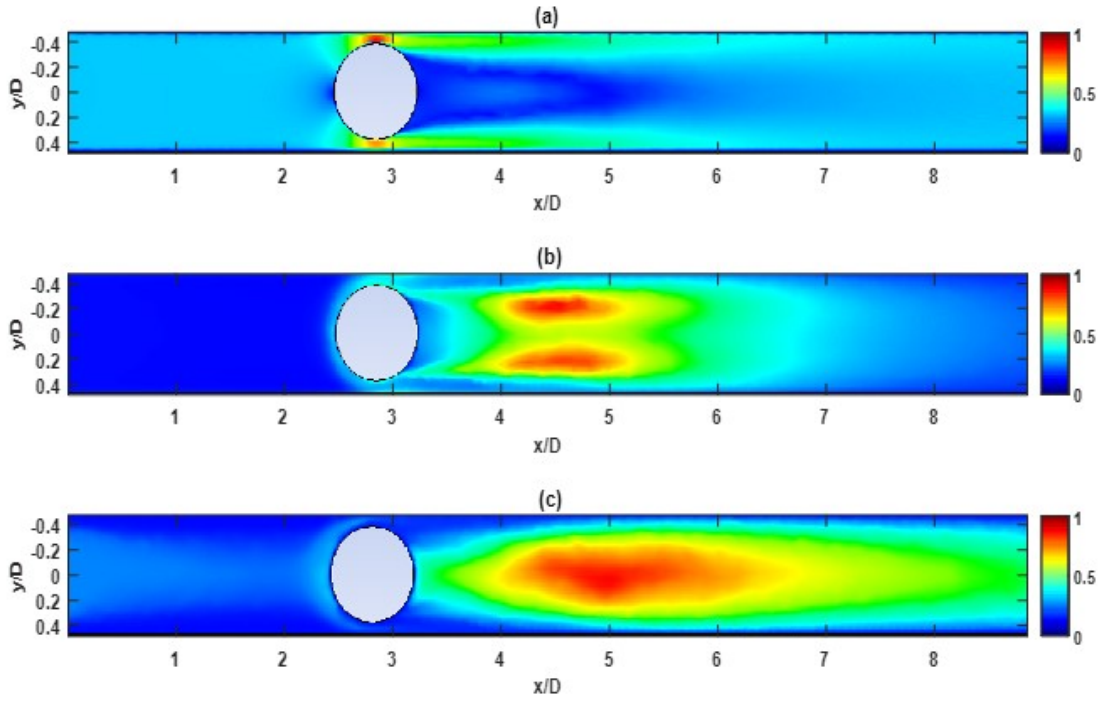

Figure 7.2: Flow characteristics for the cylinder design of TIPC device (a) ensemble-averaged velocity magnitude fields and (b) Turbulent kinetic energy field and (c) Eddy viscosity field .

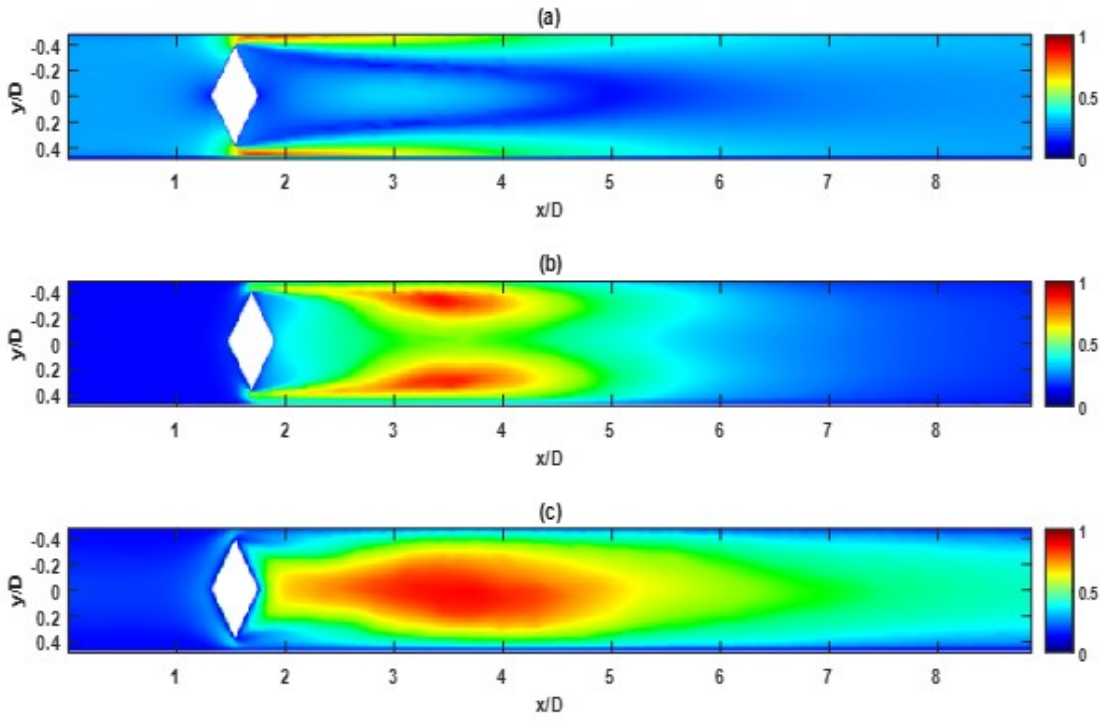

Figure 7.3: Flow characteristics for the Diamond design of TIPC device (a) ensemble-averaged velocity magnitude fields and (b) Turbulent kinetic energy fields and (c) Eddy viscosity fields.

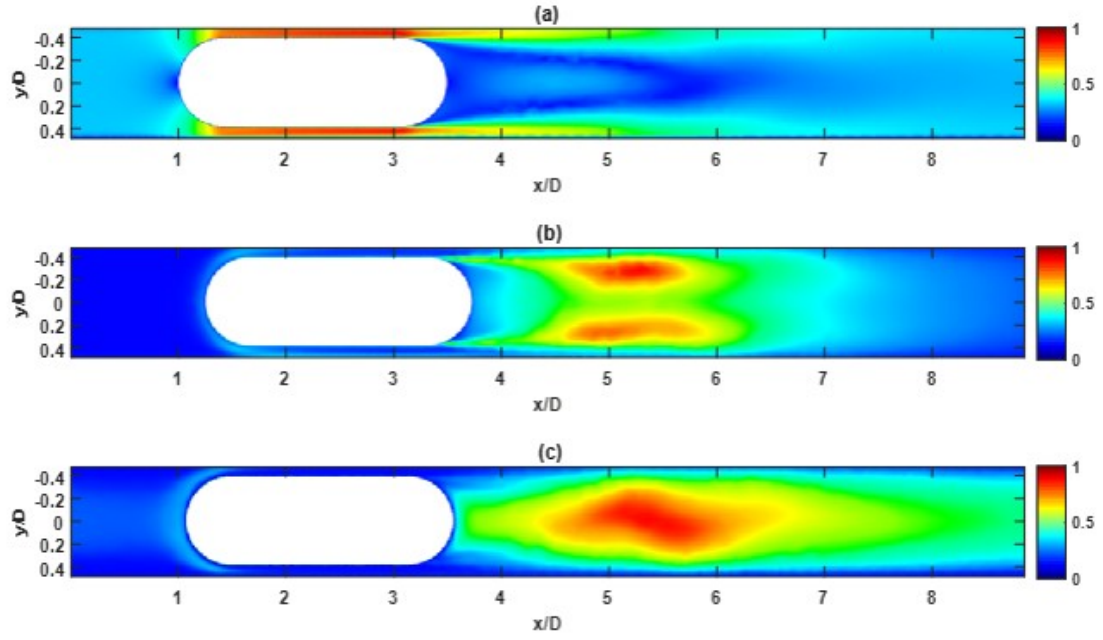

Figure 7.4: Flow characteristics for the Oval body design of TIPC device (a) ensemble-averaged velocity magnitude fields and (b) Turbulent kinetic energy fields and (c) Eddy viscosity fields.

Chapter 8

Conclusion

The physical mechanism of the TICP device has been built and studied experimentally. the TICP device are used to collect the water vapor at different temperatures. Different configurations of the TICP have been investigated in terms of increasing the rate of droplets collision. Two different experiments were conducted in order to prove the efficiency of the TIPC device using the visualization techniques. The first one was focused on the pattern of deposited oil droplets onto the dry surface due to the TIPC device. The pattern of deposited droplets becomes homogenous directly after few seconds of projected. The experiment has been done for all configurations of the TIPC device at two values of pressure, 5 psi and 20 psi. The results of all TIPC models at 20 psi show a high concentration of deposited oil droplets. Also, the cylinder shapes with a diameter of 12.7 mm generate more amount of deposited droplets based on the luminescent intensity concentration. Evidently, the large surface area of the TIPC led to increasing the shear stress which has affected increasing the probability of collisions between neighboring droplets to coalesce into larger droplets. The second experiment has applied for the visualization of the deposited droplets inside the pipe. Three configurations have been considered in terms of the efficiency, Cylinder (D=12.7 mm), Plate (W=12.7 mm) and Oval body (D=12.7 mm and L= 25.4 mm). ANSYS is used to determine the velocity distribution, the kinetic energy and eddy viscosity for configurations 1(B), 2(B) and 4.

REFERENCES

[1] Mark A Shannon, Paul W Bohn, Menachem Elimelech, John G Georgiadis, Benito J Marinas, and Anne M Mayes. Science and technology for water purification in the coming decades. *Nature (London, U. K.)*, 452(March):301–310, 2008.

[2] Srinivas Vasu Veerapaneni. Reducing energy consumption for seawater desalination. *American Water Works Association. Journal*, 99(6):95, 2007.

[3] Kim Choon Ng, Kyaw Thu, Youngdeuk Kim, Anutosh Chakraborty, and Gary Amy. Adsorption desalination: An emerging low-cost thermal desalination method. *Desalination*, 308:161–179, 2013.

[4] Mahmoud Shatat, Mark Worall, and Saffa Riffat. Opportunities for solar water desalination worldwide: Review. *Sustainable Cities and Society*, 9:67–80, 2013.

[5] H. Sharon and K. S. Reddy. A review of solar energy driven desalination technologies, 2015.

[6] S. M. El-Haggar and A. A. Awn. Optimum conditions for a solar still and its use for a greenhouse using the nutrient film technique. *Desalination*, 94(1):55–68, 1993.

[7] S Abdallah and O O Badran. Sun tracking system for productivity enhancement of solar still. *Desalination*, 220(1-3):669–676, 2008.

[8] Yasser Fathi Nassar, Saib A. Yousif, and Abubaker Awidat Salem. The second generation of the solar desalination systems. *Desalination*, 209(1-3 SPEC. ISS.):177–181, 2007.

[9] S. Al-Kharabsheh and D. Yogi Goswami. Experimental study of an innovative solar water desalination system utilizing a passive vacuum technique. *Solar Energy*, 75(5):395–401, 2003.

[10] A Ahsan, M Imteaz, U A Thomas, M Azmi, A Rahman, and N N Nik Daud. Parameters affecting the performance of a low cost solar still. *Applied Energy*, 114:924–930, 2014.

[11] B Selva Kumar, Sanjay Kumar, and R Jayaprakash. Performance analysis of a "V" type solar still using a charcoal absorber and a boosting mirror. *Desalination*, 229(1-3):217–230, 2008.

[12] B A Abu-Hijleh. K, Rababah, HM, 2003, Experimental study of a solar still with sponge cubes in basin. *Energy Conversion and Management*, 44:1411–1418, 2003.

[13] B. Janarthanan, J. Chandrasekaran, and S. Kumar. Performance of floating cum tilted-wick type solar still with the effect of water flowing over the glass cover. *Desalination*, 190(1-3):51–62, 2006.

[14] R Bhardwaj, M V Ten Kortenaar, and R F Mudde. Maximized production of water by increasing area of condensation surface for solar distillation. *Applied Energy*, 154:480–490, 2015.

[15] M. SOMMERFELD CHR. MUNDO and C. TROPEA. Droplet-Wall Collisions: Experimental Studies Of The Deformation And Breakup Process. *Int. J. Multiphase Flow*, 21(2):151–173, 1995.

[16] Lian-Ping. Wang, Orlando. Ayala, Scott E. Kasprzak, and Wojciech W. Grabowski. Theoretical Formulation of Collision Rate and Collision Efficiency of Hydrodynamically Interacting Cloud Droplets in Turbulent Atmosphere. *Journal of the Atmospheric Sciences*, 62:2433–2449, 2005.

[17] S Sikalo, M Marengo, C Tropea, and E N Ganic. Analysis of impact of droplets on horizontal surfaces. *Experimental Thermal and Fluid Science*, 25:503–510, 2002.

[18] W. C. Reade and L. R. Collins. Effect of preferential concentration on turbulent collision rates. *Physics of Fluids*, 12(10):2530–2540, 2000.

[19] Lance R. Collins and Arun. Keswani. Reynolds number scaling of particle clustering in turbulent aerosols Reynolds number scaling of particle clustering. *New Journal of Physics*, 119(6):1367–2630, 2004.

[20] L-P Wang, A. S. Wexler and Y. Zhou. Statistical mechanical description and modeling of turbulent collision of inertial particles. *J. Fluid Mech*, 415:117–153, 2000.

[21] R. Rioboo, M. Voue, A Vaillant, and J De Coninck. Drop Impact on Porous Superhydrophobic Polymer Surfaces. *American Chemical Society*, (25):14074–14077, 2008.

[22] R. Rioboo, C. Bauthier, J. Conti, M. Voue, and J De Coninck. Experimental investigation of splash and crown formation during single drop impact on wetted surfaces. *Experiments in Fluids*, 35:648–652, 2003.

[23] J Fukai, Y Shiiba, T Yamamoto, O Miyatake, D Poulikakos, C M Megaridis, and Z Zhao. Wetting effects on the spreading of a liquid droplet colliding with a flat surface : Experiment and modeling. *Physics of Fluids*, 236(7), 1995.

[24] R. Rioboo, M. H. Adao, M. Voue, and J. De Coninck. Experimental evidence of liquid drop break-up in complete wetting experiments. *J Mater Sci*, pages 5068–5080, 2006.

[25] Tianshu. Liu, Jacob. Nink, Parviz. Merati, Tian. Tian, Yong. Li, and Tom. Shieh. Deposition of micron liquid droplets on wall in impinging turbulent air jet. *Experiments in Fluids*, 48(6):1037–1057, 2010.

[26] Tianshu. Liu. Probability density function of small separation between two inertial particles in homogenous isotropic turbulence. *Physics of Fluids*, 22(4):045105–1 to 7, 2010.

[27] Shivshankar. Sundaram and Lance R. Collins. Collision statistics in an isotropic particle-laden turbulent suspension. Part 1. Direct numerical simulations. *J. Fluid Mech*, 335:75–109, 1997.

[28] Walter C Reade and Lance R Collins. Effect of preferential concentration on turbulent collision rates. *Physics of Fluids*, 12(2530), 2000.

[29] R. C. Hogan and J. N. Cucci. Stokes and Reynolds number dependence of preferential particle concentration in simulated three-dimensional turbulence. *Physics of Fluids*, 2938(13), 2001.

[30] J. Bec, A. Celani, M. Cencini, and S. Musacchio. Clustering and collisions of heavy particles in random smooth flows. *Physics of Fluids*, 17:073301, 2005.

[31] J. Bec, L. Biferale, M. Cencini, A. Lanotte, S. Musacchio, and F. Toschi. Heavy particle concentration in turbulence at dissipative and inertial scales. *Physical Review Letters*, 98:084502, 2007.

[32] Leonid I. Zaichik and Vladimir M. Alipchenkov. Pair dispersion and preferential concentration of particles in isotropic turbulence Pair dispersion and preferential concentration of particles in isotropic turbulence. *Physics of Fluids*, 15(1776), 2003.

[33] Leonid I. Zaichik and Vladimir M. Alipchenkov. Refinement of the probability density function model for preferential concentration of aerosol particles in isotropic turbulence Refinement of the probability density function model for preferential. *PHYSICS OF FLUIDS*, 19(113308), 2007.

[34] Jaehun. Chun, Donald L. Koch, and Lance R. Collins. Clustering of aerosol particles in isotropic turbulence. *J. Fluid Mech*, 536:219–251, 2005.

[35] E. Balkovsky, G. Falkovich, and G. Fouxon. Intermittent distribution of inertial particles in turbulent flows. *Physical Review Letters*, 86(2790), 2001.

[36] G. Falkovich, A. Fouxon, and M. G. Stapanov. Acceleration of rain initiation by cloud turbulence. *Nature*, 419(151), 2002.

[37] G. Falkovich and A. Pumir. Intermittent distribution of heavy particles in a turbulent flow. *Physics of Fluids*, 14(147), 2004.

[38] R. L. Stratonovich. Topics in the Theory of Random Noise (vol. 1). chapter 4. Gordon and Breach, New York, 1963.

[39] W. P. Elderton and N. L. Johnson. Systems of frequency curves. chapter 4. Cambridge, 1969.

[40] J. K. Ord. Families of frequency distributions. chapter 1. Griffin, London, 1972.

[41] N. L. Johnson and S. Kotz. Continuous univariate distributions-1. chapter 12. Houghton Mifflin Company, Boston, 1970.

[42] Edward N. Fuller, Keith Ensley, and J. Calvin Giddings. Diffusion of halogenated hydrocarbons in helium. The effect of structure on collision cross sections. *Journal of Physical Chemistry*, 73(11):3679–3685, 1969.

[43] Tianshu Liu. OpenOpticalFlow: An Open Source Program for Extraction of Velocity Fields from Flow Visualization Images. *Journal of Open Research Software*, 5, 2017.

[44] Tianshu Liu, J Montefort, S Woodiga, P Merati, and Lixin Shen. Global Luminescent Oil-Film Skin-Friction Meter. *AIAA JOURNAL*, 46(2), 2008.